Linear and Non-Linear Ultrasonic NDE of Titanium Diffusion Bonds

Edwill Alejandro Escobar-Ruiz

June 2014

Thesis submitted for the degree of Doctor of Engineering to

Imperial College London
Department of Mechanical Engineering

The content of this thesis has formed the basis for the following publications and is entirely original except where references acknowledge the work of others:

- Escobar-Ruiz, E., Cawley, P., Nagy, P. B., Collison, I. J., and Wright, D. C. (2013) Ultrasonic NDE of Titanium Diffusion Bonds Using Signal Phase. *Review of Progress in Quantitative Nondestructive Evaluation*, **32**, 1409–1416

- Escobar-Ruiz, E., (2013) *Ultrasonic Inspection Method*, Rolls-Royce plc, European Patent EP2778673 A2

- Escobar-Ruiz, E., Ruiz, A., Hassan, W., Wright, D. C., Collison, I. J., Cawley, P., Nagy, P. B. (2014) Non-Linear Ultrasonic NDE of Titanium Diffusion Bonds, *Journal of Nondestructive Evaluation*, **33** (2), 187–195, DOI: 10.1007/s10921-013-0217-5

- Escobar-Ruiz, E., Wright, D. C., Collison, I. J., Cawley, P., Nagy, P. B. (2014) Reflection Phase Measurements for Ultrasonic NDE of Titanium Diffusion Bonds, *Journal of Nondestructive Evaluation*, **33** (4), 535–546, DOI: 10.1007/s10921-014-0250-z

Para Diana

Abstract

Diffusion bonding is an attractive solid-state welding technique that promises weight reduction and improved performance in the aerospace industry. However, its adoption in fracture critical titanium components has been limited by the complications that macroscopic anisotropy introduces to typical ultrasonic NDE. Two strands of ultrasonic NDE, linear and non-linear acoustics, have been studied with the aim of overcoming these complications.

A promising linear technique that uses the phase of reflected diffusion-bond signals to extract otherwise hidden interface information was selected for further development. The principal parameters that affect the phase analysis of ultrasonic signals were investigated and their optimisation resulted in up to an order of magnitude improvement in phase measurement reliability, even at low signal-to-noise ratios. The application of these optimised parameters without a priori knowledge of the signal arrival time was illustrated, and the sensitivity of the approach to ambient temperature and annealing effects was also explored. The original technique was susceptible to measurement error and proved impractical for typical aerospace component geometries, but these shortcomings have been overcome by the improvements and adaptations proposed here. However, it was shown that the efficacy of the technique depends on the relative acoustic impedances of the bonded media and, coupled with the sensitivity limit intrinsic to linear acoustic methods, this dependence acted to curtail the benefits of the approach and prompted the exploration of alternative techniques.

Non-linear ultrasonic methods are significantly more sensitive than their linear counterparts to the imperfections likely to be present at diffusion-bonded interfaces, but suppressing extraneous contributions to the non-linear response of the interface is not trivial. An approach that succeeds in suppressing such contributions was studied and developed here. The technique, which is based on the non-collinear mixing of ultrasonic waves to generate a spectrally, modally and spatially dissociable third wave, was used to reliably characterise a set of samples whose bond quality was indeterminable using linear ultrasonic methods. Application of the technique to diffusion-bonded titanium aerospace components has been demonstrated and a significant improvement in ultrasonic NDE capability was achieved.

Acknowledgements

This work is the culmination of the valued input and support of a great many people, principal amongst them my academic supervisors Peter Cawley and Peter Nagy. The Peters must tire of students eulogising about their many merits and the thorough, dedicated support they provide, but it is not in imitation that I thank them for making a reality the work that is laid out in this document.

I am equally grateful to Chris Scruby and everyone at the RCNDE for their encouragement and selfless sharing of wisdom and knowledge, and of course to my industrial supervisors David Wright and Ian Collison, who have been and will continue to be my mentors at Rolls-Royce plc. There are many others at Rolls-Royce who have been instrumental in this project: Phillip Doorbar, David Rugg, Anthony Dunhill, Gareth Friend and of course the NDE Laboratory team. I thank these wonderful people for making research in NDE anything but a Near Death Experience. Katherine Milne was my expert guide at the beginning and this work is accordingly sprinkled with references to her research, each of which should be interpreted as a warm "thank you" for her kind efforts.

Finally, I thank my family and friends. Your patience and understanding ("sorry I'm late/didn't show up/have to leave early"), love and encouragement have been the very things that have driven the completion of this adventure.

This work was jointly funded by Rolls-Royce plc, the Engineering and Physical Sciences Research Council (EPSRC) and the UK Research Centre in NDE (RCNDE)

Contents

List of Figures **8**

List of Tables **10**

Nomenclature **11**

1 Introduction **14**

1.1 Titanium Diffusion Bonds 14

1.2 Inspection Problem Definition 17

1.3 Thesis Outline 20

2 Background to Ultrasonic NDE of Bonds **22**

2.1 Linear Ultrasonic NDE of Diffusion Bonds 22

2.2 Non-Linear Ultrasonic NDE of Diffusion Bonds 28

2.3 Summary 33

3 Linear Ultrasonic Approach **35**

3.1 Single-Sided Inspection 36

3.2 True-Phase Measurement Reliability 39

3.2.1 Observation Window Length 41

3.2.2 Phase-Spectrum Region of Interest 47

3.2.3 Observation Window Shape 48
3.3 Evaluation of Proposed Parameters 49
3.4 Summary 51

4 Practical Considerations of Linear Approach 52
4.1 Sensitivity to Signal Arrival Time 52
4.2 Effects of Ambient Temperature and Annealing 56
4.3 Practical Implementation 59
4.4 Evaluation of Single-Sided Linear Technique 63
4.5 Summary 70

5 Non-Linear Ultrasonic Approach 72
5.1 Optimised Wave-Mixing for Interface Inspection 72
5.2 Bulk and Interface Experiments 75
5.3 Results and Discussion 79
5.4 Summary 85

6 Conclusions and Overview 87
6.1 Summary of Findings 88
6.2 Future Work 92

References 94

Appendices 106
Appendix A: Filtering Effects of an Imperfect Interface 106
Appendix B: Experiment Jig 108
Appendix C: Computational Code 110
Appendix D: True-Phase Maps 113
Appendix E: Non-Linear Specimen Micrographs 114

List of Figures

1.1 Cross-sections of a diffusion-bonded interface at three stages of consolidation 16

1.2 Radial cross-sections of monolithic and MMC-reinforced compressor discs 16

1.3 Preferential alignment of HCP crystals within macro-zones 18

1.4 Cross-section of MMC-reinforced compressor disc inspected ultrasonically 20

2.1 Low frequency resonance technique as used to inspect diffusion-bonds 25

2.2 Double-sided ultrasonic inspection of titanium diffusion bonds 26

2.3 Phase spectra of two identical signals with different arrival times 27

2.4 Immersion *shear* + *shear* → *longitudinal* wave-mixing experiment 31

3.1 Single-sided ultrasonic inspection of titanium diffusion bonds 36

3.2 Variation of κ with Φ_{bond} for typical inspection of a Ti-6Al-4V titanium alloy 38

3.3 Typical waveforms used during true-phase measurement analyses 40

3.4 Definition of the various time domain parameters referred to in the text 40

3.5 True-phase measurement uncertainty for the benchmark parameters 42

3.6 Measurement uncertainty variation with window length (transducers A & B) 43

3.7 Measurement uncertainty variation with window length (transducers C & D) 43

3.8 True-phase variation with window position along pulse 44

3.9 Region of interest slope variation with window position (transducers A & B) 45

3.10 Region of interest slope variation with window position (transducers C & D) 45

3.11 Phase spectra of reference signals from transducer B 46

3.12 Measurement uncertainty variation with region of interest 47
3.13 Measurement uncertainty variation with window shape 49
3.14 True-phase measurement uncertainty using optimised parameters 50
4.1 Example of an adaptive gating procedure 55
4.2 Energies of spatially-averaged interface signals using different gating methods 56
4.3 Absolute true-phase measurement variation due to annealing 58
4.4 Absolute true-phase measurement variation due to changing water temperature . . . 59
4.5 Overall single-sided linear inspection procedure 61
4.6 Computational algorithm for determining component interfacial stiffness maps . . . 62
4.7 Geometry of specimens used to evaluate single-sided linear approach 65
4.8 Representative single- and double-sided κ maps for different contaminants used . . . 66
4.9 Comparison of single-sided and double-sided estimates of interfacial stiffness 67
4.10 Comparison of interfacial stiffness and conventional ultrasonic responses 68
4.11 Representative micrographs for samples with low average interfacial stiffness 69
5.1 Variation of Θ, θ_{1s} and θ_{2s} with a given $c = 0.519$ and $\nu = 0.316$ 73
5.2 Variation of θ_{2s} with a given $\theta_{1s} = 54°$, $c = 0.519$ and $\nu = 0.316$ 74
5.3 Shear-wave energy transmission coefficient variation with incidence angle 75
5.4 Wave-mixing experiment for the inspection of diffusion-bonded interfaces 76
5.5 Geometry of specimens used to evaluate the non-linear technique 78
5.6 Micrographs of samples used in non-linear experiments 79
5.7 Results of non-linear inspections using interface configuration 80
5.8 Comparison between two repetitions of the interface non-linear experiment 80
5.9 Comparison between the interface and bulk configuration non-linear responses . . . 82
5.10 Linear and non-linear response variation with bond quality 82
5.11 10 MHz and 25 MHz conventional ultrasonic responses for non-linear samples 84

List of Tables

3.1 Main characteristics for transducers used in true-phase experiments 41

4.1 Contaminants used in single-sided linear technique experiments 64

5.1 Experiment parameters for bulk and interface non-linear experiments 76

5.2 Transducer and electronics parameters for non-linear experiments 77

5.3 CBGG and pertinent bonding parameters for non-linear experiments 78

Nomenclature

β	Non-linear parameter
δ_{i}	Relative delay between reference and i^{th} waveforms
$\lvert\Delta\Phi\rvert$	Point-by-point absolute difference between true-phase maps
ε_{ij}	Lagrangian strain
η	Relative acoustic impedance mismatch
Θ	Total intersection angle of the waves impinging on interaction volume
$\theta_{i\mathrm{s}}$	Incidence angle for shear wave from i^{th} transducer impinging on interaction volume
$\theta_{i\mathrm{t}}$	Incidence angle for wave from i^{th} transducer impinging on surface
κ	Interfacial stiffness per unit length
Φ	True phase
Φ_{bond}	Interface true phase
Φ_{ref}	Reference true phase
φ	Phase spectrum
φ_{RoI}	Region of Interest within phase spectrum
φ'_{RoI}	Gradient of the Region of Interest within phase spectrum

ω	Angular frequency
a	Frequency ratio between transducers 1 and 2
B	Transducer bandwidth
B_{n}	Normalised transducer bandwidth
c	Shear-to-longitudinal velocity ratio
c_{l}	Longitudinal wave velocity
c_{ijkl}	Second-order elastic constants
c_{ijklmn}	Third-order elastic constants
F	Transducer focal distance
f_{c}	Transducer centre frequency
$\mathbf{k}_i$	Wave vector for i^{th} wave
k_{l}	Longitudinal wave number
L	Inspection scan line length
m	Mass per unit area
R_i	Reflection coefficient of i^{th} component
S	Horizontal distance between the impingement points of the two incident waves
SD_Φ	True-phase measurement standard deviation
R_{a}	Asymmetric reflection coefficient
R_{s}	Symmetric reflection coefficient
T_{p}	Signal period
T_{s}	Pulse length

T_{w}	Observation or 'extraction' window length
U	Strain energy density
Z	Harmonic mean of acoustic impedances
Z_i	Acoustic impedance of i^{th} component
CAN	Contact Acoustic Non-linearity
CBGG	Cross-Boundary Grain Growth
ENBW	Equivalent Noise Bandwidth
MMC	Metal Matrix Composite
PoD	Probability of Detection
TRL	Technology Readiness Level
TiMMC	Titanium Metal Matrix Composite
TOEC	Third-Order Elastic Constant

1. Introduction

Non-Destructive Evaluation (NDE) involves the exploitation of a wide range of techniques in order to assess the integrity or determine the properties of a material without damaging it. It is an essential process that underpins the economic, environmental and safety performance of the aerospace industry and myriad other sectors. There are several established techniques, and these are continually evolving to address the demands that novel materials and manufacturing processes place on contemporary capability. In the aerospace industry, these demands are intensified by the need to minimise weight, which leads to damage tolerant designs that rely on early detection and characterisation of material irregularities in order to ensure safety and performance [1].

A significant portion of the work to address these demands in the United Kingdom is coordinated by the UK Research Centre in Non-Destructive Evaluation (RCNDE), which is a collaborative effort between industry and academia supported by the Engineering and Physical Sciences Research Council (EPSRC). The Engineering Doctorate (EngD) is commonly used as an efficient vehicle for technology transfer and ensures that research topics are relevant to the medium- and long-term needs of industry. Rolls-Royce plc, a global provider of integrated power systems and services to the aerospace, marine and energy markets, sponsored the author's EngD training and provided the 'capability acquisition' environment that has led to work presented here.

1.1 Titanium Diffusion Bonds

The significant advantages offered by the diffusion bonding process compared with conventional joining methods, coupled with the exceptional engineering properties of Ti-6Al-4V titanium al-

loys, mean that there are compelling benefits to be gained from fully exploiting diffusion-bonded titanium components in the aerospace industry [2].

Ti-6Al-4V is the most widely used material in the forward portion of typical aerospace gas turbine engines (the compressor stages) as a result of its excellent thermal, strength and weight properties [3]. Diffusion bonding of this useful material yields significant performance and weight improvements compared to typical fusion welds because, as a solid-state welding process in which no melting is involved, there is no distinct heat-affected zone where material properties vary dramatically and abruptly [4].

Instead, an ideally imperceivable interface is created via the bringing together of two or more surfaces under moderate heat. This heat provides the energy required for the crystals either side of the interface to diffuse across the boundary and form a bond of near parent-material strength [5]. The temperatures involved in this process are sensibly well below the beta-transus temperature, above which marked crystallographic changes would occur [6]. The surfaces are brought into intimate contact using relatively low isostatic pressures in order to mitigate the risk of deforming the components as they are being joined. Maintaining the heat and pressure for a given dwell time has the effect of forcing surface asperities to coalesce and induces the Cross-Boundary Grain Growth (CBGG) necessary for satisfactory bonding [7], as illustrated in Figure 1.1. Crucially, the process can be applied to complex geometries and dissimilar materials, which means that previously impracticable components, such as those that depend on Metal-Matrix Composites (MMCs), can now be manufactured reasonably economically [8].

MMCs are important because they allow material properties to be tailored according to local requirements, meaning that the strengths of a material are better exploited whilst any weaknesses are suppressed [10]. An example of the successful application of MMC technology is the Titanium Metal-Matrix Composite (TiMMC) compressor disc, which comprises an MMC reinforcement around the periphery of a forged titanium disc, as shown in Figure 1.2. Reinforcement means that less material is required around the axis of the disc in order to withstand the radial forces generated as the disc rotates, producing a component which weighs up to 60% less than conventional monolithic counterparts and which is therefore more akin to a ring than a disc [11, 12].

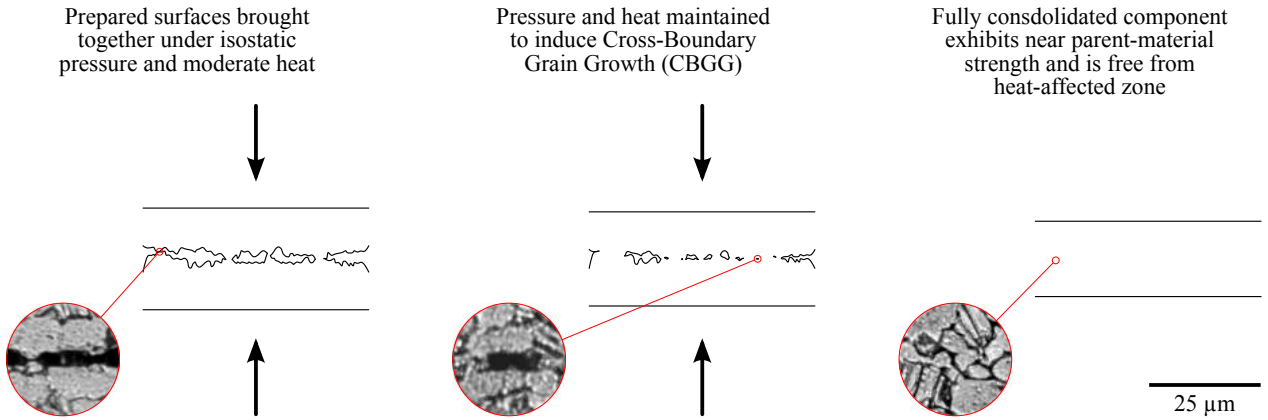

FIGURE 1.1 Cross-sections of a diffusion-bonded interface at three stages of consolidation. In this example, moderate heat and isostatic pressure are used to bring two components into intimate contact, inducing the Cross-Boundary Grain Growth that gives the bond near parent-material properties. After [9]

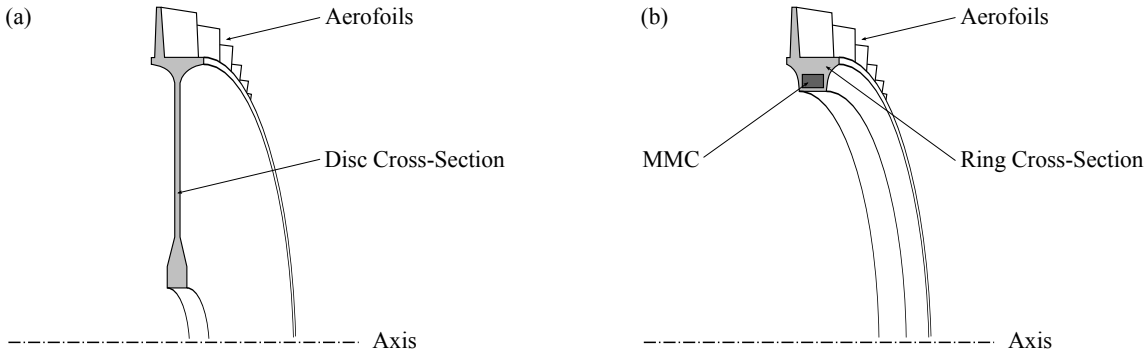

FIGURE 1.2 Radial cross-sections of (a) monolithic and (b) MMC-reinforced compressor discs. The MMC reinforcement of TiMMC discs produces weight savings of up to 60% compared with monolithic designs, but is only viable with the exploitation of the diffusion bonding process and the robust NDE that this entails. After [11]

There are several other components where titanium diffusion bonds play an important role in improving performance and reducing weight, such as super-plastically formed fan blades [13] and large diameter open-rotor engine hubs. In all cases, the integrity of the component, as determined through NDE, is safety-critical. Such exacting demands, together with the complexity of the geometries and the material characteristics of Ti-6Al-4V, have proven to be beyond the capability of current conventional NDE approaches [14]. The focus of the work presented here is to build upon the encouraging results documented by Katherine Milne [9] in order to develop a highly sensitive inspection process capable of sub-surface imaging for these advanced materials.

1.2 Inspection Problem Definition

NDE techniques are based on a variety of different physical phenomena (e.g. capillarity in Fluorescent Penetrant Inspection [15], electro-magnetism in Eddy Current Testing [16], emissivity in Thermography [17] etc.), which means that the performance and suitability of each technique depends heavily on the application for which it is being considered. For sub-surface inspections at depths of several tens of millimetres, only ultrasonic and radiographic techniques are capable of detecting, characterising and imaging sub-millimetre discontinuities. Ultrasonic inspection methods are the focus of the present work because radiographic NDE requires the implementation of extensive health, safety and environmental precautions that act to increase the unit cost of inspection and also impose restrictions on the size and geometry of the components that can be inspected [17].

Ultrasonic inspection of diffusion-bonded titanium components is made difficult by both geometric and material factors. The foremost material factor is macroscopic[1] anisotropy, to which ultrasonic NDE exhibits restrictive sensitivity even in materials having relatively modest levels of texture inhomogeneity [18]. Ti-6Al-4V is highly textured by virtue of the Hexagonal Close Packed (HCP) crystals that constitute the majority of its structure (approximately 90% by volume) [19]. The elastic modulus varies from 100 GPa (orthogonal to main axis) to 145 GPa (parallel to main axis) in these crystals [20–22], meaning that the speed of sound through the crystal can vary by as much as 20% depending on propagation direction.

Individual crystals tend to form large macro-zones that can be several millimetres in size and are therefore of comparable dimensions to typical ultrasonic signal wavelengths [23]. The crystals within a macro-zone are predominantly aligned [24], and so the speed of sound varies with propagation direction on a macro scale [25, 26]. Given that the relative orientation of neighbouring macro-zones is random, this results in distortions of the propagating sound wave (because different segments of a wavefront may propagate at different speeds) and intergranular acoustic impedance mismatches that cause significant back-scattered ultrasonic grain noise [19].

[1] In this context, macroscopic means large compared to the ultrasonic wavelength

At the diffusion bond, the random orientation of the opposing macro-zones either side of the interface additionally manifests itself as a weak planar reflector orthogonal to the transducer axis, as illustrated in Figure 1.3. This makes conventional ultrasonic inspection difficult because benign signals from the 'natural' acoustic impedance mismatches at the interface can shroud the signals from defects and voids. Importantly, these interfacial acoustic impedance mismatches are not indicative of bond quality: perfect diffusion bonds can exist between misaligned macro-zones that generate substantial acoustic reflections. To complicate matters further, the degree of mismatch varies from point-to-point within a component and consequently from component-to-component even if the materials are nominally the same.

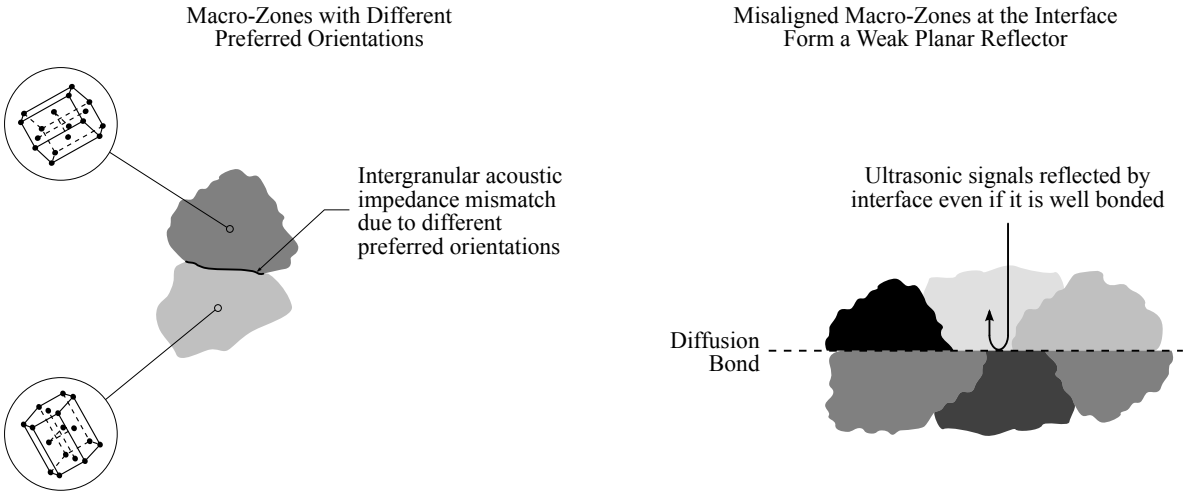

FIGURE 1.3 Preferential alignment of HCP crystals within macro-zones and the resulting effects on ultrasonic NDE. The boundary between macro-zones that have different preferred orientations constitutes an acoustic impedance mismatch, causing back-scattered grain noise and wavefront aberration. In addition, the planar nature of diffusion bonds means that the bonded interface behaves like a weak planar reflector that acts to limit inspection capability. After [27]

Coupled with the sensitivity to macroscopic anisotropy, the morphology of the imperfections that may be present at diffusion-bonded interfaces also acts to limit ultrasonic inspection capability [28]. This is because the size and shape of potential imperfections is strongly dependent on the initial surface roughness of the two surfaces to be joined [29], such that an imperfect diffusion bond may comprise reflectors much smaller than the interrogating wavelength. Unfortunately, even imperfections with dimensions of the order of magnitude of surface roughness can affect component fatigue life [30], placing greater demands on the robustness and sensitivity of any pro-

posed NDE solution. In essence, 100% CBGG is required when safety-critical components are manufactured, and a reliable NDE technique is needed to ensure this.

The problems posed by macrospic anisotropy and defect morphology are exacerbated by the complexity of the geometries to be inspected. Consider the TiMMC disc cross-section shown in Figure 1.4. Here, the disc has not had its blades attached and is at the 'rectilinear' stage of manufacture where its principal inspection is normally performed. Dotted lines indicate the position of the diffusion bonds in the component, each of which must be inspected. The depth of the bond at any given position is not more than approximately 100 mm, so ultrasonic pulses with moderately high centre frequencies ($\approx$ 20 MHz) should readily be able to insonify the interface. However, the MMC reinforcement attenuates, disperses, diffracts and distorts any ultrasonic signal that passes through it [31, 32], meaning that, even though the overall metal paths are relatively short, most of the diffusion bonds can only be accessed from one side and cannot be reliably inspected using through-transmission methods. Whilst MMCs are not present in all of the geometries where titanium diffusion bonds may be utilised, similar geometric considerations result in a general requirement to use a 'single-sided' ultrasonic inspection method only.

The amalgamation of the three factors that limit conventional ultrasonic NDE of titanium diffusion bonds (macroscopic anisotropy, inspection geometry complexity and defect morphology) result in the urgent need for improved ultrasonic NDE capability. The following is an outline of how the research put forward in this document, which aims to address this need, is structured.

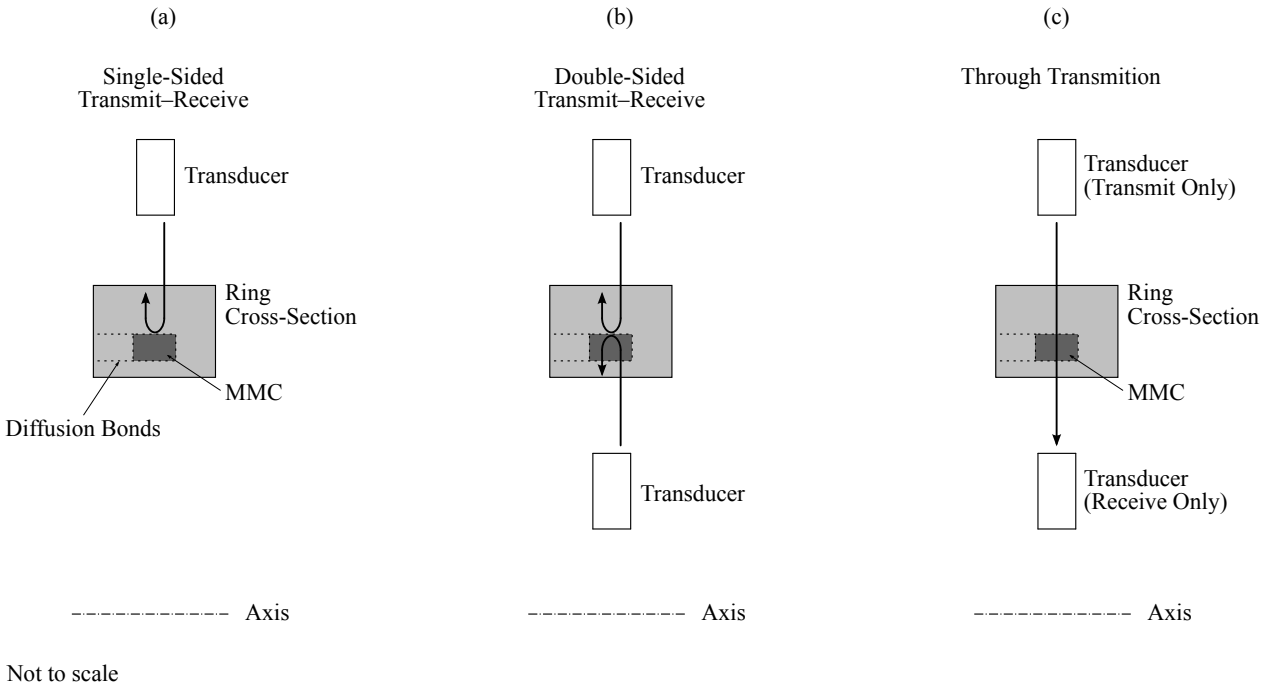

FIGURE 1.4 Radial cross-section of an MMC-reinforced compressor disc inspected in (a) single-sided transmit–receive mode, (b) double-sided transmit–receive mode and (c) through transmission mode. The complex nature of the MMC reinforcement means that diffusion bonds (denoted by dotted lines) can only be inspected if the ultrasonic pulses are not required to pass through the MMC material before detection at the receiving transducer. Only configuration (a) universally satisfies this condition

1.3 Thesis Outline

Research addressing some of the ultrasonic inspection requirements highlighted above generally falls into either linear or non-linear categories. The distinction between these two bodies of work is explained in Chapter 2, where details of the encouraging results produced by Milne et al. are provided and the various means of exploiting acoustic non-linearities are explored. In addition to detailing the background to these two categories of ultrasonic NDE, a strategy for developing the most promising approach in each strand is also detailed, thus forming the basis for the chapters that follow.

The proposed linear ultrasonic NDE approach is developed in Chapter 3. Its main limitation is addressed theoretically, and the computational algorithms on which it depends are optimised to yield an inspection technique that promises to satisfy the inspection requirements already exhibited.

Experimental validation of the approach is accordingly the main thrust of Chapter 4. First, potential limitations and complicating factors are explored, then the suggested operational procedure is laid out in detail before the technique is compared to its counterpart conventional linear method using representative samples.

Chapter 5 contains particulars of the work on non-linear ultrasonic NDE. The technique identified in Chapter 2 is adapted for the inspection of the geometries of interest here and the samples and experiments performed for validation are described. Experimental results are presented and compared with those from conventional linear ultrasonic tests, and conclusions are drawn from these as to the efficacy of each technique with respect to the original problem definition.

All of the main findings are summarised in Chapter 6, where an overview of this document is presented and where, finally, details of suggested future work are also given.

2. Background to Ultrasonic NDE of Bonds

Ultrasonic NDE is uniquely suited to the inspection of diffusion-bonded titanium components [9]. As a result, a significant body of work on ultrasonic methods aimed at addressing the problems discussed in Section 1.2 exists in the public domain. The various methods can be grouped into two main branches: 'linear ultrasonics', where superposition of stress fields holds; and 'non-linear ultrasonics', where complex wave interactions offer greater sensitivity to the material condition [33]. Linear techniques are widely available and relatively well-understood, but have proven inadequate for the inspection problem described before. Non-linear techniques are more complex, less well established and would require greater investment to achieve comparable levels of industrial acceptance [34], but are based on earlier and more sensitive indicators of material integrity, which is in harmony with the NDE requirements of solid-state welds [35].

2.1 Linear Ultrasonic NDE of Diffusion Bonds

In its simplest form, linear ultrasonic NDE involves insonifying a material with ultrasonic signals that are scattered or in some way modulated by the features of the material as the waves propagate along the surface of the specimen or through its bulk [36]. The condition of the insonified material is inferred from the specific nature of the scattering or modulation as detected either by the transmitting transducer ('transmit–receive') or by a separate receiving transducer ('through transmission') [37].

Several parameters affect the sensitivity of linear ultrasonic NDE to the condition of a material. An example of such a parameter is the transducer centre frequency, f_c, which is inversely propor-

tional to wavelength and thus closely related to the size of the artefacts that can be detected [38]: the higher the centre frequency, the greater the resolving capability of the transducer [39]. Extremely high ultrasonic centre frequencies are needed (of the order of 1 GHz) for the detection and characterisation of individual diffusion bond defects whose size is determined by the surface roughness prior to bonding (of the order of 1 µm ø) [40]. Furthermore, the scattering intensity from a spherical reflector with radius much smaller than the ultrasonic wavelength scales with f_c^4 [41], whereas scattering in the diffuse regime (where the reflector radius is greater than the wavelength) yields a less abrupt frequency dependence that tends towards that of a planar reflection [42, 43], which significantly improves the inspection sensitivity. In other words, high ultrasonic centre frequencies that result in wavelengths small or comparable to the target defect size have the potential to yield optimised resolution and sensitivity in ultrasonic NDE.

However, in the case where high-frequency bulk waves are used for the inspection of TiMMC discs, the depth of the diffusion-bonded interfaces (≈ 100 mm) would mean that the high-frequency content of the ultrasonic pulse would be overwhelmingly attenuated as it propagates through the material [44, 45]. If the transducer is to be raster scanned for imaging purposes, this effect is exacerbated by frequency-dependent attenuation through the coupling medium, which would result in extremely limited high-frequency content reaching the surface of the component [46, 47]. Such an inspection would be hopelessly insensitive to the defects for which it was intended.

High-frequency *surface* waves can be used to inspect cross-sections of the diffusion-bonded interface [40], but this would mean that only the regions of the component where the interface meets the surface could be adequately interrogated. For the bonds present in a TiMMC disc, this restriction would imply that the vast majority of the interface would not be inspected (see Figure 1.4).

Clearly high-frequency ultrasonic NDE, in the form of either bulk or surface waves, is not suitable for this particular inspection problem. Assuming that the artefacts that any potential technique ought to be sensitive to are not found in isolation but are instead distributed over the diffusion-bonded interface, as would be expected if they are the result of initial surface rough-

ness prior to bonding, their aggregate response can be adequately detected using much lower and therefore more convenient ultrasonic centre frequencies [48].

Several researchers complement time-domain information obtained using more modest ultrasonic centre frequencies (< 25 MHz) with frequency-domain information that would otherwise be discarded [49–52]. This involves, for example, characterising the effects that different bond qualities have on the ultrasonic signal spectra and using this to define a profile against which all future inspections are compared [53]. Such approaches are feasible because the interstices that form between asperities on the opposing surfaces of an interface cause scattering of ultrasound, and this scattering is highly frequency dependent [54, 55].

However, all spectral analysis methods depend on the direct frequency-domain separation between defect signatures and material noise. This separation is regrettably not observed in Ti-6Al-4V diffusion-bonded components because the spectral content (both temporal and spatial) of the material noise is too similar to that of the defects to be detected [9, 28]. It should be noted that this lack of separation means that some otherwise useful time-domain analysis tools, such as spatial averaging [56] and spatial defect correlation [57], are equally unable to significantly improve the inspection capability [58].

As an alternative to direct spectral analysis, it has been suggested that examination of the resonance characteristics of the entire diffusion-bonded specimen can yield information about the interfacial stiffness [59]. For example, a standing wave can be generated in a specimen such that an anti-node coincides with the interface and thereby maximally stresses it, as shown in Figure 2.1. The quality of the bond can be deduced by observing the change in resonance frequency between this standing wave and one for which only a node is coterminous with the interface [59]. Though clearly immune to some of the problems mentioned above, the approach offers extremely limited sensitivity and is dependent on the diffusion bond lying in the middle of the component. If the interface is not centred, the relative positional offset is directly reflected in the error associated with the estimated interfacial stiffness, resulting in an extremely geometrically constricted inspection.

None of the processes discussed above are sufficiently suited to the inspection problem defined in Section 1.2. A more favourable approach, where material texture and poor bonding effects

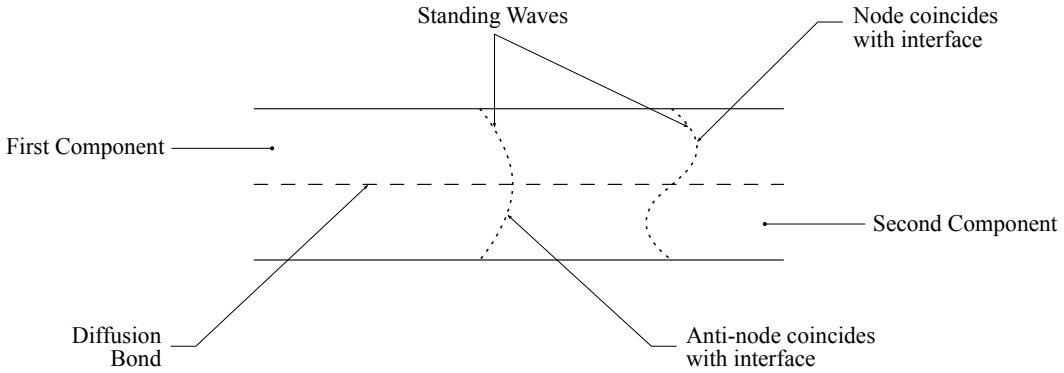

FIGURE 2.1 Low frequency (kHz) resonance technique used for the inspection of diffusion-bonded components. Standing waves are generated and their resonance frequencies compared in order to determine the interfacial stiffness. After [59]

are separated by analysing complex reflection coefficient pairs taken either side of a diffusion-bonded interface, was recently proposed by Milne et al. [14]. The technique used the Baik & Thompson imperfect interface model [60] to show that well-bonded and poorly-bonded samples could be separated via the signal phase changes induced by the interface.

This Baik & Thompson model, which is limited to the quasi-static modelling of interfaces containing a random distribution of cracks and inclusions (i) in a thin transition layer whose thickness is much less than the wavelength of the interrogating acoustic wave and (ii) whose self-resonance frequency (to be specified later) is much higher than the inspection frequency [60], has been used successfully by several researchers besides Milne et al. in disparate problem areas [61–64], including in the context of diffusion bonds [65]. According to the model, the reflection coefficient, R_1, is a function of the two acoustic impedances on either side of the interface, Z_i, the change in mass per unit area resulting from inclusions or pores at the interface, m, the angular frequency of the interrogating ultrasound, ω and, importantly, the interfacial stiffness per unit length, κ [60]:

$$R_1 = \frac{\left(\frac{Z_2 - Z_1}{Z_1 + Z_2}\right)\left(1 - \frac{m\omega^2}{4\kappa}\right) + i\omega\left(\frac{Z_1 Z_2}{\kappa(Z_1 + Z_2)} - \frac{m}{Z_1 + Z_2}\right)}{\left(1 - \frac{m\omega^2}{4\kappa}\right) + i\omega\left(\frac{Z_1 Z_2}{\kappa(Z_1 + Z_2)} + \frac{m}{Z_1 + Z_2}\right)}. \tag{2.1}$$

The appearance of the interfacial stiffness term in this expression can be exploited by noting that ultrasonic reflections from both sides of a solid-state bond comprise an asymmetric component (due to the step function in elastic properties across a perfect interface between dissimi-

lar materials) and a symmetric component (from boundary imperfections, whose ultrasonic signatures are approximately equal from either direction) to produce the double-sided inspection methodology illustrated in Figure 2.2 [66].

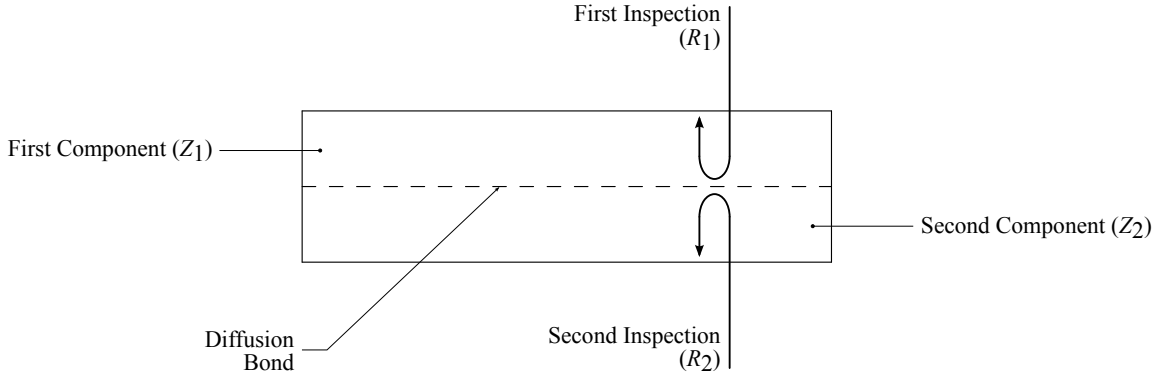

FIGURE 2.2 Double-sided ultrasonic inspection of titanium diffusion bonds. The reflection coefficients R_1 and R_2 are taken at identical positions along the interface from opposite sides, and their combination into symmetric and asymmetric components yields information about the condition of the bond. After [66]

In this configuration, the reflection coefficients from the two inspections, R_1 and R_2, can be combined under a quasi-static approximation ($\omega \ll \sqrt{4\kappa/m}$, where $\sqrt{4\kappa/m}$ is the self-resonance frequency of the spring–mass system) to produce symmetric (R_s) and asymmetric (R_a) reflection coefficients [66]:

$$R_\mathrm{s} = \frac{R_1 + R_2}{2} \approx \frac{i\omega}{\kappa} \frac{Z_1 Z_2 - m\kappa}{Z_1 + Z_2}, \tag{2.2a}$$

$$R_\mathrm{a} = \frac{R_1 - R_2}{2} \approx \frac{Z_2 - Z_1}{Z_1 + Z_2}. \tag{2.2b}$$

R_s is wholly imaginary and depends on the interfacial stiffness whereas R_a is independent of κ and is entirely real. The isolation of κ in this fashion implies that the phase difference between R_1 and R_2 contains interfacial stiffness information that can be used for the NDE of titanium diffusion bonds. However, the macroscopic anisotropy of Ti-6Al-4V causes pulse propagation times to vary throughout the material such that simple phase-spectrum point measurements comprise both an unpredictable phase delay component as well as the contribution from the inherent phase of the signal. Only this inherent phase, or 'true phase', contains κ information.

The true phase, Φ, can be isolated by noting that, for non-dispersive waves, a portion of the phase spectrum around the signal centre frequency is approximately linear. In this Region of Interest (RoI), the phase spectrum, φ, has a slope proportional to the time difference between the centre of the observation window and the half-energy point of the signal within it [67]. Extrapolation of φ_{RoI} to the zero frequency axis yields the phase-delay-independent true phase [68]. This procedure is shown in Figure 2.3, where the phase spectra of two otherwise identical signals having a 27 ns time of arrival difference (which causes a $\pi/2$ phase angle difference between them at the centre frequency, f_c) are shown to exhibit distinct linearity in the vicinity of the signal centre frequency. Linear regression of this region, which lies entirely within the bandwidth, B, yields the same Φ for both signals, as expected. Conversely, point measurements of the phase at f_c reflect the arrival time difference between the signals.

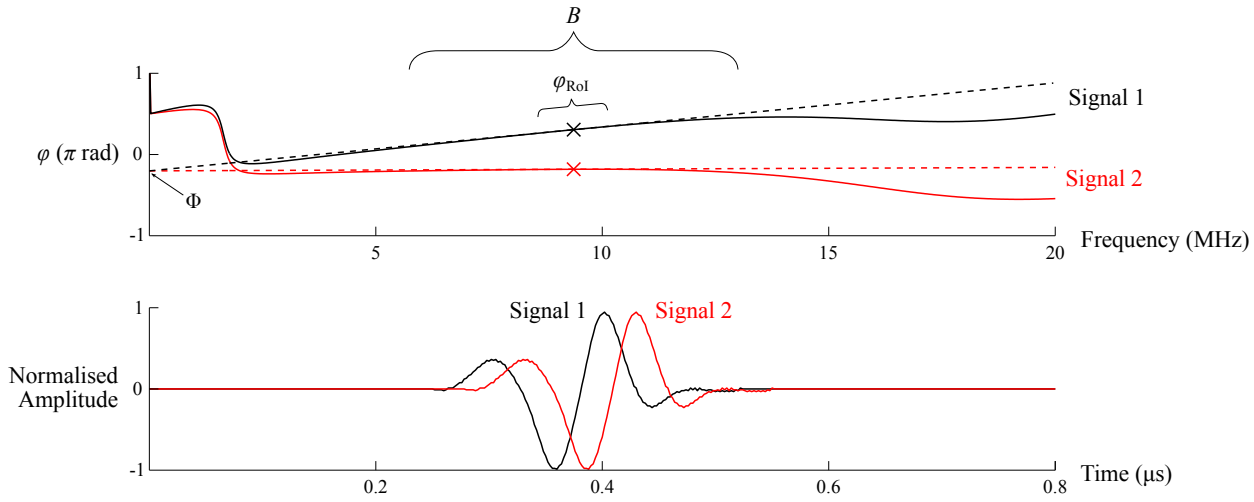

FIGURE 2.3 Phase spectra (top) for two identical signals with different arrival times (bottom). The phase delay difference between the signals is equivalent to $\pi/2$. Point measurements of the phase at f_c (crosses) reflect this phase difference, whereas true-phase measurements (dashed lines) eliminate this contribution

Milne et al. exploited true-phase measurements to assess the phase differences between R_1 and R_2 and thus produce a reflection coefficient whose characteristics in the complex plane yielded good separation between poorly-bonded and well-bonded samples [14]. However, it was not possible to reproduce this separation when there was access to only one side of the diffusion bond: the macroscopic anisotropy of Ti-6Al-4V resulted in phase measurement errors that could not be overcome by normal means when attempted from only one side. Despite this, the work showed

sufficient promise to warrant further investigation, the main findings of which are presented in Chapter 3.

2.2 Non-Linear Ultrasonic NDE of Diffusion Bonds

Although the results obtained using the imperfect interface model were encouraging, any resultant technique would be limited by the linear acoustic phenomena on which the model is based, and these are much less sensitive to microscopic material imperfections than counterpart non-linear interactions [35]. In light of this, it is reasonable in the name of completeness to evaluate non-linear ultrasonic methods with the aim of further improving inspection capability.

It is generally assumed that neither the density nor the elasticity of a medium depends on the amplitude of any acoustic wave it carries [69]. This assumption is only valid if the changes in strain, pressure, temperature and density resulting from the wave propagation are negligible, as is normally the case during conventional, linear ultrasonic NDE [33]. However, even relatively low-amplitude non-linear effects can be accumulated as acoustic waves propagate, particularly if there is low dissipation and weak dispersion, and this can yield substantial and measurable distortions of the propagating wave, efficient interactions between intersecting waves and other unconventional non-linear phenomena [69].

The non-linear stress–strain behaviour in isotropic materials is described by [70]:

$$U = \frac{1}{2!} c_{ijkl}\, \varepsilon_{ij}\, \varepsilon_{kl} + \frac{1}{3!} c_{ijklmn}\, \varepsilon_{ij}\, \varepsilon_{kl}\, \varepsilon_{mn} + \ldots , \tag{2.3}$$

where U is the strain energy density, ε_{ij} is the Lagrangian strain and c_{ijkl} and c_{ijklmn} are the second- and third-order elastic constants, respectively. This last set, the Third-Order Elastic Constants (TOECs), represent the predominant non-linearity in a material and are commonly expressed as the independent non-linear parameters A, B and C [71], which are a linear combination of the Murnaghan constants l, m and n [72]. A significant body of work has focused on exploiting acoustic waves to ascertain the TOECs of a given material in order to determine its integrity, and strong correlation between strength degradation and non-linear coefficients has been unambigu-

ously proven [69]. Practical NDE applications of this correlation rely on the relationship between lattice anharmonicity and perceived non-linearity, where greater measured non-linearity implies greater material imperfection [73]. There are three main mechanisms by which the degree of non-linearity can be measured: acousto-elasticity, harmonic generation and wave mixing [69].

Acousto-elasticity is the variation of ultrasonic wave propagation velocity with strain [74]. Generally, a material is stressed and ultrasonic velocity measurements are performed at positions and/or instances that are subject to different levels of strain. The dependence of velocity on strain allows the material non-linearity to be measured via a group of equations that relate the wave velocities for a given polarisation direction to the second- and third-order elastic constants [75]. The approach has been used to successfully determine the integrity of a variety of materials for which linear ultrasonic NDE has proven much less sensitive [76, 77]. However, successful experiments have so far led to very little industrial exploitation because obtaining accurate velocity measurements and loading the specimen to induce different levels of strain impose a number of restrictive requirements on the specimen geometry and experimental arrangement [77].

Harmonic generation is a well-studied alternative to acousto-elasticity in which loading the specimen is not a prerequisite to the non-linear measurement. Consider the non-linear longitudinal wave equation

$$\frac{\partial^2 u}{\partial t^2} = c_1^2 \frac{\partial^2 u}{\partial x^2}\left(1 + \beta \frac{\partial^2 u}{\partial x^2} + \ldots\right), \tag{2.4}$$

where c_1 is the longitudinal velocity in the linear medium and β is a function of the second- and third-order elastic constants, often referred to as the non-linear parameter. The solution to Equation (2.4) is of the form [71]:

$$u(x,t) = A_0 + A_1 \cos(k_1 x - \omega t) + A_2 \cos(2k_1 x - 2\omega t) + \ldots , \tag{2.5}$$

where ω is the angular frequency of the fundamental harmonic and k_1 is the longitudinal wave number. The non-linear parameter β can then be expressed as follows [78, 79]:

$$\beta = \frac{8A_2}{A_1^2 k_1^2 d} \tag{2.6}$$

where d is the distance over which the wave has propagated. Importantly, Equation (2.6) shows that, for a wave propagating over a given distance d, the non-linearity of the insonified material can be inferred from the relative amplitudes of the fundamental and second harmonics [80]. These second harmonics are generated by the distortions of the incident sinusoidal wave either by the lack of traction forces at an imperfect interface, which promotes its 'opening and closing' as the wave propagates [81,82], or by the non-parabolic potential of the lattice and/or dislocation motion at very low strain amplitudes, as well as other microstructural defects [83,84]. It has been shown in a number of different experiments that β is very sensitive to the condition of the material [85–87].

However, NDE techniques that exploit either acousto-elasticity or harmonic generation suffer greatly from difficulty in distinguishing between material and external (i.e. equipment, coupling medium etc.) non-linearity. Since external non-linearity is often greater in magnitude than that which arises from the material [88], the associated uncertainties with these techniques can be difficult to overcome. Some non-linear wave-mixing experiments, on the other hand, allow these two contributions to be separated spatially, spectrally and modally [89], making them a more attractive configuration for non-linear ultrasonic NDE than the approaches described above.

Wave-mixing occurs when a given interaction volume is correctly insonified with two waves, preferably of different frequencies and originating from non-collinear sources. In the absence of a diffusion bond or other interface, the material non-linearity within the interaction volume—as described by two of the three independent TOECs—manifests itself as the generation of additional waves which have propagation vectors and frequencies directly related to those of the original signals [90]. The correlation between this interaction and material degradation has been verified [91]. Manipulation of the wave equation, taking into account non-linear deformation terms in the general theory of elastic media, results in nine configurations in which this interaction is possible [92]. However, energy and momentum conservation, as well as physical limitations on the practical ar-

rangement, mean that one particular interaction configuration is most commonly employed experimentally: the case when two transverse waves mix and generate a longitudinal wave [91], as illustrated in Figure 2.4.

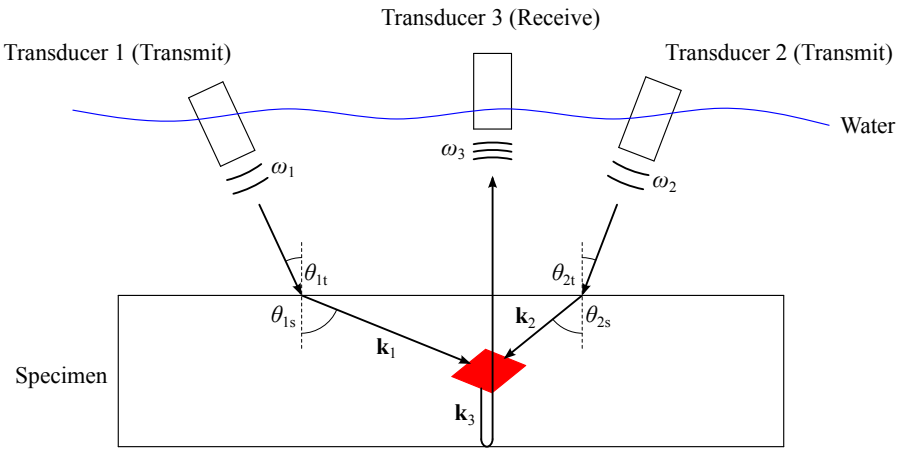

FIGURE 2.4 Immersion *shear* + *shear* → *longitudinal* wave-mixing experiment. The red parallelogram represents the interaction volume within which the third wave ($\mathbf{k}_3$, ω_3) is generated. After [91]

Whilst imaging material non-linearity is currently possible via harmonic generation [93] and harmonic generation techniques have been applied to diffusion bonds [94], the problem of eliminating unwanted contributions to the non-linear response from the surrounding system is yet to be convincingly overcome. Attempts to excite and detect at controlled regions of interest using time reversal and phase inversion methods yield some encouraging results [95], but this usually introduces other limitations on the inspection, such as being limited to near-surface applications only. The key advantage exhibited by the wave-mixing approach is the ability to image material non-linearity whilst largely eliminating unwanted non-linear contributions from external sources. This is achieved by:

1. spectral separation; whereby the injected signal frequencies ω_1 and ω_2 are selected such that the mixing signal frequency, ω_3, is not a harmonic of either input frequency,
2. modal separation; the detected third wave is a different mode (in this case longitudinal) from the incident waves,

3. spatial separation. Firstly, the non-linear interaction is limited to a region where the incident waves intersect and secondly; the mixing signal propagates in a controllable direction different from those of the incident waves.

In the arrangement shown in Figure 2.4, two shear waves are generated by mode conversion of the longitudinal pulses from transducers 1 and 2 as they impinge on the specimen surface at angles θ_{1t} and θ_{2t}, respectively. These angles are set according to the optimal total intersection angle of the shear waves within the material, $\Theta = \theta_{1s} + \theta_{2s}$, as well as the need to maximise shear transmission through the surface. Equations (2.7a) to (2.7c) show how Θ, θ_{1s} and θ_{2s} are calculated [90, 96]:

$$\cos\Theta = c^2 - \frac{(1-c^2)(1+a^2)}{2a}, \tag{2.7a}$$

$$\tan\theta_{1s} = \frac{a\sin\Theta}{1+a\cos\Theta}, \tag{2.7b}$$

$$\tan\theta_{2s} = \frac{\sin\Theta}{a+\cos\Theta}, \tag{2.7c}$$

where a is the frequency ratio ω_2/ω_1 and c is the shear-to-longitudinal velocity ratio c_s/c_l.

Since nothing can be done to affect c without altering the specimen, a first approximation to the ideal total intersection angle is obtained by selecting an appropriate frequency ratio. It is then possible to finely optimise the shear-wave interaction angles θ_{1s} and θ_{2s} by carefully adjusting ω_1 and ω_2, thus maximising the mixing signal amplitude. However, the so-called resonance condition, which can be understood as a phase matching condition akin to diffraction from a grating at an angle, imposes that [96]:

$$\omega_3 = \omega_1 + \omega_2, \tag{2.8a}$$

$$\mathbf{k}_3 = \mathbf{k}_1 + \mathbf{k}_2, \tag{2.8b}$$

such that changes to ω_1 and ω_2 must be accommodated at the receiving transducer both in terms of frequency sensitivity and spatial position. It is obviously most convenient for $\mathbf{k}_3$ to be orthogonal to the specimen surface, particularly for the 'single-sided' arrangement depicted in Figure 2.4.

Whilst the experiment described so far would indeed be sensitive to imperfections at a diffusion-bonded interface, the arrangement is optimised for maximising the response from the bulk material, i.e. that which relates directly to the presence of TOECs. It has so far been adequate to focus only on this contribution to the non-linear response as it is the most widely-studied source of material non-linearity. However, for the inspection of imperfect interfaces, the TOEC contribution is not as relevant as that of Contact Acoustic Non-linearity (CAN), which, if present, is the overwhelming source of non-linearity in a component [97].

CAN is caused by a reduction in traction forces at an imperfect interface [81]. More formally, CAN results from stiffness asymmetry across an interface as perceived by near-surface stresses, producing a 'clapping' motion when an ultrasonic wave traverses the material [98]. Researchers have previously exploited CAN for the NDE of imperfect interfaces by observing the amplitudes of the generated higher harmonics [99], but none have published results from attempts to excite CAN using non-collinear wave mixing. For the NDE of titanium diffusion bonds, it is clearly better to maximally reject the TOEC contribution whilst simultaneously retaining sensitivity to the CAN contribution. An additional key benefit of the wave-mixing approach is the selectivity it potentially affords in this respect, the promise of which is further explored in Chapter 5.

2.3 Summary

A review of the literature relating to the NDE of titanium diffusion bonds has shown that there is currently no self-contained solution to the inspection problem defined in Section 1.2. Linear ultrasonic techniques that exploit resonance, spectral analysis and signal processing have been shown to be inadequate, as have non-linear ultrasonic techniques that rely on acousto-elasticity and collinear harmonic generation. However, the foundations for at least two alternatives have been identified.

The first of these is based on the phase-spectrum analysis of signals reflected from a diffusion-bonded interface. This *linear approach* makes use of a phase measurement algorithm that eliminates the delay component of the phase calculation. It has been utilised successfully by Milne et al. on samples representative of the titanium alloy described in the problem definition [9], but there remain some obstacles that prevent its full industrial implementation. The technique:

1. produces complicated inspection results, which come in the form of complex reflection coefficient pairs whose interpretation is not intuitive in an industrial setting,
2. requires access to both sides of a diffusion-bonded interface. This is not possible for most of the diffusion-bonded components of interest here.

Points 1. and 2. are discussed in Chapter 3. A more intuitive metric for describing interface integrity is suggested via improvements to the existing phase measurement algorithm and a single-sided adaptation is proposed. The proposal and its practical implementation are evaluated and compared to the original approach in Chapter 4.

The second potential solution involves the non-collinear mixing of ultrasonic waves such that a spectrally, modally and spatially dissociable third wave is generated, the amplitude of which relates directly to the integrity of the material within the interaction volume. This *non-linear approach* has the potential to significantly increase the sensitivity of linear ultrasonic NDE techniques and has been used successfully for assessing plasticity and fatigue damage [91]. However, it:

3. has not been used for the inspection of imperfect interfaces and has so far been reported exclusively in terms of TOECs rather than the more relevant (in this case) CAN,
4. has only produced point measurements, with any scanning equipment and results not publicly reported.

These last points are both treated in Chapter 5, where a scanning non-collinear wave-mixing experiment is described and compared to conventional linear ultrasonic NDE using representative diffusion-bonded samples.

3. Linear Ultrasonic Approach

Milne et al. used true-phase measurements from both sides of an interface to distinguish between well-bonded and poorly-bonded specimens [14]. This was presented in the previous chapter as the most promising potential linear ultrasonic NDE solution to the titanium diffusion-bond inspection problem defined in Section 2.1. However, double-sided access to an interface in this fashion is generally not possible for Ti-MMC compressor discs and other safety-critical aerospace components. In this chapter, the work carried out by Milne et al. is built upon and made more practical with the aim of fully satisfying the requirements described previously using only a linear ultrasonic NDE approach.

A single-sided adaptation to the true-phase-based ultrasonic solution is developed and a more intuitive metric for describing interface integrity is suggested in Section 3.1. Section 3.2 comprises an analysis of various experimental and signal processing parameters that affect true-phase measurements, culminating in improvements to the existing phase measurement algorithm. A comparison between this improved methodology and the original work by Milne et al. is then presented in Section 3.3, followed by a summary of the key findings contained in this chapter in Section 3.4. The practical considerations pertaining to the newly-improved approach are treated in Chapter 4, where experimental results and comparisons with conventional ultrasonic NDE as well as the double-sided true-phase measurement technique are also presented.

3.1 Single-Sided Inspection

Single-sided ultrasonic inspections exploiting true-phase measurements, illustrated in Figure 3.1, are proposed to address the current lack in inspection capability. Two inspections are required as before, but in this configuration the first inspection is performed prior to diffusion bonding to acquire the reference true phase at each scan position, Φ_{ref}, which contains information about the material texture. This true phase is subsequently subtracted on a point-by-point basis from that of the second inspection, Φ, to yield the interface phase contribution Φ_{bond}.

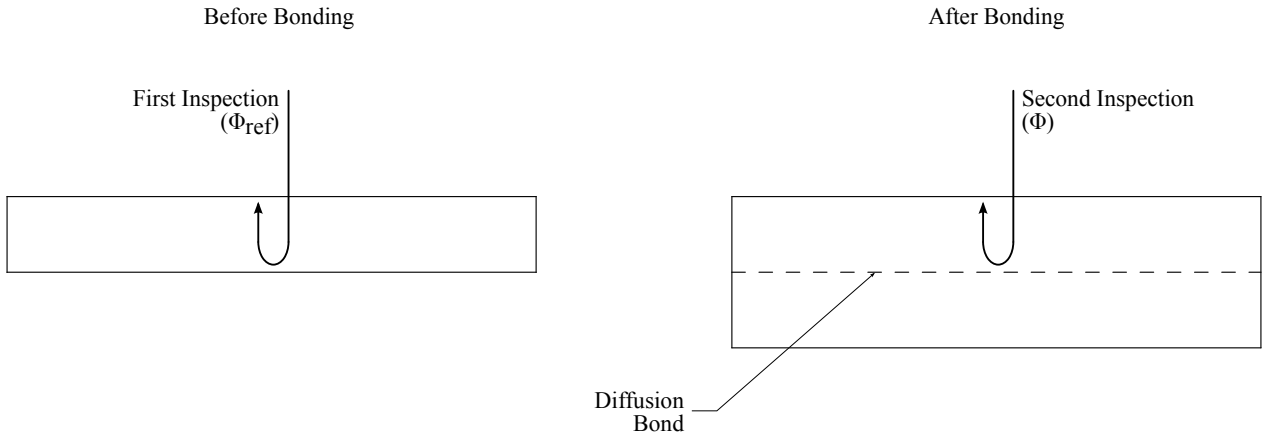

FIGURE 3.1 Single-sided ultrasonic inspection of titanium diffusion bonds. A reference true phase, Φ_{ref}, is measured prior to bonding and subtracted from the second inspection true phase, Φ, in order to isolate the true phase contribution from the interface, Φ_{bond}, at each scan position

The phase contribution from the interface can then be used to find a direct estimate of the interfacial stiffness. To illustrate this, it is convenient to introduce the harmonic mean of the acoustic impedances, Z:

$$Z = \frac{2Z_1Z_2}{Z_1 + Z_2}, \tag{3.1}$$

and the relative acoustic impedance mismatch, η:

$$\eta = \frac{Z_2 - Z_1}{Z_1 + Z_2}. \tag{3.2}$$

Then, from Equation (2.1) and given that the mass per unit area of the inclusions or pores at the interface, m, is zero for an interface consisting of an array of tight cracks [60], the reflection coefficient can be expressed as:

$$R = \frac{\eta + \frac{i\omega Z}{2\kappa}}{1 + \frac{i\omega Z}{2\kappa}}, \tag{3.3}$$

where κ is the interfacial stiffness.

Assuming that $\omega Z < \kappa$ such that the particle displacement discontinuity at the imperfect interface is negligible relative to the particle displacement, the real and imaginary parts of Equation (3.3) can be separated to yield:

$$\Re(R) \approx \eta, \tag{3.4a}$$

$$\Im(R) \approx \frac{\omega Z}{2\kappa}. \tag{3.4b}$$

As with the double-sided approach, κ only appears in the imaginary component of the reflection coefficient. It is therefore possible to formulate κ in terms of the measured Φ_{bond} by noting that $\tan(\Phi_{\text{bond}}) = \frac{\Im(R)}{\Re(R)}$ in the complex plane:

$$\kappa \approx \frac{\omega Z}{2\eta \tan(\Phi_{\text{bond}})}, \tag{3.5}$$

where Z and η are known material properties and ω is a known inspection parameter. Estimating the interfacial stiffness in this fashion may prove more useful for tangibly representing bond quality than the previous approach of formulating a complex reflection coefficient [27].

Note that the existence of ω as a factor in Equation (3.5) can be taken to indicate that interfacial stiffness estimates are inherently distorted by the frequency dependence (i.e. 'filtering') of the reflection coefficient. However, the group delay contribution from this filtering is very small compared to the wavelengths of concern here, as illustrated in Appendix A. The effect is a necessary consequence of attempting to obtain a phase angle that is independent of the relative position of

the observation window, but it is not a large enough effect in this situation to warrant correction of each individual measurement [100].

The range of possible values for κ given different interfacial acoustic impedance mismatches is shown in Figure 3.2, where it was assumed that $\rho = 4420$ kg m^{-3}, $c_l = 6.15$ mm µs^{-1} and $f_c = 10$ MHz. It is clear that the accuracy to which κ can be estimated is strongly dependent on the accuracy of the signal phase measurements.

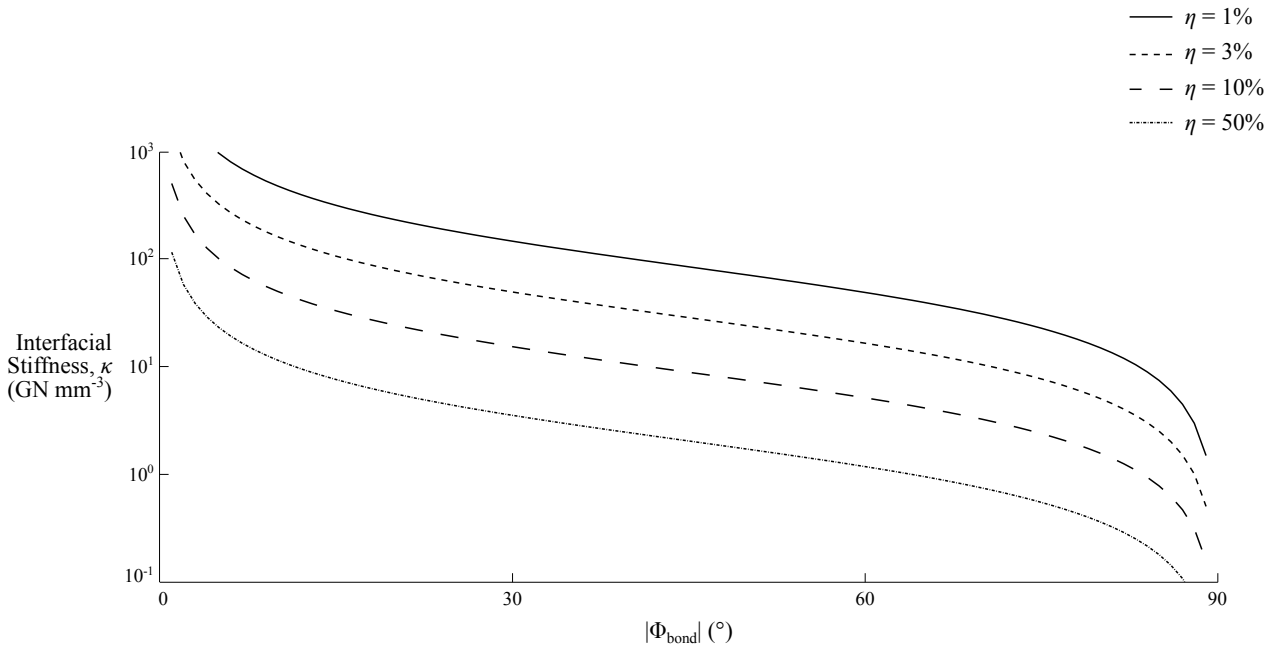

FIGURE 3.2 Variation of interfacial stiffness, κ, with the true-phase contribution from the diffusion bond, Φ_{bond}. Typical density and speed of sound values for Ti-6Al-4V titanium alloys were assumed: $\rho = 4420$ kg m^{-3}, $c_l = 6.15$ mm µs^{-1}. $f_c = 10$ MHz

It was recognised previously that macroscopic anisotropy causes ultrasonic signals propagating through material of uniform thickness to arrive at varying times, and this prompted Milne et al. to use a relatively wide observation window that captured all of the signals of interest without truncating them [14]. However, the ability to accommodate large variations in signal arrival time comes at the expense of phase measurement accuracy because wider observation windows introduce greater quantities of backscattered grain noise to the true phase calculation, thereby reducing its accuracy. The optimal conditions required to significantly improve measurement accuracy whilst retaining insensitivity to signal arrival time are outlined in the following section.

3.2 True-Phase Measurement Reliability

The phase measurement approach proposed by Milne et al., typified by the use of a relatively long observation window, is used here as a benchmark against which potential improvements are compared. Two signal processing parameters and four transducers were explored to find the optimal conditions for producing accurate true-phase measurements. Direct comparison between the different configurations was made possible by systematically evaluating the true-phase measurement standard deviation, SD_Φ, for a reference signal embedded in representative backscattered grain noise.

A forged Ti-6Al-4V block was inspected over a 50 × 50 mm area at a scan pitch of 250 μm to obtain the noise data, and a reflection from a titanium–water interface was used as the reference signal, which was scaled and embedded into the noise data at every scan position. The true-phase measurement standard deviation was calculated over the whole 50 × 50 mm area and this was repeated for each of the four transducers used. The scale factor for the reference signal was determined by the required 'peak-to-peak' Signal-to-Noise Ratio (SNR):

$$\mathrm{SNR} = 20\log_{10}\frac{A_{\mathrm{signal}}}{A_{\mathrm{noise}}}, \tag{3.6}$$

where A_{signal} is the signal amplitude and A_{noise} is that of the noise. Ten SNRs were explored, ranging from 6 dB to 20 dB. Figure 3.3 shows example waveforms for the lowest and highest SNRs used.

All scans were performed in a conventional immersion inspection system. The transducer focal spot was positioned at the same depth in the reference block at which the reference signals would later be embedded. The scan area was large enough to ensure that the captured noise was sufficiently spatially incoherent so as not to introduce systematic error and plentiful temporal averaging was employed to suppress electrical noise. The computation of SD_Φ was repeated at all ten SNRs for each transducer–parameter combination. The two true-phase measurement parameters were:

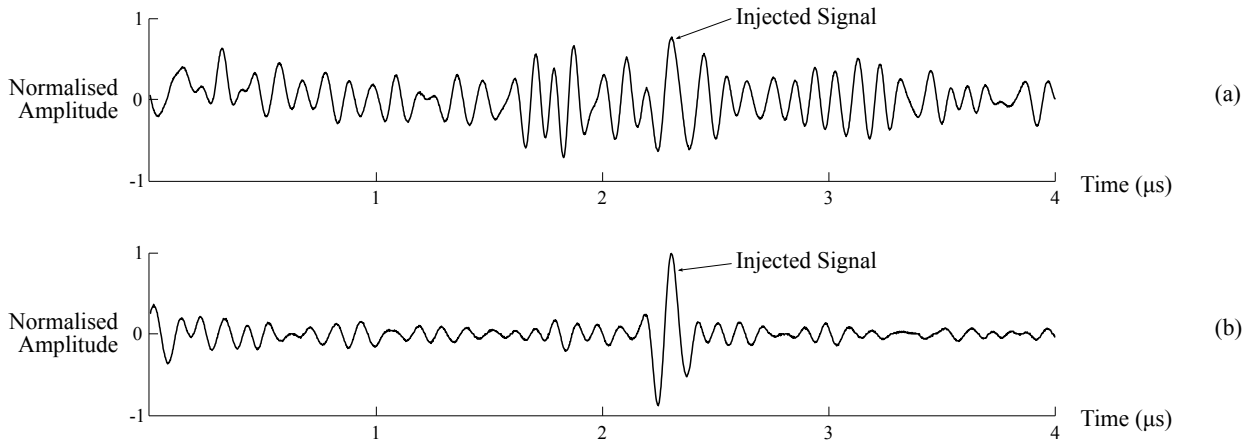

FIGURE 3.3 Typical waveforms with SNRs of (a) 6 dB and (b) 20 dB created by injecting reference signals (from a titanium–water interface) into representative backscattered grain noise

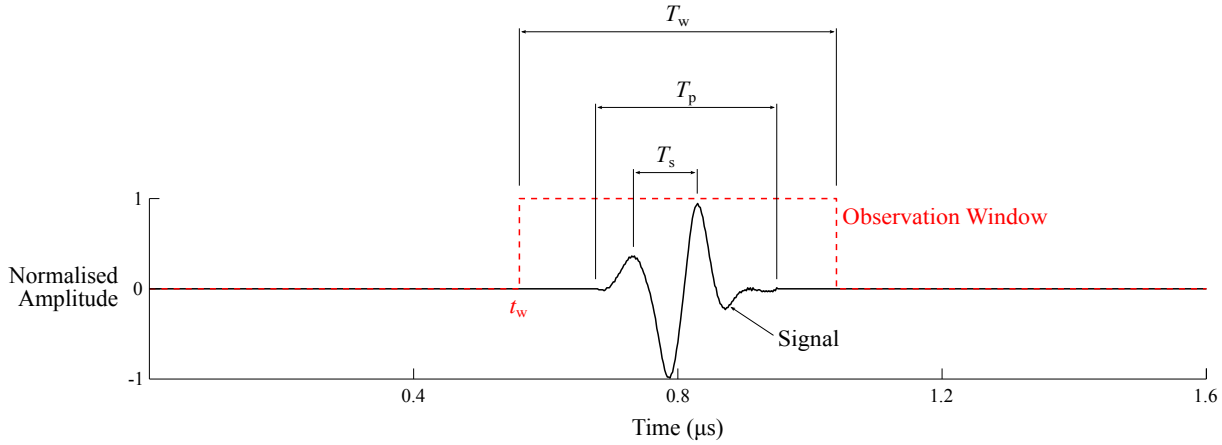

FIGURE 3.4 Definition of the various time domain parameters referred to in the text. T_s is the signal period, T_p is the pulse length, T_w is the observation or 'extraction' window length and t_w is its arrival time

1. Window length, T_w: length of the observation window used to 'extract' the diffusion bond signal (see Figure 3.4).

2. Phase-spectrum region of interest, φ_{RoI}: linear portion of the phase spectrum used to compute Φ (see Figure 2.3).

The four transducers, all being nominally 12.7 mm in diameter, were selected such that their centre frequencies and bandwidths were representative of those typically used in industry. Relevant characteristics are listed in Table 3.1.

Neither the optimisation of the parameters nor the relevance of the transducer characteristics have been treated in the literature. In the benchmark work, f_c was 10.9 MHz (signal period T_s =

TABLE 3.1 Main characteristics for the transducers used in these experiments. B is the absolute transducer bandwidth, B_n is the 6 dB-drop normalised bandwidth and F is the focal distance. Values were acquired using a glass reflector in water

Transducer	f_c (MHz)	T_s (ns)	B (MHz)	B_n (%)	F (mm)
A	4.73	211	3.75	79.4	60.0
B	9.25	108	7.48	80.9	82.5
C	4.85	206	2.47	50.9	111
D	15.6	64.1	13.9	51.7	126

92 ns), T_w was 480 ns (= 5.23 T_s) and φ_{RoI} was taken as the frequency range resulting from a 1 dB drop in the magnitude spectrum above and below f_c [14]. A simple rectangular window was used. The reasons for this choice are discussed in Section 3.2.3.

Note that the distinction between benign signals and those resulting from a poorly-bonded interface occurs as $\Phi_{bond} \rightarrow \pm 90°$ [14, 27] (although the interfacial stiffness is always positive, Equation (3.5) shows that Φ_{bond} is negative when η is negative). Assuming that phase measurement data are normally distributed, SD_Φ should be $< 15°$ in order to obtain sensible NDE capability. This is because such levels of uncertainty mean that 99.7% of measurements have an error less than $\pm 45°$, thus allowing a relatively reliable distinction to be made between 0° or 180° and $\pm 90°$.

The true-phase measurement reliability for transducer B using the benchmark parameters is shown in Figure 3.5. The figure shows that credible measurements using these parameters cannot be made when the SNR is below approximately 15 dB. For SNRs lower than this, the large SD_Φ values render any phase measurement too unreliable for estimating the interfacial stiffness. For example, at an SNR of 9 dB, which is a modest but not unreasonably low value, $SD_\Phi \approx 30°$. These levels of measurement certainty are unsuitable for the 'noisy' titanium alloy of concern here. Substantial improvements to SD_Φ can be obtained by optimising T_w and φ_{RoI}, as shown in the Sections 3.2.1 and 3.2.2.

3.2.1 Observation Window Length

In the benchmark work, window length was set according to the sum of the pulse length and maximum variation in signal arrival time over the scan area [14]. The effect of the resulting long windows on phase measurement accuracy was not investigated. In this section, window length, T_w, is

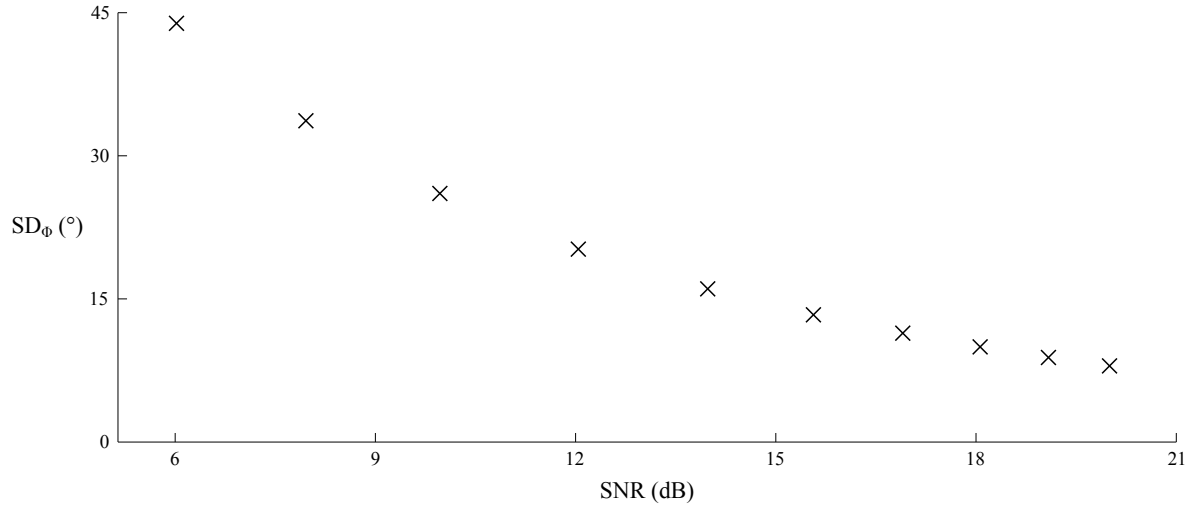

FIGURE 3.5 True-phase measurement uncertainty SD_Φ for the benchmark signal processing parameters ($T_w = 5.23T_s$ and $\varphi_{RoI} = 0.33B$) at various signal-to-noise ratios using transducer B

normalised with the corresponding signal period, T_s, of each of the four transducers and systematically varied to interrogate its effects on SD_Φ. Figure 3.4 shows how T_w, T_s and the pulse length, T_p, were defined.

For transducers A and B, Figure 3.6 shows that the least measurement uncertainty occurred when T_w was equal to T_s, regardless of SNR. The uncertainty of the measurements clearly increases with decreasing SNR, as expected, but it is never greater than 15° at $T_w/T_s = 1$ for the SNRs shown here. These results indicate that, for transducers A and B at least, the window length should always be set equal to the signal period (rather than the pulse length, for example) if phase measurement accuracy is sought. This finding is of interest because intuition would suggest that it is always better to capture as much signal data as possible, but these results reveal that a large proportion of the signal data should in fact be discarded in the interests of accuracy.

The results for transducers C and D are shown separately in Figure 3.7. It is clear that true-phase measurements with these transducers are significantly less reliable than with A and B. At high SNRs (20 dB), the lowest SD_Φ for A and B was 48% lower (better) than that of C and D. As the SNR decreased, SD_Φ increased more rapidly for C and D than it did for A and B. In addition, whilst the optimal T_w for transducers A and B remained the same ($T_w/T_s = 1$) regardless of SNR, the optimal T_w for C and D varied significantly with the relative noise level.

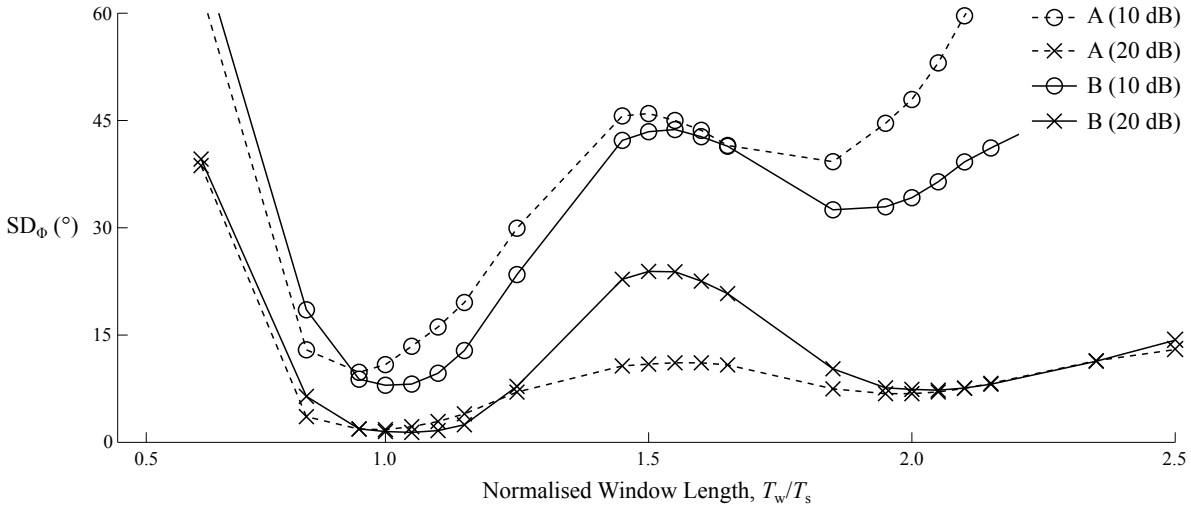

FIGURE 3.6 Measurement uncertainty variation with window length for transducers A and B at SNRs of 10 dB (∘) and 20 dB (×). Lines are for clarity and do not represent expected behaviour

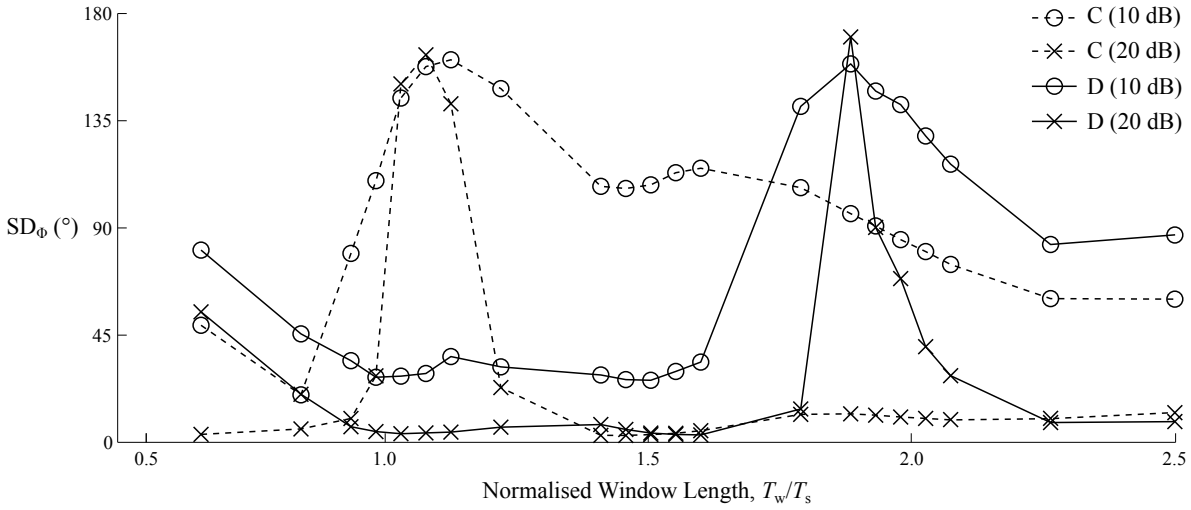

FIGURE 3.7 Measurement uncertainty variation with window length for transducers C and D at SNRs of 10 dB (∘) and 20 dB (×). These transducers do not exhibit SNR-independent minima: the optimal T_w depends on SNR. Note that the y-axis range is three times greater than that of Figure 3.6. Lines do not represent expected behaviour

The reason for the difference in performance between the two pairs of transducers is evident from Table 3.1, where the normalised bandwidths of C and D are shown to be much lower than those of transducers A and B. Note that spectral bandwidth is intrinsically related to temporal pulse length [101]. A lower B_n manifests itself as greater 'ring down' in the time domain [102], meaning that wavepackets contain several signal periods of similar amplitudes. For true-phase measurements where T_w is greater than the overall wavepacket length T_p (as was the case in the benchmark work), ring down is unimportant and the true phase by definition remains constant

despite variations in the relative positions of the window and the wavepacket within it. However, given that T_w should be made equal to T_s for increased measurement reliability, and that T_p is always greater than T_s in ultrasonic NDE, the position of the window with respect to the wavepacket is indeed relevant. Figure 3.8 shows that the measured true phase varies according to the window position, t_w, relative to the pulse when $T_w < T_p$.

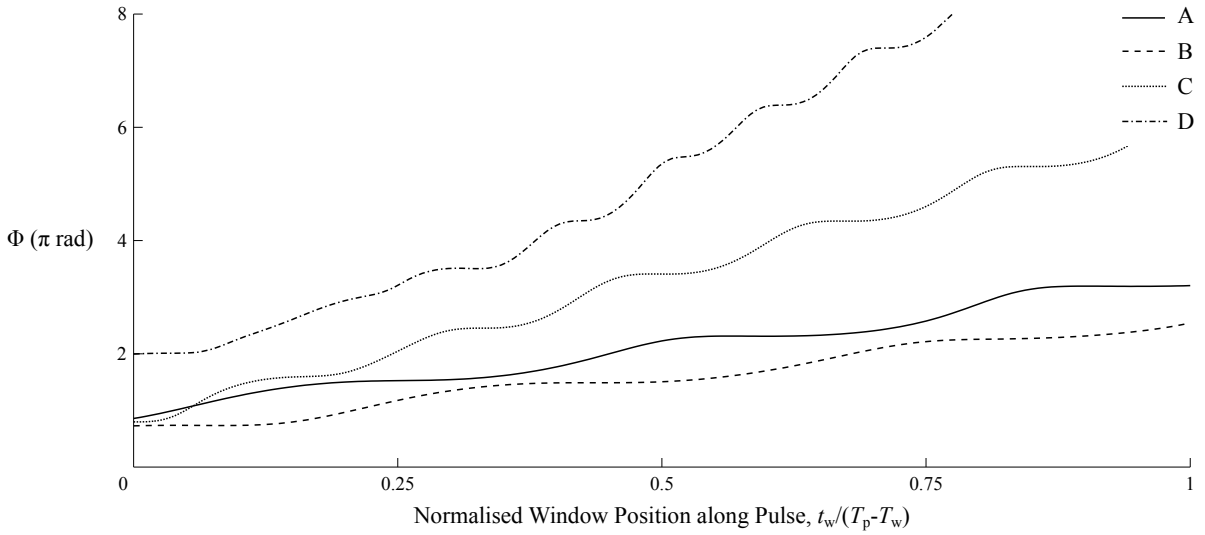

FIGURE 3.8 True-phase variation with window position along pulse. Unspoiled reference signals from each transducer were used, such that noise effects can be ignored for this comparison. $T_w = T_s$

For broadband transducers such as A and B, this dependence on t_w does not affect the precision of true-phase measurements because the slope of the phase-spectrum region of interest (φ'_{RoI}) is zero only when the window is positioned at one unique point along pulse. The slope is non-zero everywhere else, as shown in Figure 3.9. Seeking this zero-slope condition ($\varphi'_{RoI} = 0$) allows a unique true-phase to be defined for the signal and simultaneously minimises extrapolation error. However, for narrowband transducers like C and D, φ'_{RoI} is zero at several points along the pulse, as shown in Figure 3.10. The true-phase is different at each of these positions and therefore no unambiguous true phase can be defined, leading to large phase measurement errors. This indicates that broadband transducers are much better suited to true-phase measurements than their narrowband counterparts.

Overall, the results presented in this section have shown that an observation window length equal to the signal pulse duration yields significantly more robust true-phase measurements than

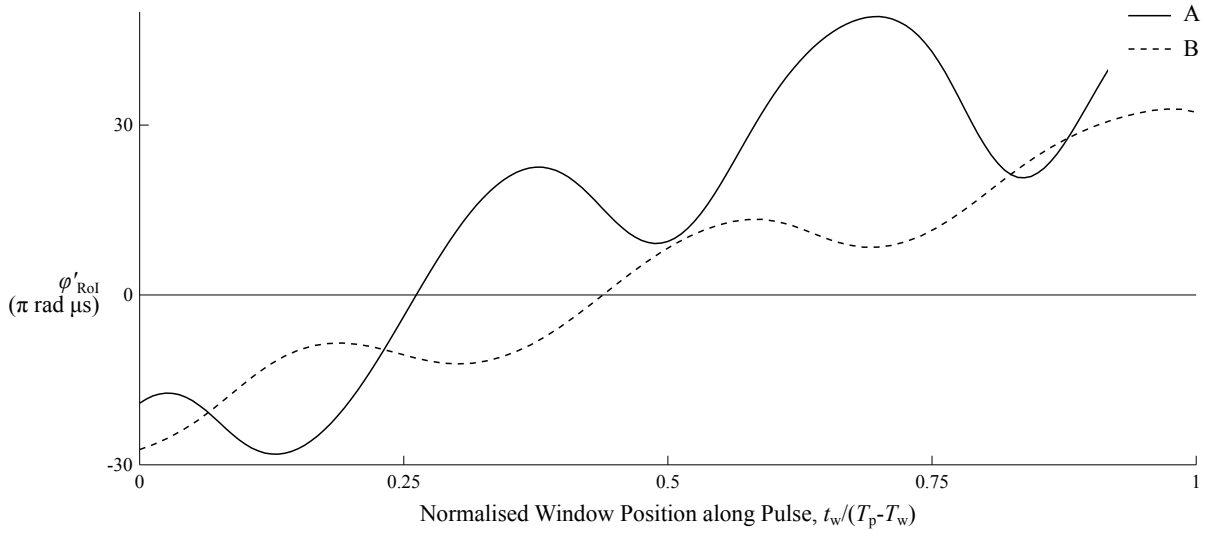

FIGURE 3.9 Region of interest slope variation with window position for transducers A and B, showing that there is only one point where $\varphi'_{\mathrm{RoI}} = 0$ in each case. Unspoiled reference signals used. $T_w = T_s$

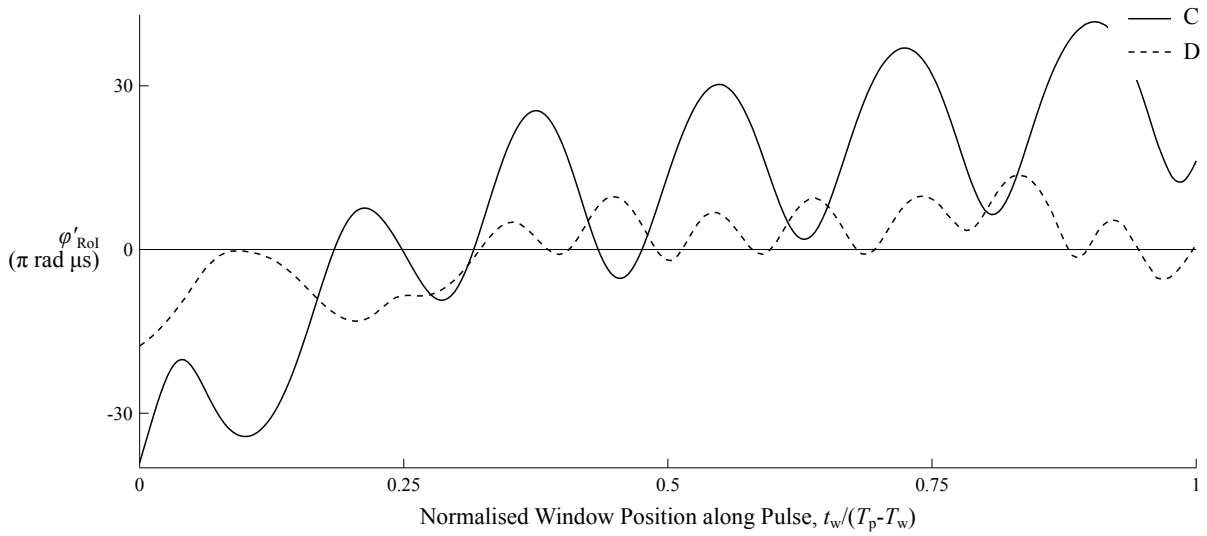

FIGURE 3.10 Region of interest slope variation with window position for transducers C and D, showing that there are multiple points where $\varphi'_{\mathrm{RoI}} = 0$ for both probes. Unspoiled reference signals used. $T_w = T_s$

the long windows used previously. This is a result of the pseudo-Gaussian shape of typical pulse envelopes, which means that the highest energy and better digitised (and therefore the most reliable) information in a pulse is received at a small region near its temporal peak. The local SNR is relatively low everywhere else, so it is beneficial to discard these error-inducing, low-amplitude pulse sections. In addition, and perhaps more importantly, by only extracting a single wavelength, the small variations in phase content that occur at the extremities of the pulse are also discarded, resulting in a more linear phase spectrum near f_c, as shown in Figure 3.11. That is to say, elimi-

nating the extraneous portions of a pulse has the effect of increasing the robustness of the linear regression required for finding the true phase because the tangent fitted at the centre frequency can be evaluated over large frequency range.

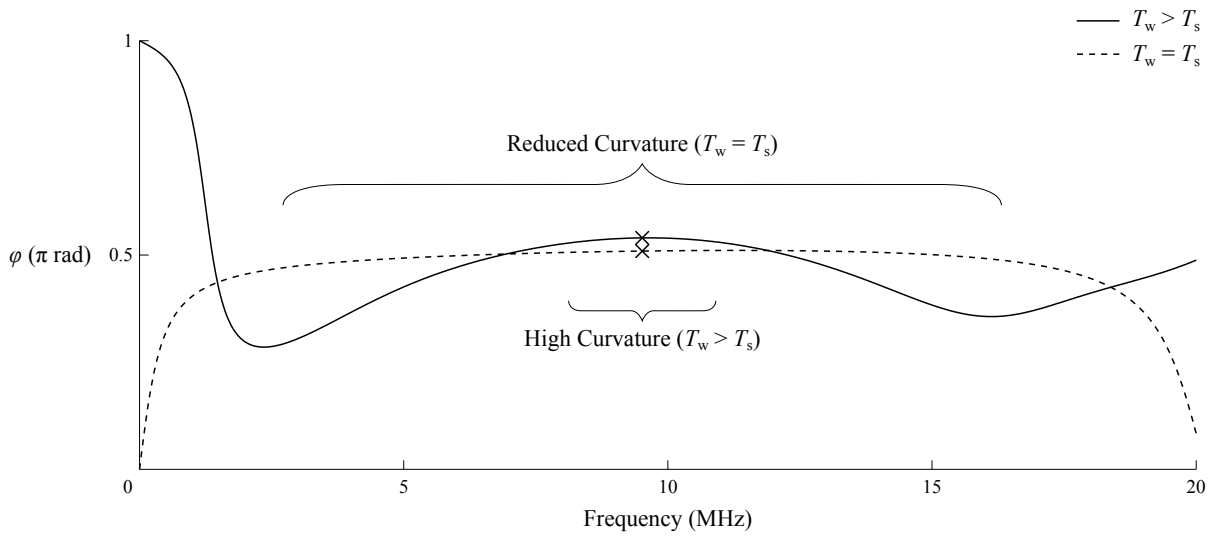

FIGURE 3.11 Phase spectra of reference signals from transducer B when $T_w = T_s$ (optimal window length—dashed line) and when $T_w = 5.23T_s$ (suboptimal window length—solid line). The length of the window relative to the signal period has a dramatic effect on the curvature of the phase spectra. The braces illustrate the regions over which the tangents to the spectra could potentially be fitted in both cases. $f_c = 9.25$ MHz, as shown by the crosses

However, this increase in measurement certainty requires broadband transducers that exhibit relatively low levels of ring down. Narrowband transducers can be used with integer multiples of T_s, but for every increase in window length the reliability of the phase measurements is dramatically reduced. Integer multiples of T_s can be used because this has the effect of averaging the φ'_{RoI} curve, incrementally reducing the number of points where $\varphi'_{RoI} = 0$. Evidence of this can be observed in Figure 3.6, where a second minimum in the measurement uncertainty is clear at $T_w/T_s = 2$ for both transducers. It should be noted that there are very few situations in which a narrowband transducer is essential: they are typically only used where increased ultrasonic energy output is much more important than bandwidth. Modern manufacturing technologies mean that it is now possible to obtain high-output-energy broadband transducers [103], so this bandwidth requirement should not unduly limit the practical exploitation of the suggested optimal parameters.

3.2.2 Phase-Spectrum Region of Interest

The other true-phase measurement parameter investigated here was the phase-spectrum region of interest, φ_{RoI}, which is the portion of the phase spectrum over which linear regression is applied in order to find Φ. Clearly, the more linear the phase spectrum around f_{c}, the more robust the linear regression and therefore the lower the SD_{Φ}.

It was shown in Figure 3.11 that T_{w} has a dramatic effect on the linearity of the phase spectrum. A relatively small φ_{RoI} was used in the benchmark work ($\approx 0.33B$) [14], probably because the linearity of the phase spectrum was limited by the long windows used. If a large φ_{RoI} had been used instead, this would have essentially amounted to linear regression over a complicated curve, which would have yielded even greater measurement error.

Shorter window lengths, on the other hand, result in reduced sensitivity to φ_{RoI} such that SD_{Φ} is only marginally affected by changes in the size of the phase spectrum region of interest. This is shown in Figure 3.12, where φ_{RoI} was normalised with the transducer bandwidth B and varied systematically over a broad range of values to examine its effect on SD_{Φ}. This analysis was only performed on transducers A and B since the errors for C and D were too great to be meaningful (for the reasons discussed in Section 3.2.1).

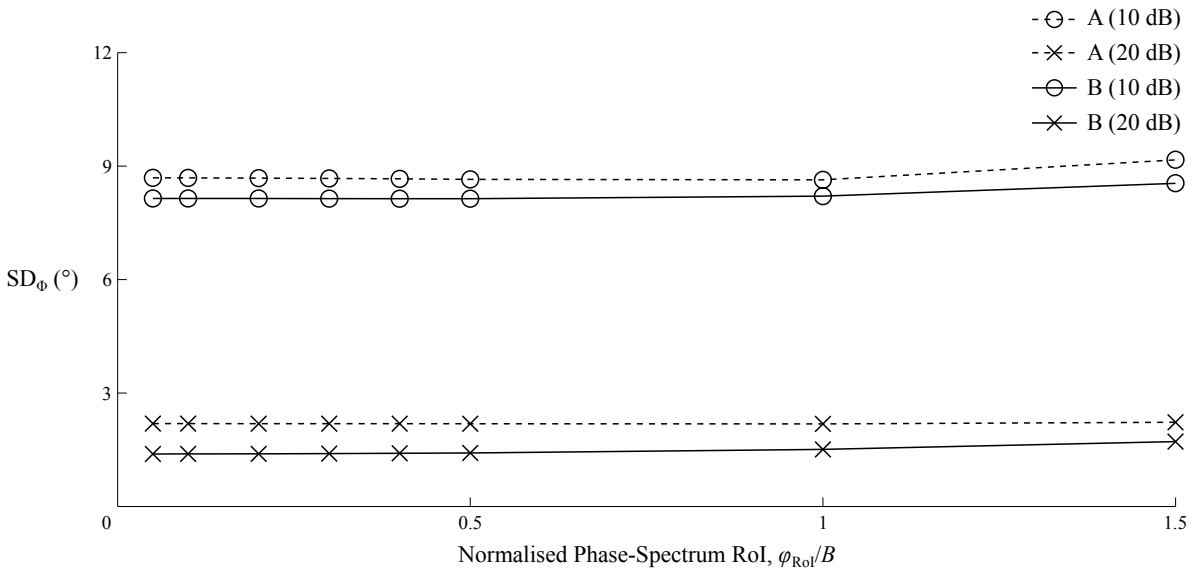

FIGURE 3.12 Measurement uncertainty variation with region of interest for transducers A and B at SNRs of 10 dB (∘) and 20 dB (×)

The figure shows that true-phase measurement accuracy is very insensitive to φ_{RoI} when $T_{\mathrm{w}} = T_{\mathrm{s}}$, highlighting the improved robustness introduced by the otherwise unintuitive approach of using a short observation window. Only a modest increase in SD_{Φ} was observed as φ_{RoI} increased beyond $\varphi_{\mathrm{RoI}}/B = 1$, corroborating the assumption that useful phase information is only found in a region close to f_{c} strictly within the transducer bandwidth.

3.2.3 Observation Window Shape

The shape of the observation window also has an effect on the true-phase measurement reliability, but this was not explored in benchmark work [14]. Although there is a large body of research in the literature covering the subject of 'windowing functions', only a little is said with regard to phase analysis. In this section, the use of a rectangular window in both the benchmark work and in the above experiments is explained.

Harmonic analysis of finite-duration data entails 'windowing' in order for the periodic extension of the data to be sensible. In all but the most trivial cases, the data will contain signals with periods not commensurate with the natural period of the observation interval, resulting in spectral leakage [104]. Windows are used to match discontinuities at the boundaries of the observation interval in order to reduce spectral leakage, but in doing so introduce losses (quantified by the coherent gain) and noise (quantified by the Equivalent Noise Bandwidth (ENBW)) [105]. Generally, a balance between these variables is sought, and certain types of windows can often be found in the literature alongside claims that they are optimised for certain applications because they improve on one at the expense of another [106]. For example, a Hann (raised cosine) window is a commonly-used windowing function, and comparison with a rectangular window shows that a 10 dB reduction in spectral leakage can be achieved if 37% coherent gain is sacrificed [105].

However, it has been noted in the literature that windows designed for accurate magnitude-spectrum estimation (e.g. Hann) may not necessarily be very effective at accurate phase-spectrum estimation [107]. Moreover, rectangular windows have been shown to distort the phase derivative, φ', to a much lesser degree than alternative window functions [108]. That is to say, where other window functions may be well-suited to situations where high dynamic range (i.e. low spectral

leakage) is of interest, a simple rectangular window is the optimal choice whenever the accurate representation of the phase spectrum is most important, as is the case here. Evidence to corroborate this is provided in Figure 3.13, where a Tukey (cosine taper) window was used to conveniently and systematically vary from a rectangular window (taper ratio = 0) to a Hann window (taper ratio = 1). The measurement standard deviation, SD_Φ, is again used as an indicator of parameter efficacy for the true-phase calculation. The figure clearly shows that rectangular windows yield the most reliable true-phase measurements regardless of SNR, as expected [109].

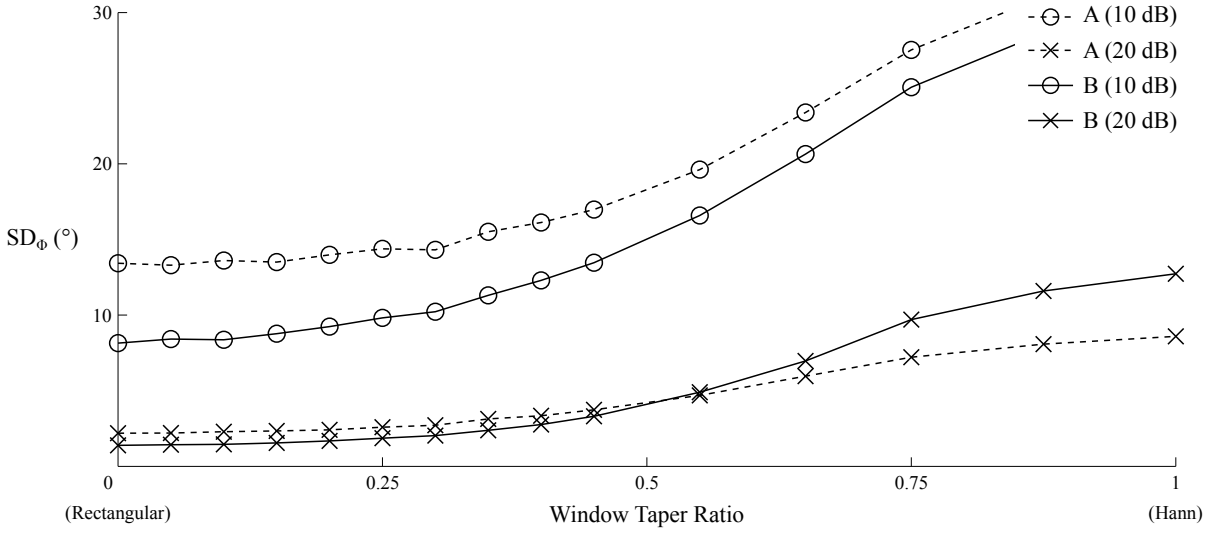

FIGURE 3.13 Measurement uncertainty variation with window shape for transducers A and B at SNRs of 10 dB (∘) and 20 dB (×). ($T_w = T_s$ and $\varphi_{RoI} = 0.1B$). Lines are illustrative only

3.3 Evaluation of Proposed Parameters

Having analysed the effects of both T_s and φ_{RoI} and justified the use of a rectangular extraction window, it is now possible to perform a full comparison between the benchmark work and the optimised parameters across a broad range of SNRs. Figure 3.14 shows the true-phase measurement uncertainty for transducers A and B using a window length equal to the signal period and a region of interest equal to 10% of the transducer bandwidth. The benchmark results are repeated here for convenience. It is clear that a substantial improvement in measurement reliability was obtained using the proposed parameters: as much as an order of magnitude reduction in the measurement

variance was observed for signal-to-noise ratios greater than approximately 10 dB. The uncertainty was reduced by smaller but still significant margins at low SNRs: a 30.6% reduction in SD_Φ was observed at SNR = 6 dB for transducer B, for example. Crucially, SD_Φ remains below the 15° 'threshold' value when the SNR = 9 dB using the new parameters, meaning that the range of SNRs at which phase measurements can be reliably made has been extended by at least 6 dB compared with the benchmark work.

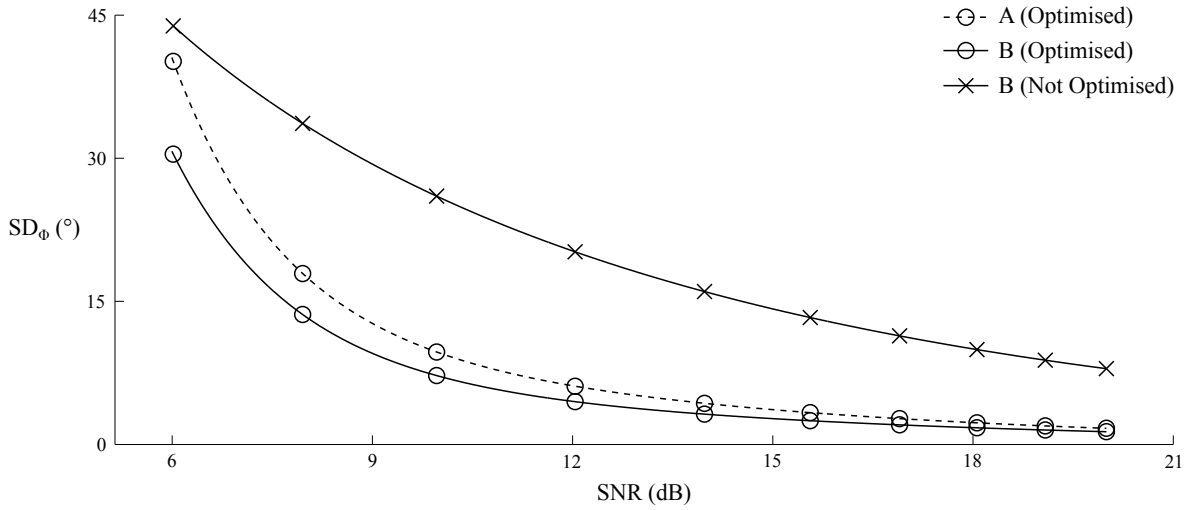

FIGURE 3.14 True-phase measurement uncertainty for transducers A (dashed line) and B (solid line) at various signal-to-noise ratios using optimised parameters ($T_w = T_s$ and $\varphi_{RoI} = 0.1B$). Benchmark results using the unoptimised parameters for transducer B are shown to ease comparison. Exponential fit curves are illustrative only

The reasons for the difference between the optimised and unoptimised results have been discussed. However, there is also a small but noticeable difference in SD_Φ between transducers A and B despite both being optimised with equivalent parameters. From Figure 3.14, it appears that B (f_c = 9.25 MHz) is more reliable than A (f_c = 4.73 MHz), particularly at low SNRs.

It is believed that the same phenomenon that prevented the optimisation of transducers C and D is also responsible for this small difference in performance: the normalised bandwidth of transducer B was 1.9% greater than that of A, resulting in A exhibiting slightly more ring down and a visibly more undulatory φ'_{RoI} curve (Figure 3.9). Under the increased influence of error-inducing noise at low SNRs, these greater undulations result in an inability to reliably find $\varphi'_{RoI} = 0$ and so measurement precision suffers. This suggests that, although extrapolating over greater frequency ranges invariably introduces greater measurement error, the benefits of increased bandwidth are

such that this extrapolation error can be reliably overcome. In other words, extrapolation error does not limit transducer centre frequency if the interrogating wavepackets have sufficient bandwidth.

3.4 Summary

A single-sided linear ultrasonic NDE approach for titanium diffusion bonds has been investigated and the true-phase measurements on which this technique depends have been analysed. Several signal processing parameters and experimental variables were systematically optimised in order to enable the reliable acquisition of true-phase data in 'noisy' environments like diffusion-bonded Ti-6Al-4V components. In particular, it has been shown that only a single period of the signal of interest should be extracted, and that this is most effective when broadband transducers are used. Narrowband transducers (having normalised bandwidths of approximately 50%) have been shown to perform poorly and should be avoided in phase analyses, whilst the selection of the transducer centre frequency should be based on the inspection requirements only given that the effect on true-phase measurement uncertainty is small compared to other variables.

The above findings are investigated practically in Chapter 4, where experimental factors are discussed and equivalence between the benchmark approach and the single-sided adaptation presented here is demonstrated.

4. Practical Considerations of Linear Approach

The work presented so far has demonstrated the robustness and accuracy with which true-phase measurements can be made, and has described how these might be used to predict the interfacial stiffness of diffusion-bonded titanium components. In this chapter, the practical aspects of such experiments are discussed, and pertinent temperature effects are addressed using samples manufactured specifically for this project. The computational code required to process the acquired data is described, and the single-sided approach is evaluated and compared with its double-sided counterpart.

4.1 Sensitivity to Signal Arrival Time

The short, rectangular window described in Chapter 3 clearly yields very reliable true-phase measurements across a broad range of SNRs. However, having the window length equal to one signal period and requiring that the pulse be broadband (to minimise ring down) mean that it is difficult for an automated system to reliably capture signals whose arrival times cannot be predicted. This difficulty was overcome by minimising the influence of the factors that act to reduce the spatial coherence resulting from the diffusion-bonded interface, as is explained below.

Ultrasonic inspections are normally 'threshold gated' (using a 'surface-following' gate) to allow the ultrasonic propagation time to and from any interface to be normalised even when this interface is not parallel with the scanning axes. This enables the user to focus only on the time range that is of interest, e.g. at a certain depth within a material. However, gating in this fashion (where the breach of a given threshold constitutes an independent datum to which each waveform is sep-

arately aligned) is not always reliable because small variations on the surface of the component can cause the gate to trigger earlier or later than expected, particularly in systems with limited dynamic range. In terms of automatically identifying diffusion bond signals, this inaccurate triggering spoils the spatial coherence introduced by the planar diffusion bond, making it difficult to identify the average signal arrival time.

To illustrate this, a diffusion-bonded specimen made from two cross-rolled Ti-6Al-4V plates was inspected over a 55 × 55 mm area at a scan pitch of 250 μm using transducer B. The specimen top surface was aligned with the scanning axes as much as was practically possible. Three different gating approaches were employed on this specimen, and the energies of the spatially-averaged diffusion bond signals for each are given in Figure 4.2. Only the portions of the waveforms containing diffusion bond signals are shown.

For the 'ungated' results of Figure 4.2(a), the diffusion bond signal energy was fairly broadly distributed in time and lacking a well-defined peak as a result of:

1. some inevitable misalignment of the specimen,
2. an inevitable amount of lack of surface flatness and
3. macroscopic anisotropy.

Cross-rolled material is typically more textured than forged material and therefore represents a worst-case scenario in these experiments. The total spread of the energy is approximately $3.4T_s$, making it impossible for a window of length $T_w = T_s$ to capture signals arriving at the extremes of this range.

Gating using the conventional threshold approach results in the diffusion bond signal energy distribution shown in Figure 4.2(b), where the distribution is narrower (approximately $2.6T_s$) and has a higher peak value than the ungated results of Figure 4.2(a). However, this slight improvement is still inadequate for window lengths equal to T_s. A much smaller range and an unambiguous peak in the energy distribution is required.

A gate that is able to adapt to the specimen geometry using a continuous mathematical expression is proposed in order to achieve this: inspections are performed without gating, but regions of the scan area which may serve as datums for alignment are identified before data analysis takes

place. These regions are spatially averaged locally to yield a set of datum waveforms. The waveforms are cross-correlated to a reference waveform such that relative delays between the scan axis and the specimen surface for each region are obtained. From this, a function that describes the shape of specimen surface can easily be computed.

As an example, consider the simple case of a single scan line over the length L. The datum regions could sensibly be taken as being centred at $L/8$, $L/2$ and $7L/8$, as shown in Figure 4.1. A number of waveforms are taken at each region and spatially averaged, yielding three representative waveforms from the middle and both extremities of the length L. Arbitrarily selecting the middle waveform as the reference, cross-correlation of the two remaining waveforms with this reference yields the relative delays, δ_{i}, between all three waveforms. These delays are then used to compute, for example, a quadratic function that describes the distance between the specimen and scan axis over the length L. The function is subsequently interrogated with each scan step to yield an array of delays that can be used to normalise all of the waveforms from the inspection, allowing the interface to be aligned without the artefacts that are present using threshold gating. Alignment in this fashion successfully mitigates the effects of specimen misalignment and lack of surface flatness.

In the diffusion-bonded specimen example described earlier, this process yields a much improved energy distribution, as shown in Figure 4.2(c). Here, the total spread of the energy in time is just $1.7T_{\mathrm{s}}$, and the peak of the distribution is well-defined and distinct, allowing a short window to correctly capture all of the diffusion bond signals across the specimen. It is clear that this procedure can be readily adapted to complex shapes and multi-dimensional inspections as long as suitable functions are used to described the specimen surface. In particular, this approach is well-suited to situations where misalignment can be significant and periodic, such as in the inspection of disk forgings using a turntable. Overall, these results show that short extraction windows can be exploited even in the presence of misalignment, lack of specimen flatness and, importantly, macroscopic anisotropy.

However, it is stressed that this does not imply that texture effects can be eliminated by gating algorithms, or that the use of adaptive gating procedures like the one described above render true-

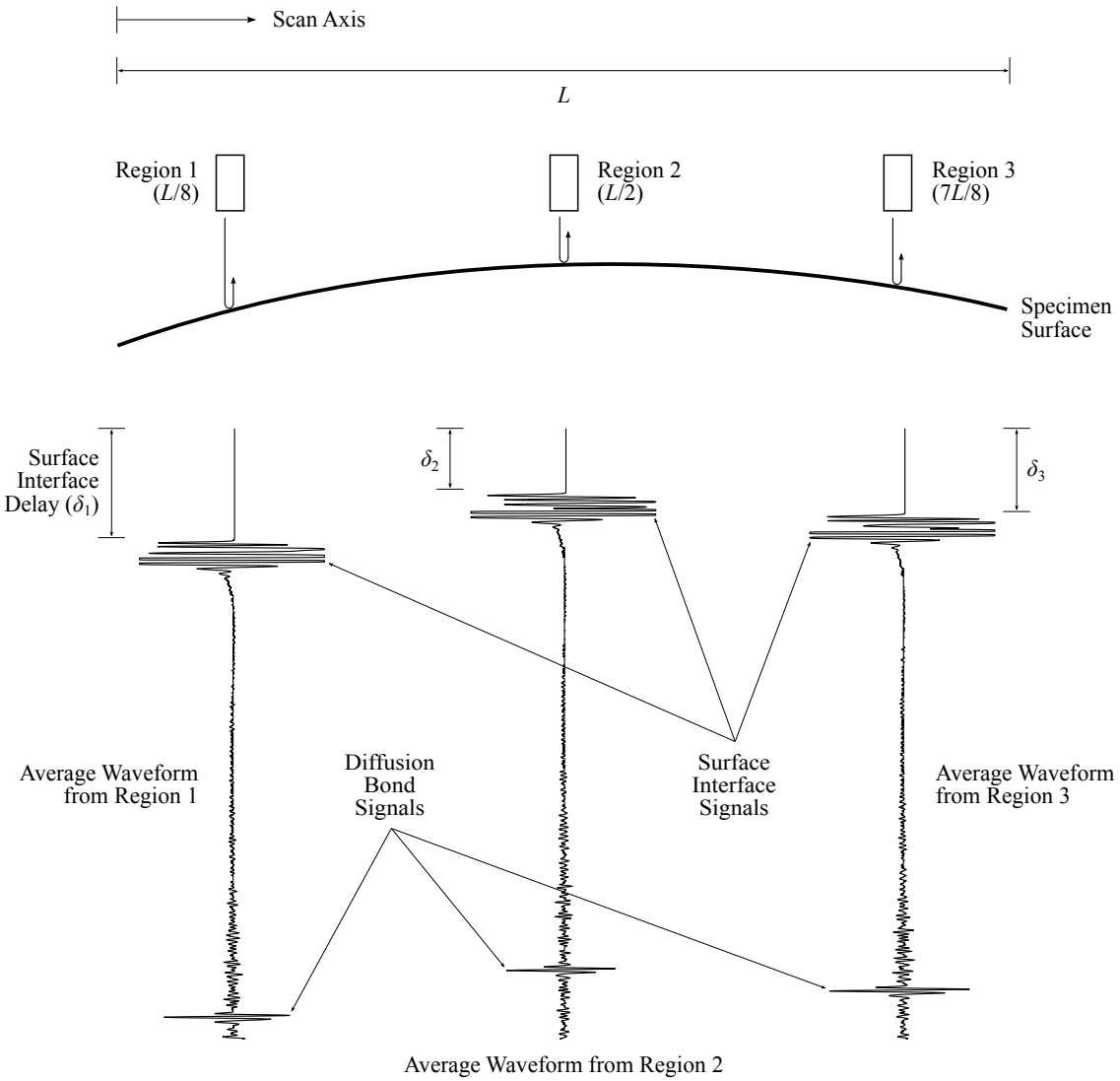

FIGURE 4.1 Example of an adaptive gating procedure. A number of regions, in this case three, are locally spatially averaged and cross-correlated to obtain the relative delay δ_i between the scan axis and specimen surface at each region. These relative delays are then used to describe the specimen surface over the length L

phase measurements obsolete. Though adaptive gating reduces the energy spread of diffusion-bond signals over a given area, even the most subtle of signal arrival time variations caused by macroscopic anisotropy would have the potential to produce meaningless interfacial stiffness estimates if the true-phase approach were not used. The remit of adaptive gating is only to allow the automated extraction of diffusion-bond signals accurately and robustly by maximising the spatial coherence introduced by the uniform nature of the diffusion-bonded interface. True phase calculations are still required to obtain useful interfacial stiffness estimates.

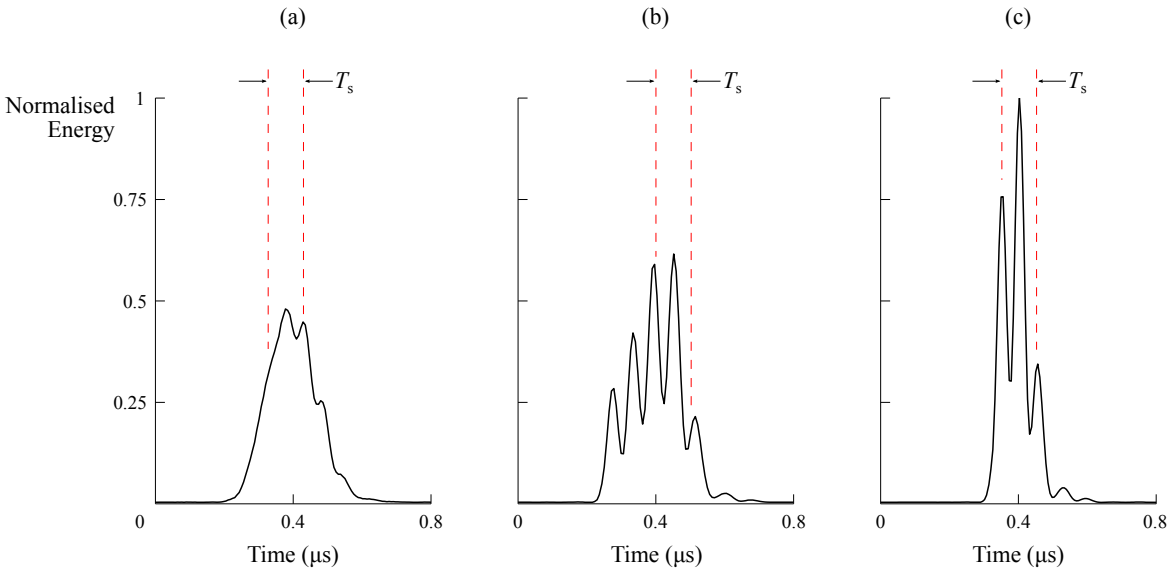

FIGURE 4.2 Energies of spatially-averaged diffusion bond signals for (a) ungated, (b) threshold-gated and (c) adaptively-gated inspection data, normalised to the maximum overall value observed. T_s is shown centred on the local maximum in each case, illustrating the potential position and length of a short extraction window. Adaptive gating yields a narrow energy distribution with a distinct peak, confirming improved diffusion bond signal spatial coherence. These results were obtained from a cross-rolled Ti-6Al-4V block exhibiting relatively high levels of macroscopic anisotropy. Waveform energy is proportional to the square of the amplitude, hence the 'rectified' appearance of these waveforms

4.2 Effects of Ambient Temperature and Annealing

The proposed single-sided technique promises greater robustness via optimised signal processing parameters. However, the sensitivity of the true-phase measurements to ambient temperature has only been reported for materials such as stainless steel [68], for which texture effects can be relatively small compared to those of Ti-6Al-4V. In addition, nothing has been said thus far about the effect of annealing on the reliability of the single-sided approach. This is relevant because the single-sided technique relies on a reference inspection performed prior to diffusion bonding (as described in Section 3.1). Diffusion bonding of titanium components involves annealing (at modest temperatures below β-transus) in order to induce cross-boundary grain growth and thus adhesion [110], but this may also cause small microstructural changes in the material. The result is that the reference true-phase measurement, Φ_{ref}, may not fully reflect the texture effects observed during the second (post bond) inspection, thus potentially limiting the ability to isolate the true-phase contribution from the interface, Φ_{bond}.

The sensitivity to both annealing and ambient temperature was explored by inspecting two sets of three forged Ti-6Al-4V blocks (9 mm thick) in a conventional immersion system. Each set of blocks was first inspected in a reference state and then re-inspected after either annealing or after varying the water temperature. The true phase of the back-wall signal was calculated at each scan position for all six blocks. The point-by-point absolute difference, $|\Delta\Phi|$, between the reference inspection and the subsequent scans was used as a measure of sensitivity to the variables. Each inspection was performed over the same 40×40 mm area of the blocks at a scan pitch of 250 µm using transducers A and B. The results are presented as the average of the absolute differences with error bars representing the standard deviation.

For the annealing experiment, the three Ti-6Al-4V samples were annealed as if they were being diffusion bonded for use in an aerospace gas turbine engine. The true-phase measurement difference between the post anneal and reference inspections was used as an indicator of the extent to which the annealing process affected the microstructure. The result for each sample as well as a combined average across all samples are presented in Figure 4.3. The figure clearly shows that the annealing process had a negligible affect on the microstructure of these blocks, producing less than 0.75° change in the measured true phase on average. Differences between the $|\Delta\Phi|$ values for transducer A and B can be attributed to differences in sensitivity to microstructure resulting from the different centre frequencies, focal distances and focal spot sizes of the two transducers. The results demonstrate that the texture information acquired via the reference inspection in the single-sided technique is not compromised by the diffusion bonding process, meaning that it can indeed be used reliably to isolate the true-phase contribution from the interface after the component has been diffusion bonded.

For the ambient temperature experiment, the lowest water temperature explored, 15.0°C, was arbitrarily taken as the reference state against which all other inspections were compared. The maximum temperature was 45.0°C. The inspections were performed in a water bath that had a temperature control accurate to 0.1°C and a circulation system that ensured uniform water temperature. A thermocouple, also accurate to 0.1°C, was attached to the side of the blocks and ample time was allowed to ensure that the centre of the blocks reached the temperature of the surrounding fluid before each inspection.

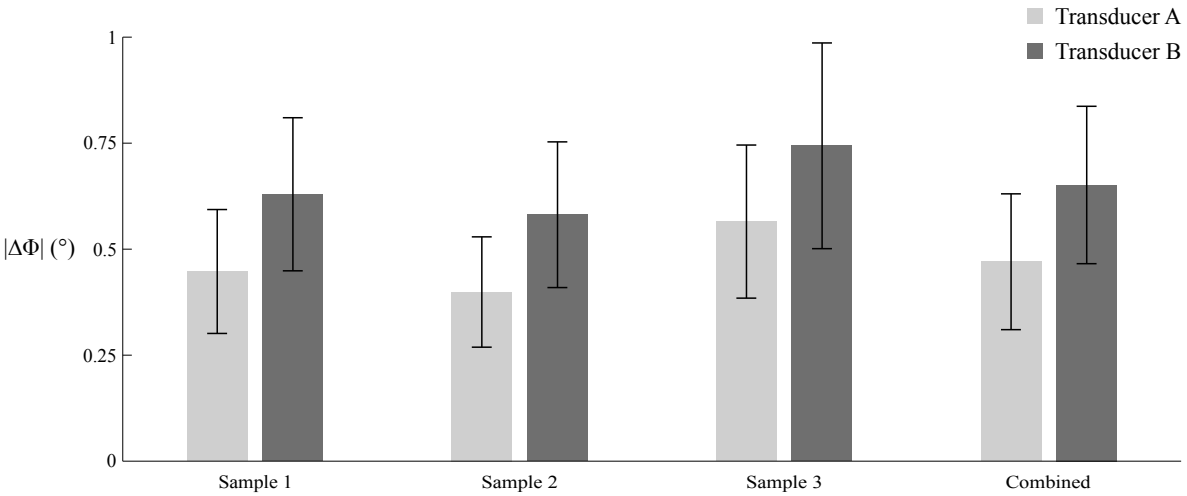

FIGURE 4.3 Absolute true-phase measurement variation resulting from annealing Ti-6Al-4V blocks as per the diffusion bonding process. Error bars show one standard deviation

Figure 4.4 shows that both transducers exhibited monotonically increasing measurement differences as the water was heated. These differences constitute an error in the true-phase measurement because it is impossible to predict the effect that a given temperature change imparts locally on the true phase. In contrast to relatively untextured materials such as stainless steel [68], the effect of ambient temperature variations on textured materials such as Ti-6Al-4V is clearly not negligible. This is because the speed of sound variations induced by temperature changes, a phenomenon common to all materials [111], manifest themselves in textured materials as variations in phase modulation. The true phase detected at the transducer, which acts as a phase averaging device over its aperture [19], is a function of the total insonified volume and the phase aberration effects encountered therein, which, as stated above, vary unpredictably with temperature.

On one hand, the results highlight that true-phase analysis is highly efficient at mitigating thermal instability: assuming that a 30°C increase in temperature causes a 0.6% decrease in sound velocity, the increase in the two-way propagation time through the blocks from the experiments is 0.024 µs. At 9.25 MHz (transducer B), this causes approximately 80° absolute phase angle drift, which is a factor of eight more (worse) than the 10° true-phase shift caused by the same 30°C temperature change in Figure 4.4.

On the other hand, this effect depends heavily on the transducer centre frequency, focal distance and focal spot size. Furthermore, and more importantly, this greater mitigation of thermal

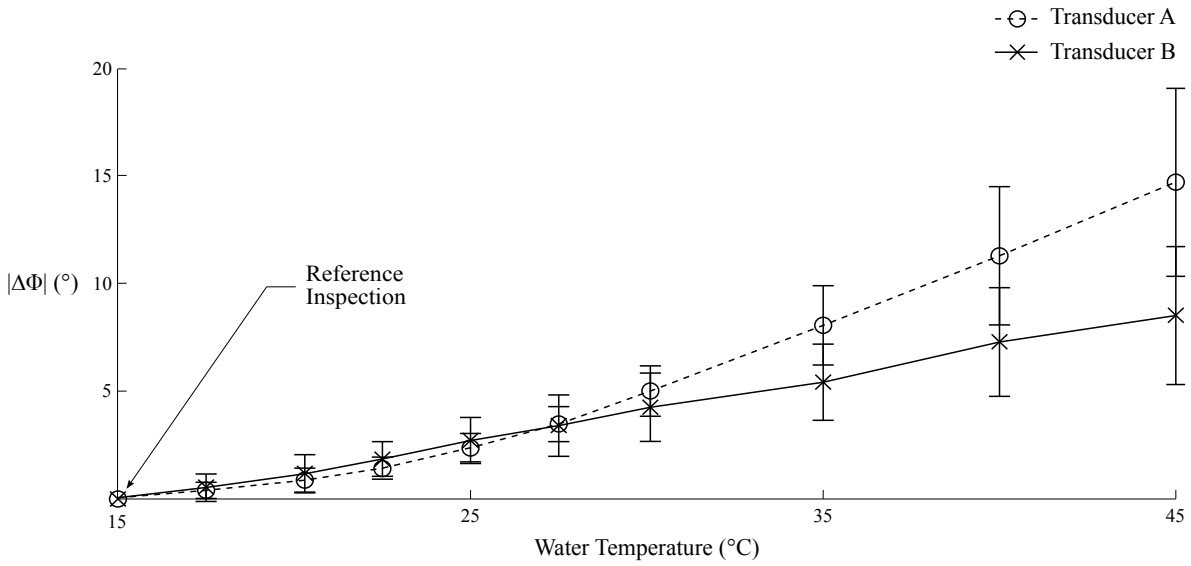

FIGURE 4.4 Absolute true-phase measurement variation with water temperature for transducers A and B. All values are average differences (calculated at each scan position for three forged Ti-6Al-4V blocks) with respect to the reference inspections performed at 15°C. The remnant true-phase drift is larger for transducer A than it is for B as a result of differences in the temperature-dependent sensitivity to microstructure resulting from the different centre frequencies, focal distances and focal spot sizes of the two transducers. Error bars show one standard deviation. Lines are illustrative only

instability does not negate the need for adequate temperature control, as the results clearly show: 10° additional true-phase measurement uncertainty is significant in the context of differentiating between well-bonded and poorly-bonded interfaces.

Based on the results presented here, it is suggested that the temperature be controlled to within perhaps ±2°C during phase-based inspections of textured materials. This requirement, whilst undesirable, should not notably diminish the usefulness of NDE approaches that rely on true-phase measurements given that temperature control is already common practice in ultrasonic NDE [37].

4.3 Practical Implementation

In this section, the process of obtaining the single-sided interfacial stiffness map for an arbitrary component is outlined in its entirety. It is assumed, for brevity, that the final component comprises two simple diffusion-bonded blocks, but the process can be readily adapted to more complex geometries.

The adherends are first machined and polished to the specification determined by the Hot Isostatic Press (HIP) cycle that they will undergo. They must then each be given unique identifiers and one must be selected as the reference block through which both interface inspections will be performed, as illustrated in Figure 4.5. For complex geometries, the choice of reference adherend is governed by the access issues discussed in Section 1.2. The chemical etching process that usually takes place immediately before HIP is deferred until after this reference inspection takes place. Etching removes remnants of the recast layer and ensures that the interface is clean prior to bonding [4]: insufficient material is removed to affect the true-phase reference measurement. It is stressed that robustly aligning the reference block is crucial if the first and second inspection data are to be brought together fruitfully. For this project, a simple jig was manufactured to ensure that the same volume was insonified during each inspection (see Appendix B), though clearly more automated solutions are possible.

The acquired data is processed to yield the interfacial stiffness map used to determine the integrity of the bonded component. The algorithm this entails is described in Figure 4.6 and relevant code is provided in Appendix C. Further to the temperature control requirement stated in the previous section, it is important to note that the need to perform one inspection before and another after diffusion bonding gives rise to four risks that are unique to the proposed inspection technique:

1. the reference data may be lost or corrupted before it can be used to isolate Φ_{bond},
2. the transducer with which the reference inspection was performed may be damaged or lost before the second inspection is due to take place,
3. the operator performs the computational analyses with discordant data sets,
4. the two inspection data sets are not properly aligned.

Nothing can be done to salvage the inspection if the reference data is lost before the interfacial stiffness is computed, so it is imperative that all reasonable efforts are made to safely store the reference data during the considerable time that separates the two inspections.

In the case of the unavailable transducer, however, it may be possible to perform the second inspection with a nominally identical transducer and normalise the resultant output. This could

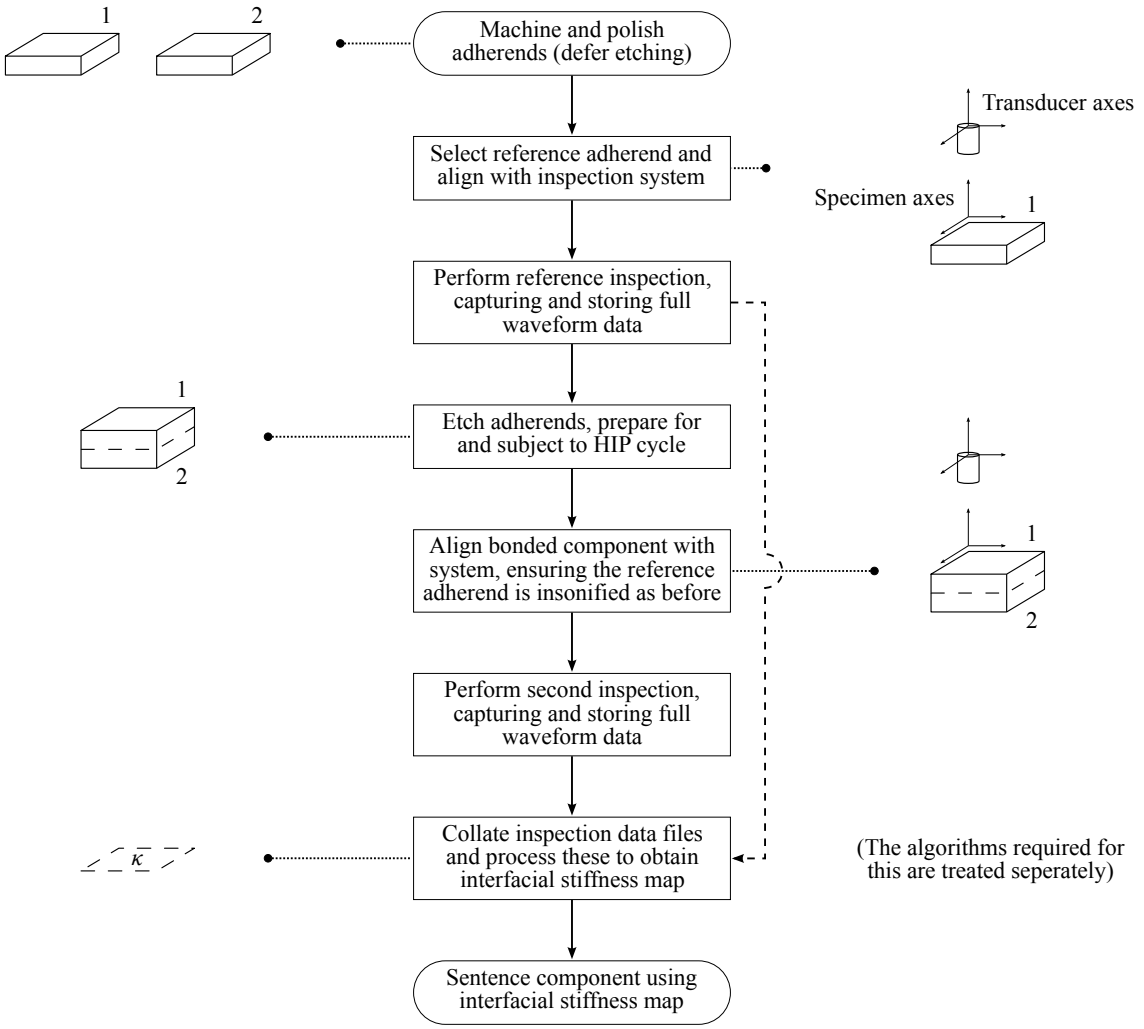

FIGURE 4.5 Overall procedure for sentencing a component having undergone single-sided ultrasonic NDE using true-phase measurements

most readily be achieved if the original probe had been fully characterised in terms of true phase, focal spot size, focal length and frequency response beforehand. Such characterisation can be incorporated into the process depicted in Figure 4.5, though it should be noted that the efficacy of normalisation in this fashion is yet to be demonstrated. In terms of operator error when manipulating the data files, industrialisation of the technique should take into consideration restrictions in the user interface to mitigate this risk. Finally, the risk arising from the technique's sensitivity to alignment errors between the two inspections can be abated by the proper use of jigs and tooling, as was the case in these experiments.

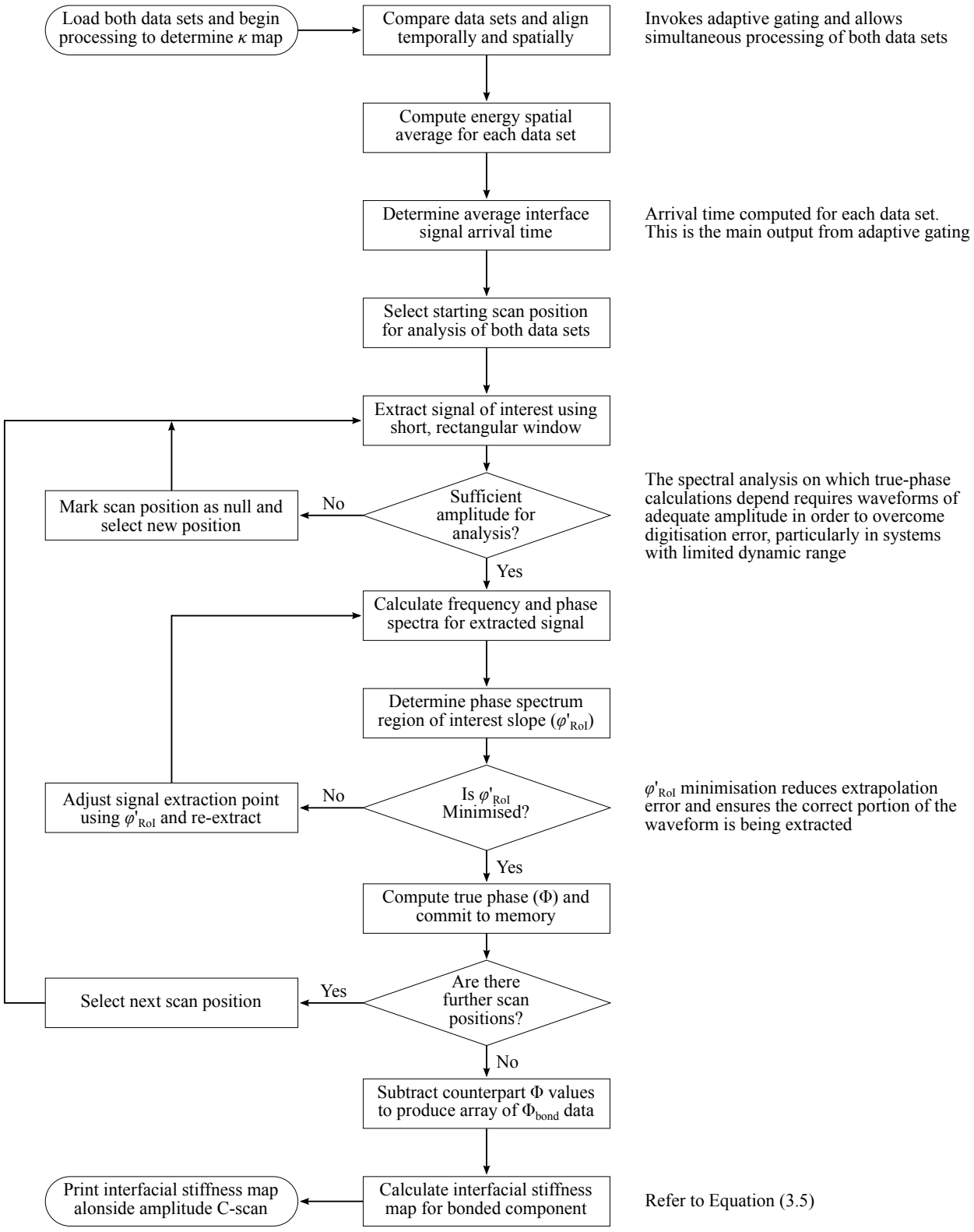

FIGURE 4.6 Computational algorithm for determining the interfacial stiffness map of a component from its single-sided inspections before and after HIP

Overall, it is clear that the relatively complicated nature of the proposed technique introduces new risks to the ultrasonic inspection problem. It is important to bear this in mind when assessing the technique and comparing it to alternative NDE methods.

4.4 Evaluation of Single-Sided Linear Technique

An optimised methodology that allows accurate true-phase measurements to be made in spite of a series of complicating factors has been described. As a result of these optimisations, a single-sided inspection for diffusion-bonded titanium components using signal phase is now possible. The experiment necessary to verify the equivalence of the single- and double-sided approaches is described below.

Forged Ti-6Al-4V blocks were used to create 25 diffusion-bonded specimens, each with a different bond quality as determined by contaminants placed within the interface. An overview of the contaminants used and the method of application to the specimens is provided in Table 4.1. Six of the specimens were not contaminated prior to bonding as they were intended to be well-bonded control samples. However, two of these did not successfully complete the Hot Isostatic Press (HIP) cycle and exhibited poor diffusion bonds. The remaining samples were contaminated with either particulates or residue from substances that could potentially affect the integrity of Ti-6Al-4V diffusion bonds in a typical industrial setting. These were:

1. Ardrox 6333: low foam alkaline cleaner used widely in industry. A concentration of 6% (diluted with deionised water) was used in these experiments.
2. Ceiling tile: scrapings from generic ceiling tiles were collected and passed through a 53 μm sieve to yield a fine powder.
3. MgO: mineral used widely in industry and domestically. A fine powder, also passed through a 53 μm sieve, was used here.
4. Orthosil F2: another widely-used alkaline cleaner and degreaser. 6% concentrate (diluted with deionised water).

5. Tensol-12: solvent-based adhesive found commonly in industrial settings. A concentration of 50% (diluted in high-purity dichloromethane) was used.

TABLE 4.1 Contaminants used in these experiments to obtain different bond qualities in 25 diffusion-bonded Ti-6Al-4V samples. Contamination was performed in an ISO7 class clean room facility [112]. Single pipette drops were used to 'stain' 12 of the samples, whilst another 7 were contaminated using fine particulates (passed through a 53 µm sieve) to an extent that could feasibly remain undetected in a normal industrial production environment

Contaminant	Morphology	Application	No. of specimens	Additional Notes
None	-	-	2	HIP cycle disrupted
None	-	-	4	Control specimens
Ardrox 6333	Residue	Pipette drop	6	-
Ceiling tile	Particulate	Controlled dusting	4	-
MgO	Particulate	Controlled dusting	3	-
Orthosil F2	Residue	Pipette drop	3	-
Tensol-12	Residue	Pipette drop	3	-

Each specimen contained a 101.6 × 25.4 mm diffusion-bonded interface, but only an area of 20 × 12 mm was contaminated in each sample, as illustrated in Figure 4.7. The seeding of the contaminants was performed in an ISO7 class clean room facility [112] to minimise the risk of extraneous uncontrolled substances being embedded in the interface. It was not possible to accurately quantify the contaminants embedded in each specimen because the low volumes used proved impossible to measure. Instead, the seeding process was designed to generate a contaminant distribution that could feasibly pass undetected during the typical manufacture of diffusion-bonded titanium components [113].

The specimens were inspected using transducer B at a scan pitch of 250 µm. An interfacial stiffness (κ) map was created for each sample using both the double-sided and single-sided methods described in Sections 2.1 and 3.1, respectively. The true-phase measurements were performed using the optimised parameters established previously. Figure 4.8 shows the single- and double-sided κ maps for six samples to illustrate the typical response from the different types of contaminants used. Appendix D contains the equivalent interface true-phase (Φ_{bond}) maps for these specimens. It can be seen from Figure 4.8 that the interfacial stiffness maps of the ceiling tile and MgO specimens exhibit regions of lower κ towards the bottom edge of the samples (where an evacuation pipe was fitted) compared with the upper end. This is because the interface evacua-

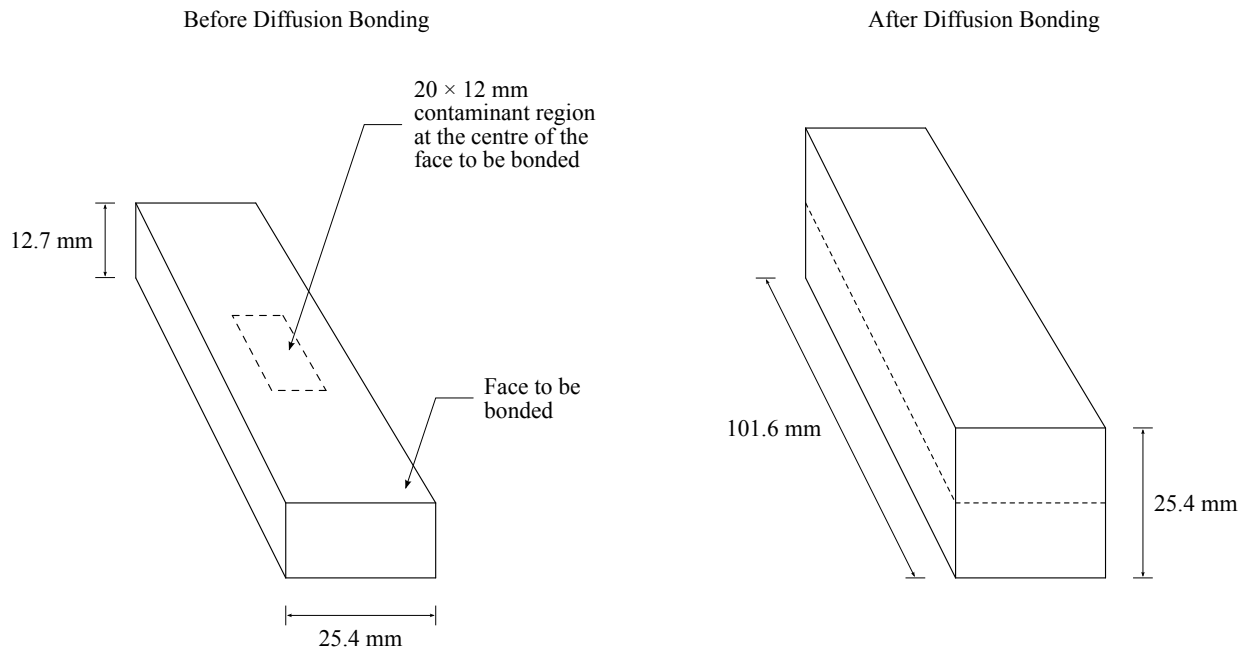

FIGURE 4.7 Specimen geometry for the samples used to here to compare the single-sided approach with the double-sided counterpart

tion process necessary during HIP displaces loose particulates effectively but is less able to affect aqueous stains. Despite attempts to mitigate this effect, retaining the contaminants within the designated area was not as successfully achieved with particulates as it was with staining.

Each κ map (two per sample, each comprising point-by-point estimates of κ) was averaged so that the single-sided and double-sided predictions of interfacial stiffness could be more readily compared. This is shown in Figure 4.9, where excellent agreement between the two methods is evident. The original work by Milne et al. showed that the double-sided inspection could be used to distinguish between well- and poorly-bonded samples [14], and the results in the figure now highlight the equivalence between the single- and double-sided approaches, suggesting that the single-sided method can indeed be used effectively when access to both sides of the diffusion-bonded interface is not possible.

The κ measurement standard deviations are not shown because these were large and would render the graph illegible. The large standard deviations observed are the result of the point-by-point nature of the calculations and the sensitivity of κ to small changes in Φ_{bond} (see Equation (3.5) and Appendix D). This is exacerbated when the interfacial acoustic impedance mis-

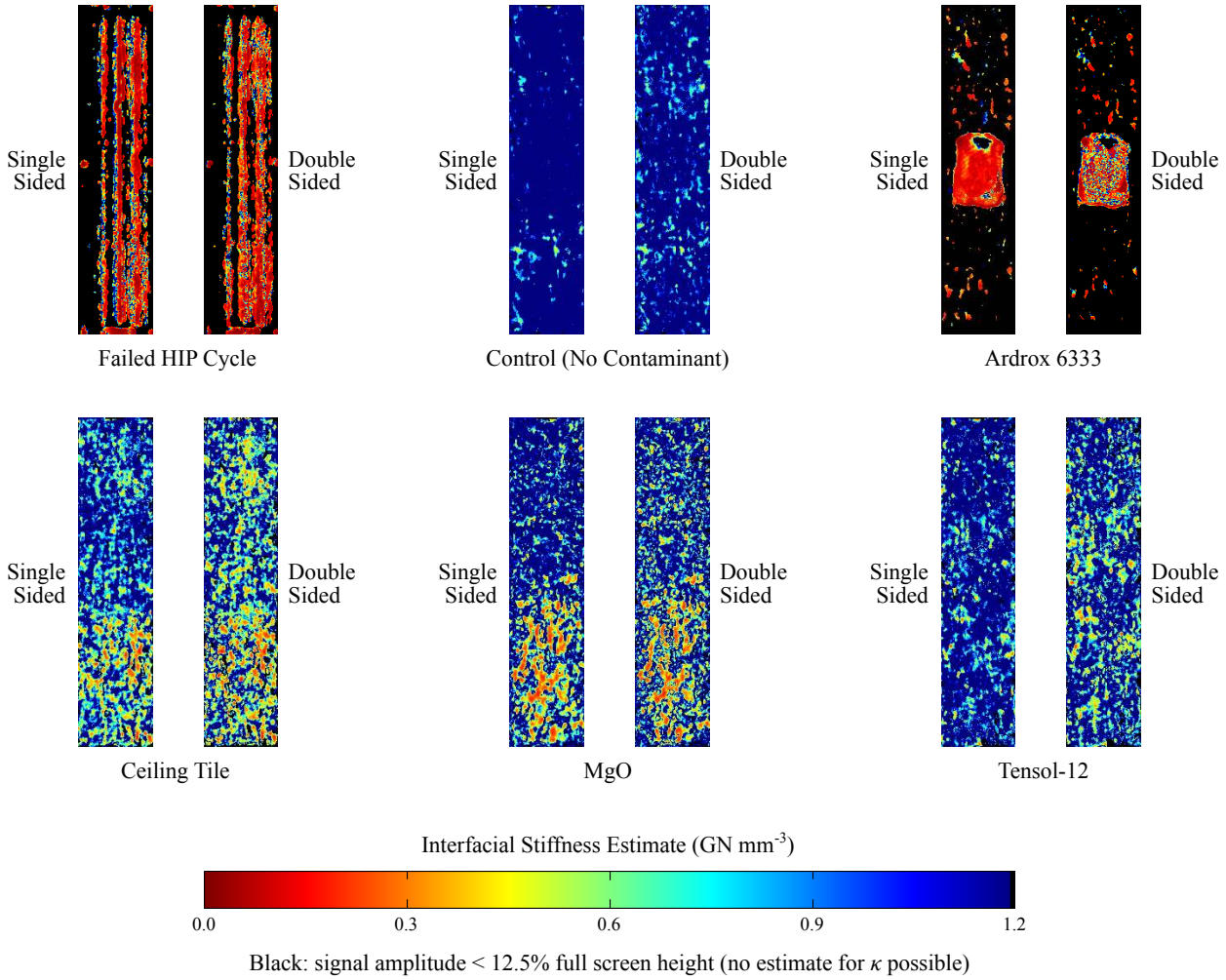

FIGURE 4.8 Interfacial stiffness maps acquired using the single-sided and double-sided techniques. The six specimens shown here are representative examples of the specimens used in these experiments. Note that the calculation to determine κ becomes prohibitively unreliable as the signal amplitude drops below approximately 12.5% (see Figure 4.6). Where this is the case, the map is designated black

matches are small and when well-bonded regions and poorly-bonded regions can exist within the same sample in reasonably equal measure, as is the case for most of the samples here.

The small differences between the average κ values predicted by each method may be explained by the difference in SNRs of the waveforms that each approach uses to determine Φ_{bond}. Single-sided inspections involve the true-phase measurement of one very high-SNR waveform (first inspection: signal from a titanium–water interface used to determine Φ_{ref}) and of one relatively low-SNR waveform (second inspection: diffusion bond signal used to determine Φ). A double-sided inspection, on the other hand, involves the true-phase measurement of *two* relatively low-SNR waveforms (diffusion bond signals from both sides of the interface) the combina-

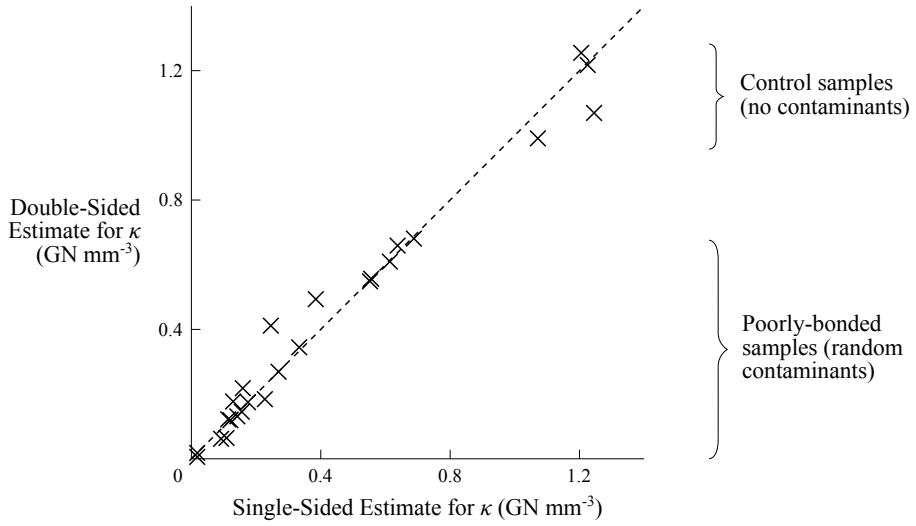

FIGURE 4.9 Comparison of the single-sided and double-sided predictions for the interfacial stiffness κ. The dashed line is the expected relationship. Each cross (×) represents the average κ for one sample using both methods

tion of which introduces greater error into the κ predictions than the single-sided inspections. This 'compounding' of measurement error suggests that the single-sided inspection method is more reliable than the established double-sided approach and offers a possible explanation for the outliers in Figure 4.9. However, although this is true under ideal conditions, the single-sided technique involves two inspections performed at very different times, leading to the risks highlighted in Section 4.3. These must be properly managed if the method is to be fruitfully exploited.

Whilst it has been shown that the two methods are equivalent, the potential benefit of a true-phase-based technique over a conventional ultrasonic inspection has not yet been fully quantified. In an attempt to address this, the 25 diffusion-bonded samples described above were subjected to a conventional ultrasonic inspection with the same transducer that was used for the interfacial stiffness analysis (f_c = 9.25 MHz). This inspection was performed using the same parameters as the κ experiment, except that the gain was fixed at the level required for a 150 µm ø flat-bottom hole at a metal depth equal to that of the diffusion bond to produce a 50% full screen height response. Figure 4.10 shows the normalised amplitude from this inspection plotted against the corresponding single-sided interfacial stiffness estimate for each specimen. Each cross represents an average of the response over the inspected specimen area.

It can be observed that, for samples exhibiting a high average κ (the control samples), the ultrasonic response from the conventional inspection was consistently low. Furthermore, the

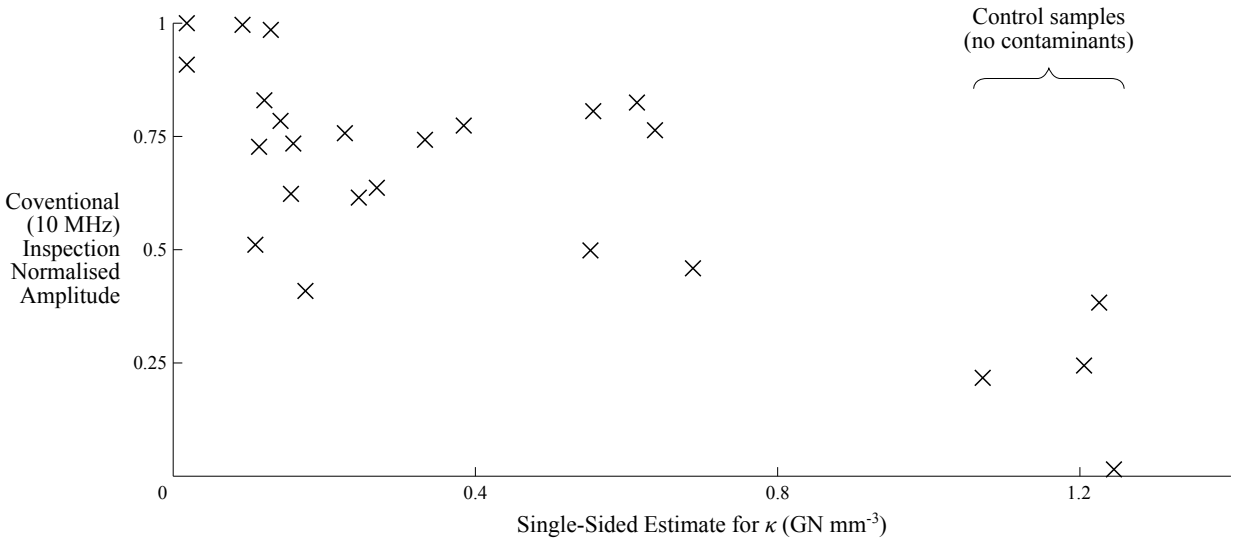

FIGURE 4.10 Single-sided average interfacial stiffness, κ, and corresponding conventional ultrasonic NDE response for 25 contaminated diffusion-bonded samples. Poorly-bonded samples, sections of which are shown in Figure 4.11, exhibited low interfacial stiffness and correspondingly high conventional inspection responses. The opposite is true for the well-bonded control samples

poorly-bonded samples exhibited low interfacial stiffness estimates and correspondingly high amplitude responses from the conventional inspection. These samples exhibited clear evidence of poor bonding after being sectioned, as the representative micrographs in Figure 4.11 show, and so it can be concluded that the interfacial acoustic impedance mismatch of these samples was not large enough to be confused with the response from the contaminants at the interface. In other words, whilst these experiments show that interfacial stiffness estimates are indeed sensitive to the condition of solid-state welds, they do not yield a quantitative measure of the advantage that the technique holds over conventional ultrasonic NDE for forged Ti-6Al-4V diffusion-bonded components. Experiments to yield this quantitative information would produce specimens for which both the interfacial stiffness estimates and the conventional amplitude responses were high.

It is reasonable to assume that κ-based approaches, either single- or double-sided, could become increasingly valuable NDE solutions for adherends that exhibit large acoustic impedance mismatches. Birefringence measurements of forged and cross-rolled Ti-6Al-4V specimens show that typical relative acoustic impedance mismatches, η, between two 'perfectly misaligned' adherends made from these materials is approximately 1.2% and 3.4%, respectively. These relatively low values limit the range over which phase-based interfacial stiffness estimates offer advantages over conventional ultrasonic inspections. Larger acoustic impedance mismatches, such as those

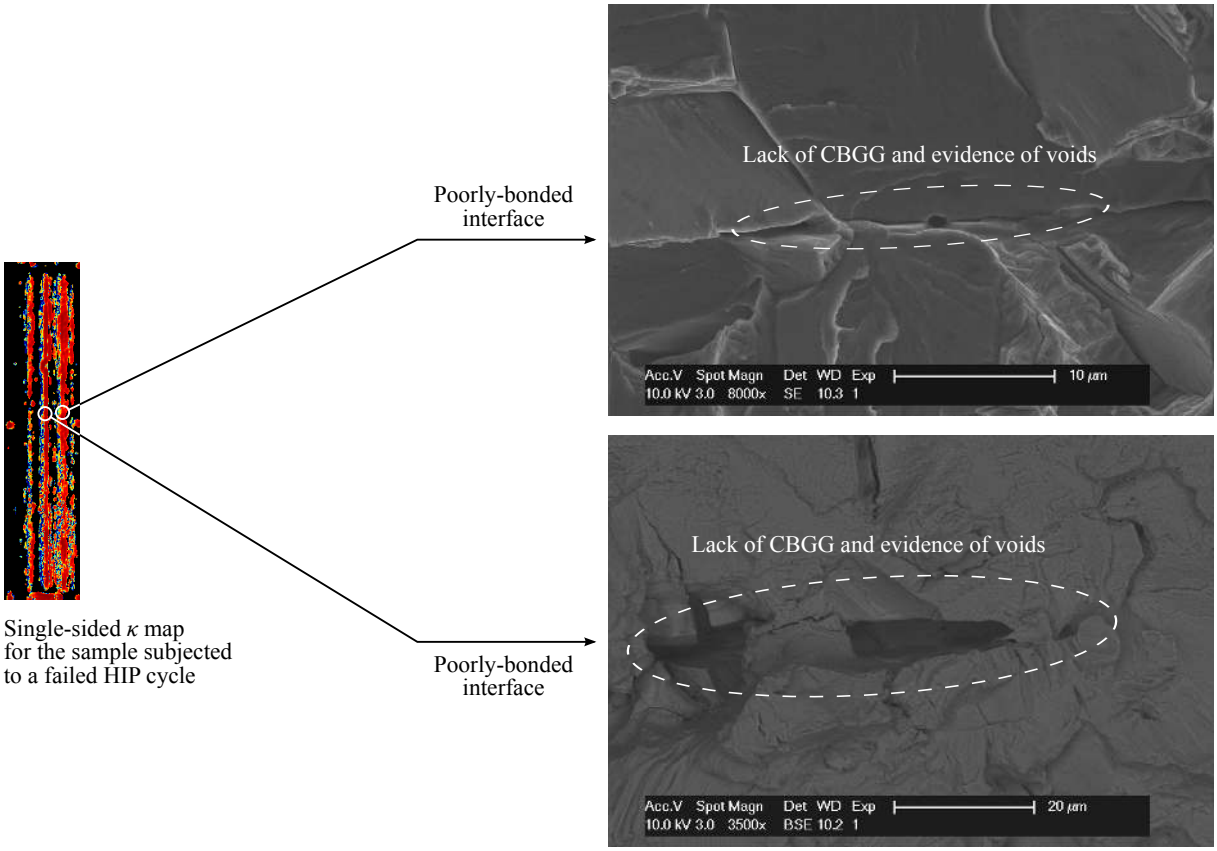

FIGURE 4.11 Representative micrographs of samples exhibiting low average interfacial stiffness. These micrographs were taken from Scanning Electron Microscope (SEM) analyses of the sample that underwent a failed HIP cycle. However, similar evidence of lack of Cross-Boundary Grain Growth (CBGG) and discrete voids was found in all of the other samples for which the κ estimates were low and the conventional ultrasonic responses were high

that would arise from the solid-state welding of dissimilar alloys, would broaden the window of opportunity for the exploitation of the technique described here. Attempts to maximise η in Ti-6Al-4V components by strategically diffusion bonding unidirectionally-rolled plates (the preferred orientations of the opposing macro-zones on both sides of the interface were systematically misaligned) proved fruitless since, even in this unrepresentative and extreme case, the reflections from the interface were unable to shroud individual 200 µm ø glass beads embedded at the diffusion bond.

However, the joining of Ti-6Al-4V to Ti-6Al-2Sn-4Zr-6Mo or Ti-6Al-2Sn-4Zr-2Mo, which has been studied previously in order to better exploit the different strengths of these three common titanium alloys [30, 114, 115], could yield acoustic impedance mismatches of between 8% to 10% based on typical material properties at room temperature [116]. Even greater mismatches are possible when completely dissimilar materials, such as aluminium and magnesium alloys, are joined.

Whilst these types of diffusion bonds have been investigated [117], it is unclear if they are widely exploited commercially. Despite this, it is clear that in these cases, where η can be much greater than the $\approx 1\%$ mismatch observed here, the κ-based approaches would significantly improve ultrasonic NDE capability.

It is not possible, with the results presented here and the η limitations described above, to sensibly and convincingly claim that κ measurements are significantly more reliable indicators of interface integrity than amplitude measurements alone for diffusion-bonded Ti-6Al-4V components. However, the results do show that κ measurements are sensitive to the integrity of the solid-state weld and that, given sufficient η, the analyses and results from this chapter and those of Chapter 3 can be gainfully exploited in other inspection scenarios. In terms of increasing the ultrasonic inspection sensitivity to meet the requirements for Ti-6Al-4V titanium alloys used in safety-critical gas turbine engine components, these results indicate that it is necessary to turn to the field of non-linear acoustics, which is treated in the next chapter.

4.5 Summary

The practical aspects of the proposed single-sided true-phase measurement approach have been described. It has been shown that the diffusion bonding process most commonly used in the aerospace industry does not induce sufficient microstructural changes to adversely affect the technique. The effect of water temperature on phase aberration was also illustrated, highlighting the need for maintaining a constant ambient temperature during inspections, as is the case for many other ultrasonic NDE techniques. In addition, the computational code required to manipulate the inspection files and compute κ was put forward, and potential unique risks to the process were identified with reasonable mitigating actions subsequently advised.

The above practical considerations served as a foundation for an investigation into the equivalence between the prospective approach and its double-sided counterpart. This equivalence was demonstrated experimentally and the potential of the technique was tentatively laid out. Sensitivity to the integrity of diffusion-bonded interfaces was demonstrated on a number of samples con-

taining seeded defects relevant to the industrial exploitation of diffusion-bonded titanium components.

However, it was not possible to quantify the improvement in capability that the technique offers compared to conventional approaches with respect to Ti-6Al-4V components. The acoustic impedance mismatches observed in the forged samples used here and in unidirectionally-rolled samples with relatively large texture mismatches were insufficient to shroud the defects that were embedded at the diffusion-bonded interfaces. Conventional inspections were adequately able to distinguish the poorly-bonded and well-bonded samples without recourse to the phase-based inspection technique.

It was noted that other solid-state welds where there is a large interfacial acoustic impedance mismatch (e.g. between dissimilar materials) could benefit substantially from the phase-based ultrasonic NDE techniques described and optimised here. As for diffusion-bonded Ti-6Al-4V components, the possible interfacial acoustic impedance mismatches appear to be too low and/or the embedded contaminants too large or numerous for the phase-based techniques to offer significant advantages over conventional methods. Non-collinear non-linear ultrasonic NDE, explored in Chapter 5, may offer significantly improved inspection capability that does not depend on the interfacial acoustic impedance mismatch and promises to be an overall much more sensitive indicator of material integrity than conventional ultrasonic NDE approaches.

5. Non-Linear Ultrasonic Approach

Several linear ultrasonic NDE techniques have been reviewed and, in the case of interfacial stiffness measurements, studied thoroughly to address the diffusion-bonded Ti-6Al-4V inspection problem. However, the access requirements of the double-sided approach, the inconvenient range of relative acoustic impedance mismatch values at which both single- and double-sided techniques were expected to work and the difficulty in generating small enough defects to be shrouded by these small texture mismatches but still be perceivable to linear acoustic methods have cumulated to render linear acoustic techniques inadequate for this particular NDE problem. Non-collinear non-linear ultrasonic NDE, the background of which was detailed in Chapter 2, is adapted and evaluated in the work that follows with the purpose of more fully satisfying the requirements expressed in Section 1.2.

5.1 Optimised Wave-Mixing for Interface Inspection

Mixing two ultrasonic pulses, preferably of different frequencies and originating from non-collinear sources, was discussed in Section 2.2. It was shown that the merits of such a technique are the generation of a spectrally, modally and spatially dissociable third wave whose amplitude relates directly to the integrity of the material within the interaction volume. The generation of this distinctly isolable third wave brings about benefits that make non-collinear non-linear ultrasonic NDE an attractive proposition for the inspection problem described here.

It was shown in Section 2.2 that the initial experiment (hereafter referred to as the 'bulk' configuration) must satisfy Equations (2.7a) to (2.7c) as well as the so-called resonance condition—

Equations (2.8a) and (2.8b)—in order for the interaction that generates the third wave to take place and for its output to be related to the integrity of the material. Figure 5.1 shows how the intersection angles described by Equations (2.7a) to (2.7c) vary with the frequency ratio a for a given shear-to-longitudinal velocity ratio c (in the case of Ti-6Al-4V titanium alloy, $c = 0.519$ and the Poisson ratio $\nu = 0.316$). There is limited flexibility in this regime as the intersection angles and other variables have limited ranges within which the experiment will be sensitive to the presence of TOECs.

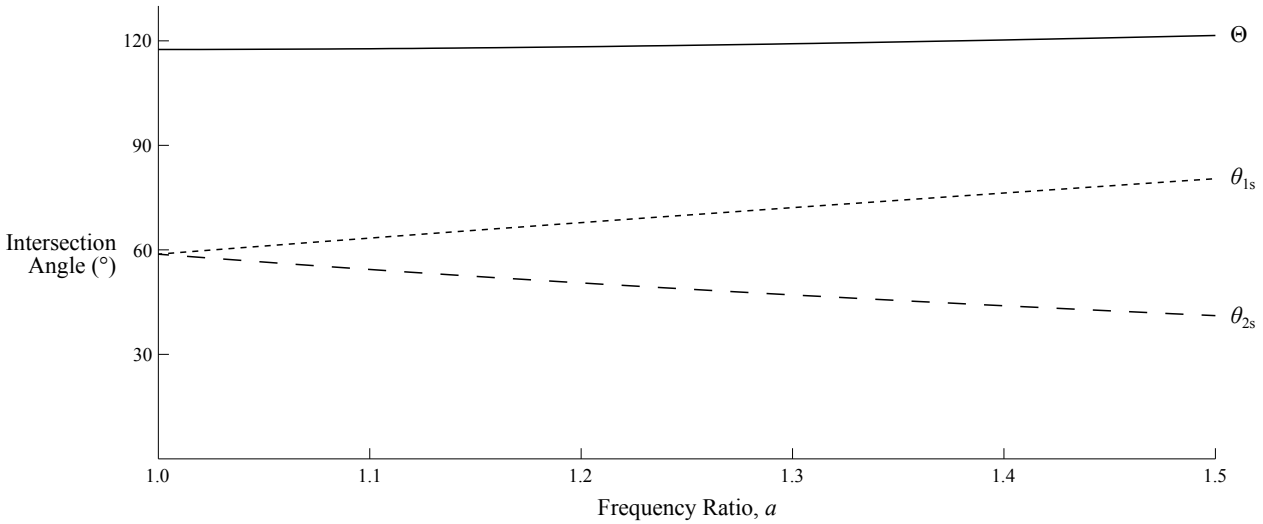

FIGURE 5.1 Variation of the mixing angles Θ, θ_{1s} and θ_{2s} with the frequency ratio in Ti-6Al-4V titanium alloy ($c = 0.519$, $\nu = 0.316$)

However, it was also noted in Section 2.2 that for the inspection of imperfect interfaces, the TOEC contribution is not as relevant as that of CAN, which, if present, is the overwhelming source of non-linearity in a component [97]. Phase matching at the interface maximises sensitivity to CAN, whereas phase matching over the interaction volume maximises sensitivity to TOEC. For the NDE of titanium diffusion bonds, it is clearly better to maximally reject the bulk TOEC contribution whilst simultaneously retaining sensitivity to the interfacial CAN contribution. This implies deliberately spoiling the interaction described by Equations (2.7a) to (2.7c) but continuing to satisfy the temporal part of the resonance condition, described by Equation (2.8a).

This difference in approach yields an alternative experiment (the 'interface' configuration) that is still non-collinear mixing, and in which phase matching is still essential, but in which this phase

matching is forced to occur very specifically over the interface and, if possible, nowhere else. Doing this would mean, given the nature of the CAN mechanism and the planar nature of the diffusion-bonded interface, that:

$$(\mathbf{k}_1 + \mathbf{k}_2) \times \mathbf{n} = 0, \tag{5.1}$$

where $\mathbf{n}$ is the reception direction and, in this special case, the surface normal of the interface. Full constructive interference in the form of phase matching is therefore ensured by:

$$\omega_1 \sin\theta_{1s} = \omega_2 \sin\theta_{2s}. \tag{5.2}$$

These relations imply that there is no explicit optimal Θ for interface inspection experiments unlike in the bulk configuration, and this yields increased flexibility in terms of transducer positioning and angulation. Figure 5.2 shows how the interaction angle θ_{2s} varies with a in this new regime for the same c as in Figure 5.1. θ_{1s} can now be set to a greater range of values ($\theta_{1s} = 54°$ in the figure), with the potential for much smaller interaction angles than before.

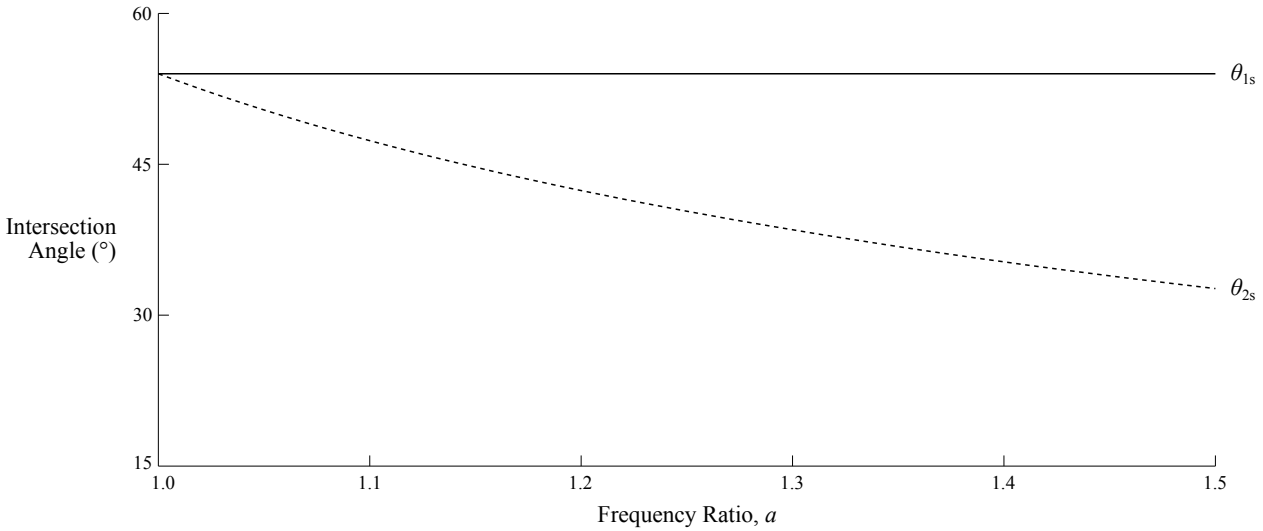

FIGURE 5.2 Interface inspection variation of the mixing angle θ_{2s} with the frequency ratio in Ti-6Al-4V titanium alloy ($\theta_{1s} = 54°$, $c = 0.519$, $\nu = 0.316$)

5.2 Bulk and Interface Experiments

The above modifications and the precedent bulk configuration were examined experimentally. For both sets of experiments, one of the main considerations when determining the mixing angles was the transmission of the shear waves into the specimen as a function of incidence angle. The shear wave transmission coefficient resulting from a longitudinal wave in water (ρ = 998 kg m^{-3}, c_l = 1.48 mm µs^{-1}) incident onto Ti-6Al-4V titanium alloy (ρ = 4420 kg m^{-3}, c_l = 6.15 mm µs^{-1}, c_s = 3.19 mm µs^{-1}) is shown in Figure 5.3.

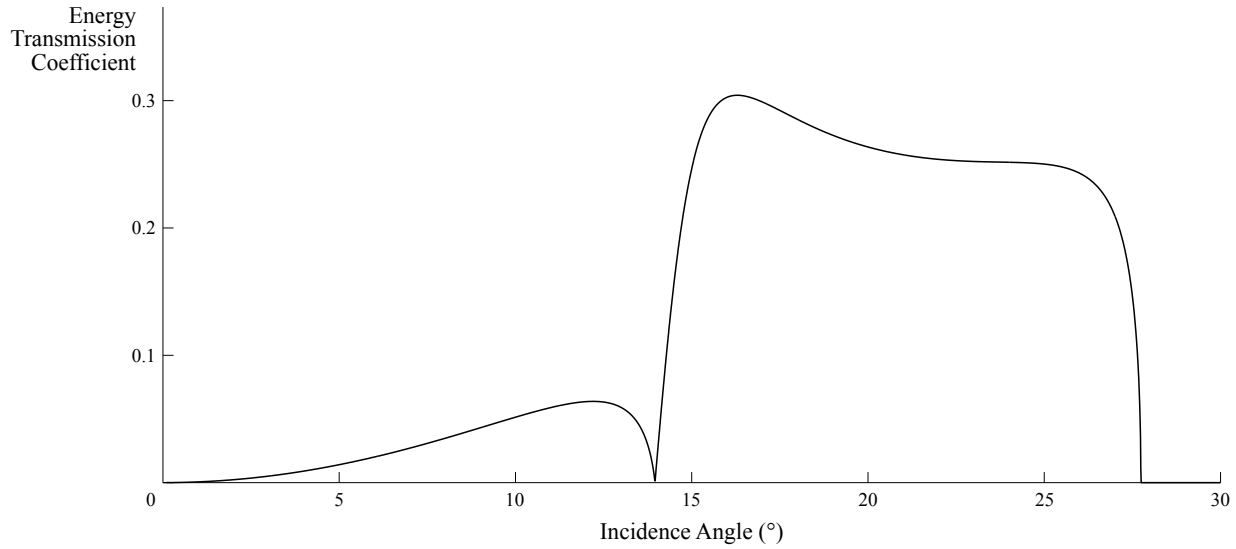

FIGURE 5.3 Shear-wave energy transmission coefficient variation with impinging longitudinal wave incidence angle for Ti-6Al-4V immersed in water

The figure shows that the incidence angles $\theta_{1\mathrm{t}}$ and $\theta_{2\mathrm{t}}$ must be greater than 16° and less than 27° in order for at least 20% of the energy from the transducers to pass through the water–titanium interface in the form of a shear wave. However, $\theta_{1\mathrm{t}}$ and $\theta_{2\mathrm{t}}$ cannot be the same (since a cannot be unity if there is to be frequency separation) and therefore a compromise must be reached between these two angles such that the maximum total energy reaches the interaction volume. It should be noted that it is undesirable to select the incidence angle that yields peak transmission because this occurs extremely close to the first critical angle, at which no shear-wave energy is transmitted.

Another important consideration for both experiments is the frequency ratio a, which must be selected whilst respecting the shear wave transmission coefficient mentioned above, the fact that

a large a implies a large horizontal distance between the impingement points of the two incident waves and the fact that a cannot be too small because spectral separation of the three waves is one of the main benefits of this technique. A frequency ratio of 1.2 was found to be a reasonable compromise between these competing factors for both bulk and interface experiments.

The resulting interface configuration is illustrated in Figure 5.4, where it can be seen that the transducers were arranged in a more compact fashion than the bulk configuration shown in Figure 2.4. A beneficial consequence of this compactness (quantified by the horizontal distance between the impingement points of the two incident waves, S) is the ability to inspect closer to the specimen edges. The values for θ_{1s}, θ_{2s}, θ_{1t} and θ_{2t} used in both experiments are listed in Table 5.1. It can be seen that a significant reduction in both Θ and S was achieved for the interface configuration.

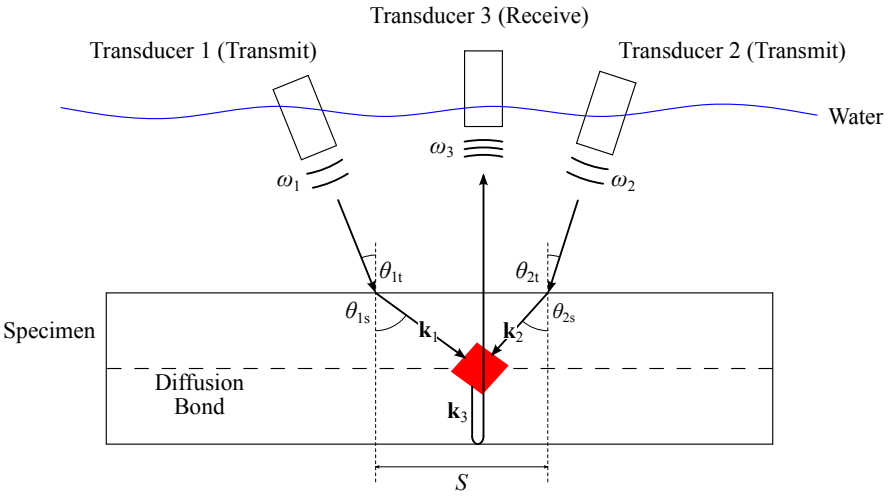

FIGURE 5.4 Wave-mixing experiment for the inspection of diffusion-bonded interfaces. The red parallelogram represents the interaction volume within which the third wave ($\mathbf{k}_3$, ω_3) is generated. Annotated angles are scaled to represent those given for the interface configuration in Table 5.1 (compare with Figure 2.4)

TABLE 5.1 Experiment parameters for bulk and interface configurations (see Figs. 2.4 and 5.4). S depends on the required depth of the interaction volume within the specimen, which was 12.7 mm for both bulk and interface configurations

	Θ (°)	θ_{1t} (°)	θ_{2t} (°)	θ_{1s} (°)	θ_{2s} (°)	S (mm)
Bulk	118.6	25.4	20.9	68.0	50.6	47.0
Interface	96.4	22.0	18.1	54.0	42.4	29.1

Both experiments were performed using the same signal generators, transducers and spectral parameters. Transducers 1 and 2 were unfocused whilst transducer 3 had a focal length in water of 127 mm. Other relevant details are listed in Table 5.2. Transducers 1 and 2 were driven by a signal generator to produce narrowband pulses at fixed centre frequencies in order to obtain the desired frequency ratio $a = 1.2$. These pulses were windowed (Gauss) to control spectral leakage [105]. Transducer 3 (receive mode only when performing non-linear scans) was filtered to maximise the frequency separation effect. The water paths associated with each transducer were no greater than approximately 40 mm.

TABLE 5.2 Transducer parameters and electronics settings for bulk and interface experiments. A bandpass filter was only used on transducer 3 since the other two transducers were driven to produce narrowband pulses of a fixed f_c. Transducers 1 and 2 were unfocused whilst transducer 3 had a focal length in water of 127 mm

Transducer	Nominal ø (mm)	Nominal f_c (MHz)	Pulse f_c (MHz)	Pulse Duration (μs)	Bandpass Width (MHz)
1	6.35	5	4.5	8	-
2	6.35	5	5.5	8	-
3	12.7	10	-	-	0.75

Eight 127 × 127 × 25.4 mm Ti-6Al-4V samples were created for these experiments. Each sample, illustrated in Figure 5.5, was manufactured from two plates diffusion bonded in an evacuated hot press chamber. An additional double-thickness plate was used as a reference sample representing a perfect diffusion bond. This plate was annealed to the same degree as the bonded samples in order to account for any texture changes introduced by the bonding process. The bonding time, temperature, pressure, and the surface roughness of the plates were altered for each sample in order to obtain a range of different bond qualities.

The quality of each diffusion bond was assessed by determining the Cross-Boundary Grain Growth (CBGG), which represents the proportion of grains that were observed to have 'grown' across the interface and were thus fully bonded [7] (see Section 1.1). Micrographs for each sample were taken half way between the centre and the edge of the specimens (see Figure 5.5) at 500x magnification and each was analysed to detect the percentage CBGG per unit area. Table 5.3 shows the observed CBGG for all of the samples. Figure 5.6 shows representative micrographs for samples 1

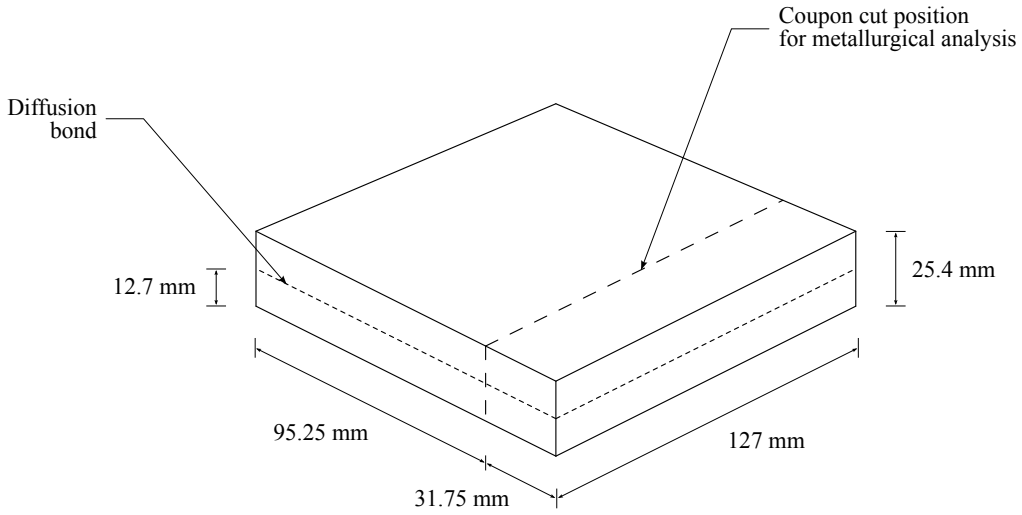

FIGURE 5.5 Specimen geometry for the samples used to here to evaluate the non-collinear non-linear wave-mixing technique. Coupons for metallurgical analyses were extracted from a central position half way between the centre and the edge of each specimen

(6.59% CBGG), 3 (48.0% CBGG) and 7 (85.1% CBGG), selected arbitrarily for illustrative purposes. The micrographs for all eight diffusion-bonded specimens are included in Appendix E.

Note that CBGG is not the inverse of interfacial percentage voiding, but instead represents a more statistically robust, if somewhat conservative, measure of the diffusion bond quality [118, 119]. Unlike interfacial percentage voiding, CBGG is not directly susceptible to the measurement error associated with grains that are in close proximity to each other across the interface but that do not offer the bond any significant strength [120].

TABLE 5.3 Cross-Boundary Grain Growth and pertinent bonding parameters for each sample used in the experiments. 100% CBGG represents a perfect diffusion bond

Sample No.	1	2	3	4	5	6	7	8	9
CBGG (%)	6.59	32.7	48.0	68.8	73.2	79.3	85.1	86.0	100
Temp. (°C)	695	745	745	745	795	845	915	775	800
Time (hrs)	2	2	3	2	2	2	2	4	2

Each specimen was subjected to two separate scans for each configuration. The equipment and specimens were re-aligned and re-calibrated before each repetition in order to give an indication of experiment robustness. Each sample was also scanned using transducer 3 in transmit/receive mode after adjusting its waterpath to focus on the diffusion-bonded interface (rep-

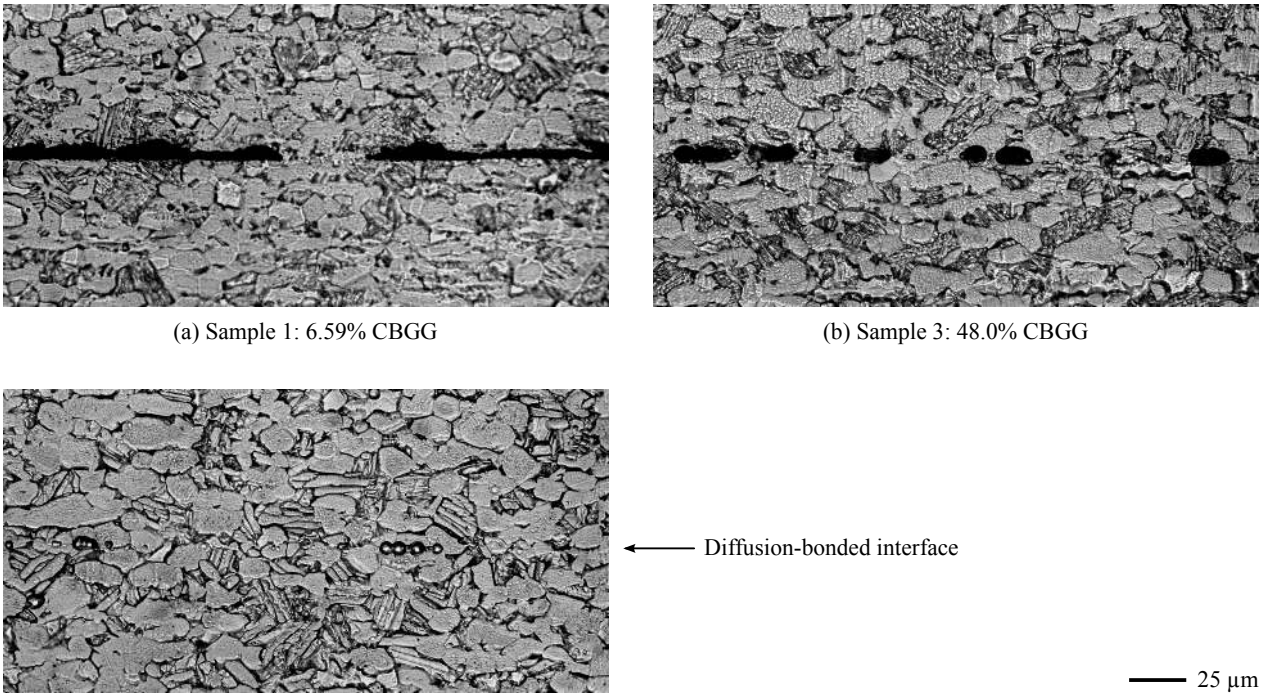

(a) Sample 1: 6.59% CBGG

(b) Sample 3: 48.0% CBGG

(c) Sample 7: 85.1% CBGG

FIGURE 5.6 Micrographs of samples 1 (a), 3 (b) and 7 (c) at 500x magnification, showing progressively greater diffusion bond quality as quantified by the percentage Cross-Boundary Grain Grown (CBGG)

resenting a conventional 10 MHz inspection), illustrating that this approach could yield simultaneous linear/non-linear inspection data if so adapted. Additionally, an industrial scanner was employed to inspect each sample at 25 MHz for completeness.

5.3 Results and Discussion

Non-linear responses were acquired from the central 50.8×50.8 mm region (40×40 scan positions) of each sample. Images were produced by measuring the spectral magnitude (at 10 MHz) of the reflected longitudinal wave from the interface at each scan position. Figure 5.7 shows the non-linear images of the nine samples used in this study. The magnitudes of the non-linear signatures were normalised relative to the highest response in the whole sample set and a colour scale was applied for visualisation.

The figure shows that there is a perceivable increase in overall non-linearity from samples 1 to 5. It is also evident that the most poorly bonded specimen (sample 1) produced a similar non-linear response to that of the reference specimen (sample 9), as expected given that gross disbonds

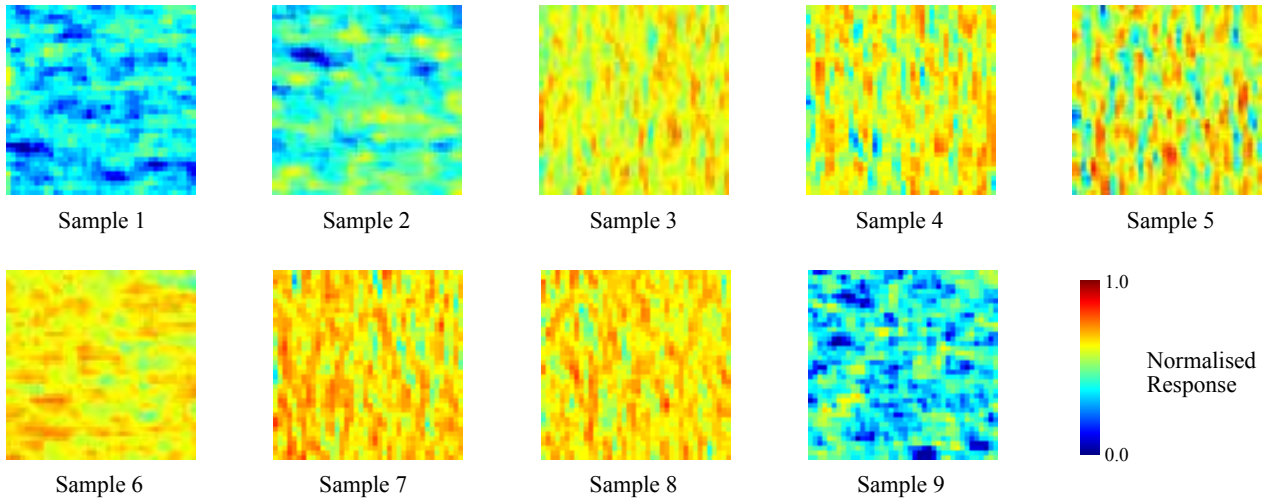

FIGURE 5.7 Non-linear response, normalised to the highest value observed overall, for each sample using the interface configuration. Each image depicts the central 50.8 × 50.8 mm area of the sample (40 × 40 scan positions)

are known to exhibit limited non-linearity [121]. It is convenient to visualise these results by plotting the average response from each image against CBGG, as shown in Figure 5.8. Here, a comparison is made between the two sets of experiments performed using the interface configuration. The error bars represent one standard deviation in non-linear response over the inspected area of each specimen.

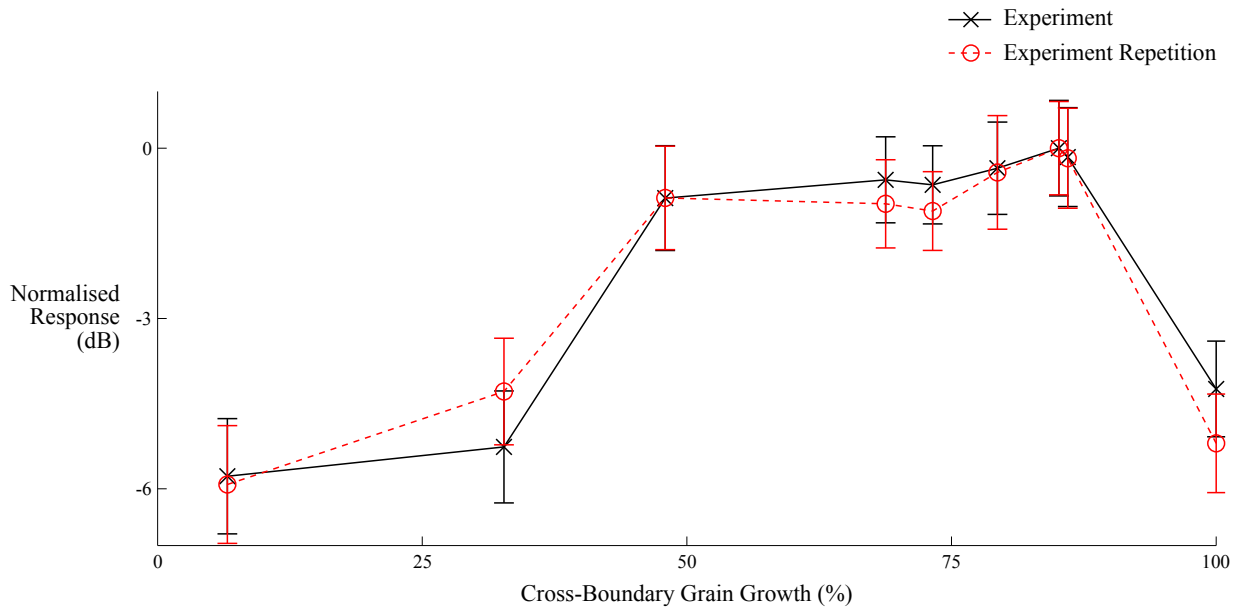

FIGURE 5.8 Comparison between two repetitions of the interface configuration experiment. Each point marks the mean response from the corresponding specimen, with the error bars representing one standard deviation in response over the averaged area. Lines between points are for clarity only and do not represent expected behaviour

A relatively low non-linear response was observed for samples 1, 2 and 9 in both sets of experiments, whilst the remaining samples exhibited reliably higher non-linear responses across the two sets of experiments. A similar maximum for the non-linear response of poorly-bonded interfaces as a function of contact pressure was predicted first by Richardson [81] and observed experimentally by Solodov [122]. In addition, the standard deviations calculated for each sample were consistent in both tests. These results show that the experiments were robust despite the complete re-alignment of the apparatus between experiment sets, as corroborated by earlier work where it was observed that wave-mixing measurement standard deviations can be as low as 1.33% [123]. This level of robustness and repeatability represents a significant improvement over other non-linear imaging techniques.

A comparison was also made between the bulk and interface configuration responses. These two configurations differ in that they exhibit different levels of sensitivity to bulk material (TOEC) and interface (CAN) non-linear contributions (see Figures 2.4 and 5.4 for illustrations of the geometric arrangement that each entails, respectively). The comparison is shown in Figure 5.9. It is clear that the relative decrease in non-linear response of samples 1, 2 and 9 observed using the interface configuration was not as pronounced using the bulk arrangement. The largest drop in non-linear response for the bulk configuration was 3.52 dB, whereas it was 5.93 dB for the interface arrangement. The interface configuration was clearly more sensitive to the condition of the diffusion bond than the bulk arrangement. It is noteworthy that although the interface configuration necessarily suppresses the TOEC portion of the overall non-linear response, this is not detrimental to the detectability of the longitudinal wave because CAN contributions from 'loose' interfaces can be 2 or 3 orders of magnitude greater than those of the TOECs [124].

Having established the reliability of the wave-mixing approach and the merit in optimising the system for the interfacial non-linear response, the conventional 10 MHz inspection and non-linear response results were combined in Figure 5.10 to illustrate the overall effectiveness of the approach. The figure clearly shows that the wave-mixing technique is significantly more sensitive to microstructural imperfections than conventional linear ultrasonic techniques. The linear ultrasonic responses are indistinguishable from one another for bond qualities greater than approximately 70% CBGG (samples 5 and above), whereas the non-linear responses of the same speci-

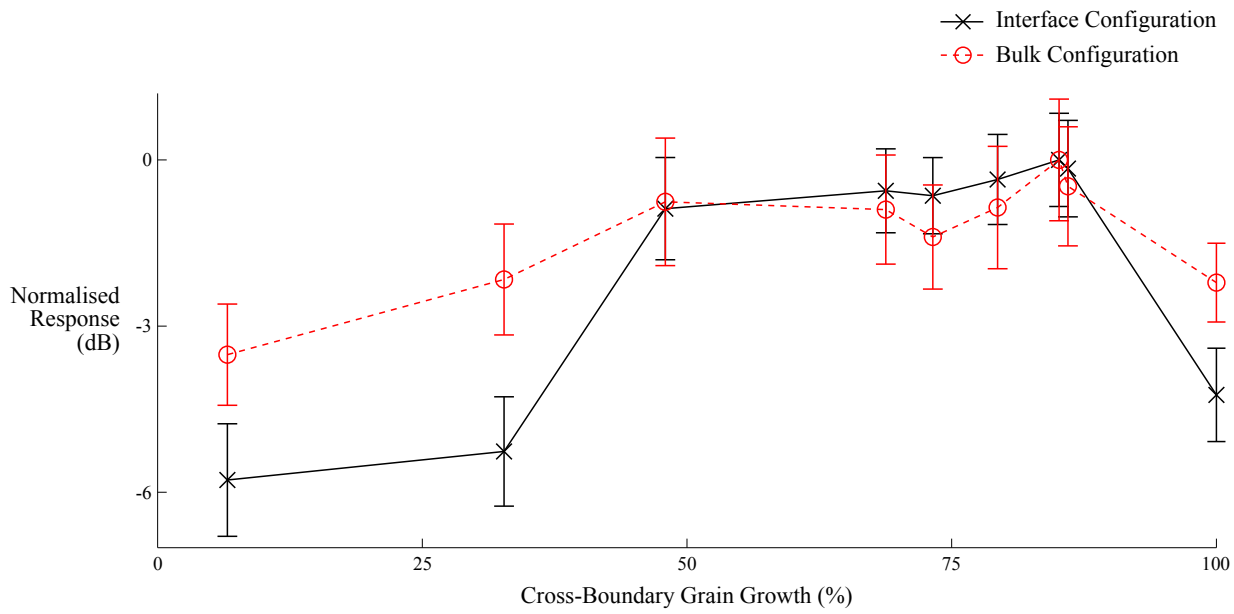

FIGURE 5.9 Comparison between the interface and bulk configuration non-linear responses. Each point marks the mean response from the corresponding specimen, with the error bars representing one standard deviation in response over the averaged area. Lines between points are for clarity only and do not represent expected behaviour

mens are much greater than that of the reference specimen (sample 9; 100% CBGG), allowing a distinction to be made across a much greater range of bond qualities than previously possible.

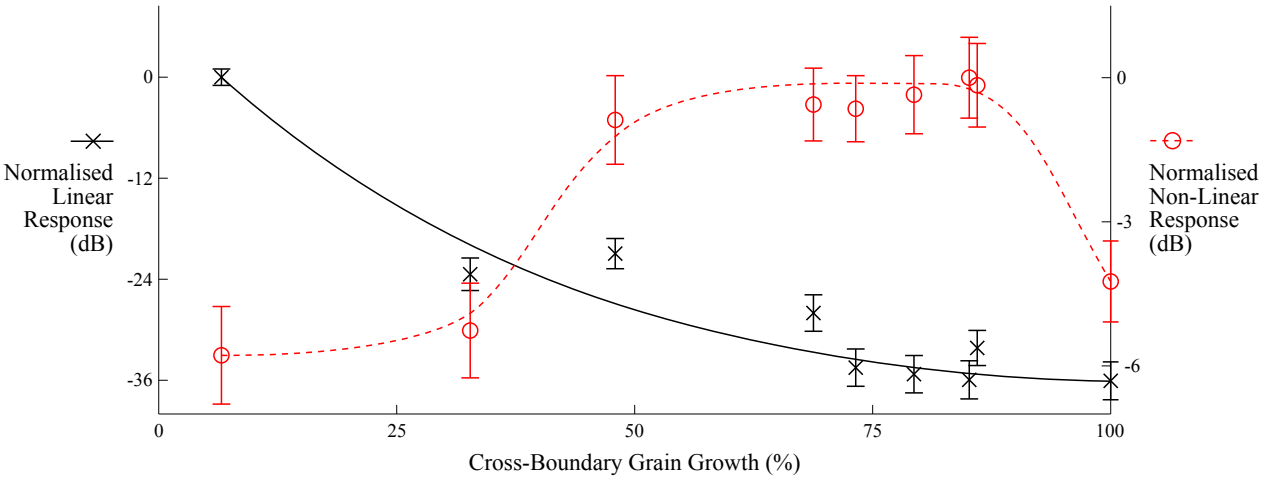

FIGURE 5.10 Linear (left axis, black solid line) and non-linear (right axis, red dashed line) response variation with bond quality. The linear inspection was performed using transducer 3, which had a nominal centre frequency of 10 MHz. Error bars represent one standard deviation in response over the averaged area. Curves are approximate trends and illustrate expected behaviour

It is stressed that the non-linear results cannot be used in isolation: linear and non-linear responses must be exploited together to convincingly extend the range of diffusion bond qualities

determinable non-destructively. With the current arrangement (where Transducer 3 can be reconfigured to transmit/receive in order to acquire a 10 MHz linear ultrasonic inspection covering an equivalent area of the sample), the linear ultrasonic response can be used as a 'high-pass filter' for bond quality: if the linear response is above a given threshold, say −30 dB for the data in Figure 5.10, the samples are clearly very poorly-bonded and there is no need to proceed with the non-linear inspection. However, in the case of a linear response below −30 dB, the magnitude of the non-linear response yields hitherto unknown information as to the state of the material and permits the unambiguous identification of near-perfect diffusion-bonded interfaces.

The significance of these results is further emphasised by the high-frequency ultrasonic inspection results shown in Figure 5.11. Although such an inspection would be unattractive in an industrial setting given the requisite waterpaths and material penetration limitations, it is nevertheless important to highlight that high-frequency linear ultrasonics would not offer any advantage over this novel wave-mixing approach. The figure shows that, for bonds that exhibited more than approximately 70% CBGG, linear ultrasonic inspections were not suitable for determining bond quality. The relative improvement in detectability expected from the higher frequency inspection was limited to samples 1 to 4 (< 70% CBGG); everywhere else the mean 25 MHz response was coterminous with the corresponding 10 MHz result and lay within one standard deviation of the result from the reference sample, thus making separation impossible.

The exception to this was the response from sample 8, which exhibited higher-than-expected responses under both 10 MHz and 25 MHz inspection conditions. This apparently anomalous behaviour is explained by the fact that this sample, along with sample 3 (both highlighted in Figure 5.11) were held at their respective bond temperatures for significantly longer periods of time than the remaining samples (see Table 5.3, which shows that the bond times for samples 3 and 8 were 50% and 100% longer than those of the other samples, respectively). Given that annealing dwell time is inexorably linked to grain size and that larger grains produce greater ultrasonic backscatter, it is not surprising that both of these samples exhibited higher ultrasonic responses than the rest of the sample set.

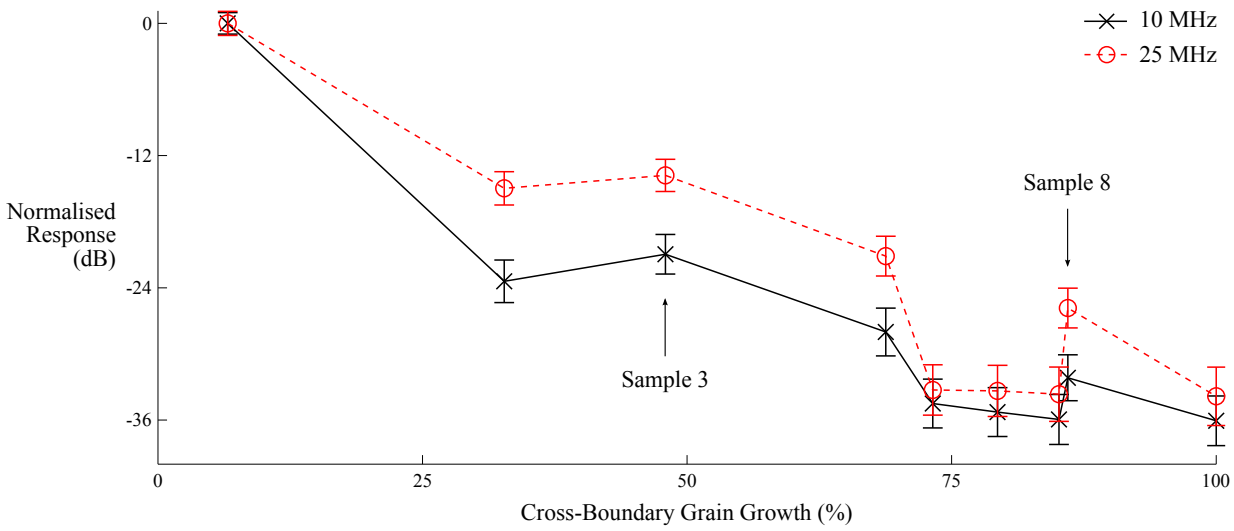

FIGURE 5.11 Mean linear (conventional) ultrasonic response for each sample at 10 MHz (black solid line) and 25 MHz (red dashed line). Error bars represent one standard deviation in response over the averaged area. Lines are for clarity only and do not represent expected behaviour

Note that the linear ultrasonic responses for samples 5 and above were purely the result of back-scattered grain noise: despite spatial averaging and specimen profiling, no unambiguous defect signals were found in these samples at either 10 MHz or 25 MHz. This may be explained by the potentially minute nature of imperfections at the diffusion-bonded interface and the fact that their aggregate response diminishes rapidly as they become sparser and the overall bond integrity improves. Assuming voids of the order of 1 µm ø resulting from initial surface roughness, a pulse with centre frequency of the order of 1 GHz would be required for the interrogating signal wavelength to be comparable to the defect diameter. These findings also make it clear that interfacial stiffness estimates would have been equally incapable of discriminating between these samples.

It is believed that the main contribution to error in these experiments is the remnant sensitivity to bulk non-linearity, the rejection of which can be further improved by reducing the size of the interaction volume and/or employing different wave-mixing configurations. Reducing the interaction volume improves the spatial resolution of the inspection and is a conceptually simple way of reducing the bulk non-linearity with respect to that of the interface because, whilst the bulk non-linear response is proportional to the extent of the *volume*, the interface non-linearity scales with the interfacial *area* within the volume.

Achieving this effect is not trivial because proper interaction between the two oblique waves is paramount to the experiment, and reducing the volume requires *all* transducers to be focused (rather than just transducer 3, as was the case here) and a reduction of the pulse duration, such that correctly timing and aligning the wave packets becomes increasingly difficult. A solution to this may be to use bespoke ultrasonic arrays to both generate and detect the necessary waves. The arrays would have some generic geometric setting angles θ_{1t} and θ_{2t} to minimise the need for extreme electronic beam steering (since large steering angles can be 'lossy' [125]) and they can be designed to electronically 'sweep' to finely optimise temporal and spatial alignment. An additional benefit of this approach would be that a smaller distance S could be achieved (see Figure 5.4), resulting in greater inspection coverage and further rejection of bulk non-linearity.

Perhaps more elegantly, an altogether different wave-mixing interaction could be exploited. It is possible, for example, to mix a longitudinal and a shear wave to generate a longitudinal wave [96]. Though these kinds of interactions may be impractical for bulk characterisation inspections, the nature of diffusion-bonded interface non-linearities may mean that it is possible to achieve even greater bulk non-linearity suppression than with the configurations explored here. The applicability of the original set of possible interactions described by Taylor [90] and others [92] should be reconsidered in light of the diffusion bond inspection problem.

The results from these experiments have demonstrated that the inspection problem described in Section 1.2 can indeed be solved by non-linear ultrasonic NDE. Specifically, this entails the non-collinear mixing of ultrasonic pulses such that Contact Acoustic Non-linearities are excited and thus generate a spatially, modally and spectrally dissociable third pulse whose amplitude is related to the weld integrity. The technique can be applied in a single-sided fashion, it does not require inspections before and after bonding and it does not appear to be significantly affected by the acoustic impedance mismatches present at the interface between Ti-6Al-4V adherends.

5.4 Summary

NDE of titanium diffusion bonds using a non-collinear ultrasonic wave-mixing technique has been investigated. A set of samples with diffusion bonds of varying quality was produced, and

conventional ultrasonic inspections of these were shown to be inadequate for their characterisation, even at relatively high ultrasonic frequencies. Two experiment designs were employed: an 'overall' material non-linearity arrangement and a configuration designed to somewhat reject the non-linearity arising from the bulk material whilst retaining sensitivity to the condition of the diffusion-bonded interface.

A significant improvement in interface inspection capability was observed using the latter approach, though both wave-mixing arrangements offered clear and significant advantages compared with both conventional ultrasonic inspections and, importantly, alternative non-linear techniques.

Overall, the experiments showed that near perfect diffusion bonds could be successfully separated from the partial bonds to which linear ultrasonic approaches exhibited no sensitivity. Moreover, the robustness, flexibility and insensitivity to external non-linearity of non-collinear mixing were sufficiently illustrated. The main contribution to this improved capability and the observed repeatability of the mixing experiments was the spectral, modal and spatial separation of system and interfacial non-linearity offered by the non-collinear technique.

6. Conclusions and Overview

Linear and non-linear techniques for the ultrasonic NDE of diffusion-bonded Ti-6Al-4V components have been investigated. An overview of the work laid out in this document is presented below, followed by a summary of the associated findings.

The relevance of Ti-6Al-4V titanium alloys was described in Section 1.1 in the context of novel and important safety-critical gas turbine engine components. These components include Titanium Metal Matrix Composite (TiMMC) compressor discs that can weigh up to 60% less than monolithic counterparts [11, 12], super-plastically formed fan blades that can only be produced practicably with hollow cores using diffusion bonding [13], and open-rotor engine hubs, the size of which make manufacturing difficult unless diffusion bonding is employed.

The motivation for this work was then presented in Section 1.2, where the importance of improving current ultrasonic NDE capability was stressed given the safety-critical nature of the environment in which titanium diffusion bonds would be best exploited and where the challenges to be overcome were also laid out. The primary challenges were identified as being the macroscopic anisotropy of the titanium alloys of concern here, the morphology of the defects that diffusion bonds may be susceptible to and the complex geometries that must be satisfactorily inspected.

Chapter 2 contained separate overviews of both linear and non-linear acoustics with the aim of highlighting the benefits and disadvantages of each, particularly with regard to sensitivity and ease of implementation. Several linear and non-linear methods were reviewed and assessed and it was shown that there was no self-contained solution capable of overcoming the challenges mentioned above. A strategy for developing the most promising approach in each strand was then detailed:

the encouraging results produced by Milne et al. [14] were to be pursued in order to understand the sensitivity limit of linear ultrasonic NDE, whilst the non-collinear wave-mixing technique was to be investigated to understand whether attempting to overcome the difficulty in producing robust raster-scanned non-linear measurements could be justified by the potential for significantly improved sensitivity to the integrity of solid-state welds in titanium components.

The selected linear ultrasonic NDE approach was developed in Chapter 3. Its main limitation (its need for access to both sides of the inspected interface) was addressed and the computational algorithms on which it depends were optimised. The optimisation process resulted in findings, listed in Section 6.1, that can be applied to other situations in which accurate phase measurements are required. Experimental validation of the new approach was then presented in Chapter 4. Potential limitations and complicating factors were addressed and an operational procedure was laid out in detail before the technique was compared to its double-sided counterpart and a conventional linear method using representative samples.

The non-linear approach was explored in Chapter 5, where it was adapted for the inspection of the geometries of interest here and where the process to maximise its sensitivity to the non-linearity originating from the interface was demonstrated. The samples and experiments that formed evaluation trials of the technique were described and the results presented and compared with those from conventional linear ultrasonic tests. The conclusions drawn from this evaluation are also listed below.

6.1 Summary of Findings

Linear ultrasonic techniques exploiting resonance, spectral analysis and signal processing were shown to be inadequate for the inspection problem defined in Section 1.2. A more promising technique, utilised successfully by Milne et al. on representative Ti-6Al-4V samples [9], was based on the phase-spectrum analysis of signals reflected from a diffusion-bonded interface to determine their true phase and thus differentiate well-bonded and poorly-bonded samples. However, the approach produced complicated inspection results in the form of complex reflection coeffi-

cient pairs and, crucially, required access to both sides of a diffusion-bonded interface. Work to build upon this technique produced:

1. the definition of a single-sided adaptation to the phase-based approach involving inspections performed both before and after bonding to account for and reduce the impact of the texture effects inherent in Ti-6Al-4V titanium alloys,
2. an expression for the interfacial stiffness that is a function of the measured interface phase contribution and which is a more intuitive inspection output than complex reflection coefficient pairs and
3. a set of optimised signal processing parameters that result in improvements to the phase measurement accuracy of up to one order of magnitude and which can be applied in other situations where accurate phase measurements are required.

The above analyses, along with the results of the experimental validation of the new approach, showed that:

4. the extraction window length should be equal to the period of the signal of interest,
5. broadband transducers having normalised bandwidths of approximately 80% or more should be used,
6. observing points 4 and 5 makes the measurement relatively insensitive to the phase spectrum region of interest used to determine the true phase, as long as this does not exceed the transducer bandwidth,
7. the transducer centre frequency should be selected on the basis of the inspection requirements and not on the potential for extrapolation error resulting from the true-phase measurement algorithm (noting of course the need to respect the quasi-static modelling approximation $\omega \ll \sqrt{4\kappa/m}$),
8. rectangular extraction windows should always be used when performing phase measurements and
9. respecting points 4 to 8 enables the reliable acquisition of true-phase data in 'noisy' environments like diffusion-bonded Ti-6Al-4V components.

It was additionally shown that:

10. the diffusion bonding process most commonly used in the aerospace industry does not induce sufficient microstructural changes to adversely affect the technique,
11. the temperature of the environment in which the technique is performed must be adequately controlled during inspections, as is the case for most ultrasonic NDE, and
12. the process is potentially susceptible to unique risks, such as the loss of the reference inspection data between the first and second inspections, and these require reasonable mitigating actions if the technique is to be properly exploited.

The above practical considerations served as a foundation for an investigation into the equivalence between the prospective approach and its double-sided counterpart:

13. equivalence in capability between the single-sided technique and its predecessor was demonstrated experimentally,
14. sensitivity to the integrity of diffusion-bonded interfaces was demonstrated on a number of samples containing seeded defects relevant to the industrial exploitation of diffusion-bonded titanium components, and
15. the potential of the technique was detailed, particularly with respect to solid-state welds exhibiting large acoustic impedance mismatches ($\eta > 8\%$). However,
16. it was not possible to quantify the improvement in capability that the technique offers compared to conventional approaches with respect to Ti-6Al-4V components because the acoustic impedance mismatches observed in the samples used ($\eta \approx 1\%$) were insufficient to shroud the defects that were embedded at the diffusion-bonded interfaces.

It was then noted that non-linear ultrasonic NDE may offer significantly improved inspection capability that:

17. does not depend on the interfacial acoustic impedance mismatch and
18. promises to be an overall much more sensitive indicator of material integrity than both conventional and phase-based ultrasonic NDE approaches.

Non-linear ultrasonic techniques that rely on acousto-elasticity and collinear harmonic generation were reviewed, but

19. the non-collinear wave-mixing technique was identified as the most compelling approach as a result of its ability to image material non-linearity whilst largely eliminating unwanted non-linear contributions from external sources.

A set of samples with diffusion bonds of varying quality was produced and two experiment designs were employed: an overall material non-linearity arrangement ("bulk configuration") and a configuration designed to somewhat reject the non-linearity arising from the bulk material whilst retaining sensitivity to the condition of the diffusion-bonded interface ("interface configuration"). Experiments showed that:

20. conventional ultrasonic inspections of the specimens were unable to characterise the integrity of the diffusion bonds, even at relatively high ultrasonic frequencies,
21. supplementing conventional inspections with wave mixing (either bulk or interface configurations) offered clear and significant advantages compared with conventional inspections alone and also, importantly, alternative non-linear techniques and
22. an appreciable improvement in interface inspection capability could be attained using the interface configuration compared with the bulk configuration.

Moreover, the experiments showed:

23. the robustness, flexibility and insensitivity to external non-linearity of non-collinear mixing,
24. the importance of the spectral, modal and spatial separation of system and interfacial non-linearity offered by the non-collinear technique and
25. that a near perfect diffusion bond could be successfully and reproducibly separated from the partial bonds to which linear ultrasonic approaches exhibited no sensitivity.

The significance of points 20–22 and 25 is emphasized: an inspection technique that utilises only conventional, readily-available and relatively inexpensive ultrasonic NDE equipment has been successfully applied to the inspection problem defined in Section 1.2. The integrity of the diffusion bonds in Ti-6Al-4V aerospace components has been established experimentally using this

advanced approach despite all other techniques, including ultrasonic NDE employing high transducer centre frequencies, proving inadequate. The technique needs access to only one side, and whilst it does still rely on conventional ultrasonic NDE to identify very-poorly bonded specimens, it offers hitherto unobserved levels of sensitivity to interface integrity compared to conventional ultrasonic approaches.

6.2 Future Work

The exploitation and future development of the linear (κ-based) approach is dependent on the extent to which the solid-state welding of dissimilar materials is adopted in industry. If dissimilar materials are indeed joined then conventional amplitude-based techniques would not be satisfactory (as a result of the factors described in Section 1.2) and the κ-based method becomes very attractive. In its current state and according to the NASA-derived Technology Readiness Level (TRL) scale [126], the single-sided technique presented here is at TRL 4, and as such it is ready to be built into a representative production system in order for its capability to be comprehensively evaluated. Once components that have solid-state welds exhibiting relatively large (> 8%) acoustic impedance mismatches have been identified, the necessary steps entail:

- incorporating the computational code produced for this project into a production inspection system,
- creating a suite of test pieces from these components containing pertinent interfacial defects,
- systematically evaluating these specimens using the technique, noting any key process variables,
- undertaking a Probability of Detection (PoD) study to quantify the inspection capability and
- evaluating the technique with respect to the inspection requirements and in light of alternatives that may be available

The above steps could also be applied to adhesively bonded components rather than those that are solid-state welded, but attention must be given to the adhesive layer thickness in this case, as the

Baik & Thompson imperfect interface model applies only when the wavelength is much greater than the layer thickness [60].

The non-collinear non-linear technique is less mature than the linear method described above. It is currently at TRL 2 and requires further work to optimise the Third-Order Elastic Constant (TOEC) contribution rejection whilst retaining sensitivity to the Contact Acoustic Non-linearity (CAN) contribution. This could be achieved by:

- exploring alternative wave-mixing interactions that, although already reported in the literature [90, 92], have been somewhat disregarded as a result of their impracticability for the characterisation of bulk material non-linearity and/or
- minimising the size of the interaction volume, which would exploit the fact that the bulk non-linear response is proportional to the extent of the *volume* whilst the interface non-linearity scales with the interfacial *area* within the volume. This would also improve the spatial resolution of the inspection.

The two points above should be supplemented by the use of ultrasonic arrays, which would significantly improve the temporal and spatial alignment of the acoustic pulses insonifying the interaction volume and would also increase the inspection coverage by reducing the footprint of the three transducers.

Finally, future work should aim to establish a relationship between the ultrasonic signatures acquired non-destructively and engineering strength parameters. In the work presented in Chapter 5, it was evident that a linear approach could not be used to reliably inspect diffusion bonds with more than 70% Cross-Boundary Grain Growth (CBGG), whereas the proposed hybrid non-linear approach permitted the identification of near perfect diffusion bonds. It would be beneficial to relate this 70% CBGG value, for example, to some measure of the interface strength. However, such a comparison between a single measure of bond quality, like CBGG, and interface strength is fraught with difficulty because of the large sensitivity variation among different strength-related parameters of interest, such as the yield strength, ultimate tensile strength, fatigue strength, fracture toughness, etc. [2].

References

[1] Megson, T. (2007) *Aircraft Structures for Engineering Students*, 4th edn. Oxford, Elsevier.

[2] Ohsumi, M., Kiyotou, S., and Sakamoto, M. (1985) The Application of Diffusion Welding to Aircraft Titanium Alloys. *Transactions of the Iron and Steel Institute of Japan*, **25**, 513–520.

[3] Cumpsty, N. (2008) *Jet Propulsion: A Simple Guide to the Aerodynamic and Thermodynamic Design and Performance of Jet Engines*, 2nd edn. Cambridge, Cambridge University Press.

[4] Mahoney, M. W. and Bampton, C. C. (1993) Fundamentals of Diffusion Bonding. In: *ASM Handbook Volume 6: Welding, Brazing and Soldering*. ASM International.

[5] Ashworth, M. A., Jacobs, M. H., and Davies, S. (2000) Basic Mechanisms and Interface Reactions in HIP Diffusion Bonding. *Materials & Design*, **21**, 351–358.

[6] Anderson, J. C., Leaver, K. D., Leevers, P., and Rawlings, R. D. (2003) *Materials Science for Engineers*, 5th edn. Cheltenham, Nelson Thornes.

[7] Yan, P. and Wallach, E. R. (1993) Diffusion-Bonding of TiAl. *Intermetallics*, **1**, 83–97.

[8] Suresh, S. (ed.) (1993) *Fundamentals of Metal-Matrix Composites*. Butterworth-Heinemann.

[9] Milne, K. (2010) *Ultrasonic Inspection of Titanium Diffusion Bonds*. Doctoral Thesis, Imperial College London.

[10] Ashby, M. (2005) *Designing Hybrid Materials. In:* Materials Selection in Mechanical Design, 3rd edn. Oxford, Elsevier.

[11] Doorbar, P., Dixon, M., and Chatterjee, A. (2009) Aero-Engine Titanium: from Alloys to Composites. *Material Science Forum*, **618**, 127–134.

[12] Twigg, E. S. (2007) *Method of Manufacturing a Fibre Reinforced Metal Matrix Composite Article*. Patent EP1533067 B1.

[13] Serra, D. (2008) Superplastic Forming Applications on Aero Engines: A Review of ITP Manufacturing Processes. *6th EUROSPF Conference*, Carcassonne, France.

[14] Milne, K., Cawley, P., Nagy, P. B., Wright, D. C., and Dunhill, A. (2011) Ultrasonic Non-Destructive Evaluation of Titanium Diffusion Bonds. *Journal of Nondestructive Evaluation*, **30**, 225–236.

[15] British Standards Institution (2013) BS EN ISO 3452-1:2013. *Non-Destructive Testing: Penetrant Testing—General Principles*. London, BSI.

[16] British Standards Institution (2011) BS EN ISO 15549:2010. *Non-Destructive Testing: Eddy Current Testing—General Principles*. London, BSI.

[17] Hellier, C. J. (2012) *Handbook of Nondestructive Evaluation*, 2nd edn. McGraw-Hill.

[18] Pavlov, S. V., Isaev, A. A., and Zav'yalova, N. (1991) Ultrasonic Inspection in the Production of Disk Blanks Made of Granulated Nickel Alloys. *Metal Science and Heat Treatment*, **33**, 934–936.

[19] Blodgett, M. P. and Eylon, D. (2001) The Influence of Texture and Phase Distortion on Ultrasonic Attenuation in Ti-6Al-4V. *Journal of Nondestructive Evaluation*, **20**, 1–16.

[20] Bache, M. R. and Evans, W. J. (2001) Impact of Texture on Mechanical Properties in an Advanced Titanium Alloy. *Materials Science and Engineering*, **319–321**, 409–414.

[21] Lütjering, G. and Williams, J. (2007) *Titanium*, 2nd edn. Berlin, Springer.

[22] Tromans, D. (2011) Elastic Anisotropy of HCP Metal Crystals and Polycrystals. *International Journal of Research and Reviews in Applied Sciences*, **6**, 462–483.

[23] Li, A., Roberts, R. A., Margetan, F. J., and Thompson, R. B. (2001) Study of the Effect of Microstructure on Ultrasonic Signal Attenuation. *Review of Progress in Quantitative Nondestructive Evaluation*, **20**, 1322–1329.

[24] Uta, E., Gey, N., Bocher, P., Humbert, M., and Gilbert, J. (2009) Texture Heterogeneities in α_p/α_s Titanium Forging Analysed by EBSD—Relation to Fatigue Crack Propagation. *Journal of Microscopy*, **233**, 451–459.

[25] Panetta, P. D., Margetan, F. J., Yalda, I., and Thompson, R. B. (1996) Ultrasonic Attenuation Measurements in Jet-Engine Titanium Alloys. *Review of Progress in Quantitative Nondestructive Evaluation*, **15**, 1525–1532.

[26] Margetan, F. J., Wasan, H., and Thompson, R. B. (2000) An Experimental Study of Microstructure-Induced Ultrasonic Signal Fluctuations in Jet-Engine Titanium Alloys. *Review of Progress in Quantitative Nondestructive Evaluation*, **19**, 1433–1440.

[27] Escobar-Ruiz, E., Cawley, P., Nagy, P. B., Collison, I. J., and Wright, D. C. (2013) Ultrasonic NDE of Titanium Diffusion Bonds Using Signal Phase. *Review of Progress in Quantitative Nondestructive Evaluation*, **32**, 1409–1416.

[28] Thomas, G. H. and Spingarn, J. R. (1988) Ultrasonic Evaluation of Solid-State Welds. *Journal of Nondestructive Evaluation*, **7**, 227–235.

[29] Derby, B., Briggs, G. A. D., and Wallach, E. R. (1983) Non-Destructive Testing and Acoustic Microscopy of Diffusion Bonds. *Journal of Materials Science*, **18**, 2345–2353.

[30] Tuppen, S. J., Bache, M. R., and Voice, W. E. (2005) A Fatigue Assessment of Dissimilar Titanium Alloy Diffusion Bonds. *International Journal of Fatigue*, **27**, 651–658.

[31] Ahmed, S., Thompson, R. B., and Panetta, P. D. (2003) Ultrasonic Attenuation as Influenced by Elongated Grains. *Review of Progress in Quantitative Nondestructive Evaluation*, **22**, 109–116.

[32] Atalar, A., Quate, C. F., and Wickramasinghe, H. K. (1987) Phase Imaging in Reflection with the Acoustic Microscope. *Applied Physics Letters*, **31**, 791–793.

[33] Rose, J. L. (1999) *Ultrasonic Waves in Solid Media*. Cambridge, Cambridge University Press.

[34] British Standards Institution (2004) PD CEN/TR 14748:2004. *Non-Destructive Testing: Methodology for Qualification of Non-Destructive Tests*. London, BSI.

[35] Nagy, P. B., McGowan, P., and Adler, L. (1990) Acoustic Nonlinearities in Adhesive Joints. *Review of Progress in Quantitative Nondestructive Evaluation*, **9**, 1685–1692.

[36] Gilmore, R. S. (1996) Industrial Ultrasonic Imaging and Microscopy. *Journal of Physics D: Applied Physics*, **29**, 1389–1417.

[37] British Standards Institution (1999) BS EN 583-1:1999. *Non-Destructive Testing: Ultrasonic Examination—General Principles*. London, BSI.

[38] Rose, J. H., Roberts, R. A., and Margetan, F. J. (1992) Time-Domain Analysis of Ultrasonic Reflection from Imperfect Interfaces. *Journal of Nondestructive Evaluation*, **11**, 151–166.

[39] Krautkrämer, J., Krautkrämer, H., and Hislop, J. D. (1990) *Ultrasonic Testing of Materials*, 4th edn. Berlin, Springer-Verlag.

[40] Weglein, R. D. (1988) Titanium Diffusion Bond Evaluation via Acoustic Microscopy. *Ultrasonics Symposium*, **2**, 1045–1048.

[41] Hickling, R. (1962) An Analysis of Echoes from a Solid Elastic Sphere in Water. *Journal of the Acoustical Society of America*, **34**, 1582–1592.

[42] Faran, J. J. (1951) Sound Scattering by Solid Cylinders and Spheres. *Journal of the Acoustical Society of America*, **23**, 405–418.

[43] Ying, C. F. and Truell, R. (1956) Scattering of a Plane Longitudinal Wave by a Spherical Obstacle in an Isotropically Elastic Solid. *Journal of Applied Physics*, **27**, 1086–1097.

[44] Ahmed, S., Thompson, R. B., and Panetta, P. D. (2003) A Formal Approach to Include Multiple Scattering in the Estimation of Ultrasonic Backscattered Signals. *Review of Progress in Quantitative Nondestructive Evaluation*, **22**, 79–84.

[45] Chatillon, S., Poidevin, C., Gengembre, N., and Lhémery, A. (2003) Simplified Modeling of Backscattered Noise and Attenuation Phenomena for Quantitative Performance Demonstration of UT Methods. *Review of Progress in Quantitative Nondestructive Evaluation*, **22**, 93–100.

[46] Pinkerton, J. M. M. (1949) The Absorption of Ultrasonic Waves in Liquids and its Relation to Molecular Constitution. *Proceedings of the Physical Society Section B*, **62**, 129–147.

[47] Litovitz, T. A. and Davis, C. M. (1964) *Physical Acoustics*. New York, Academic Press.

[48] Turner, J. A. and Weaver, R. L. (1994) Radiative Transfer of Ultrasound. *Journal of the Acoustical Society of America*, **96**, 3654–3674.

[49] Drinkwater, B. W., Dwyer-Joyce, R. S., and Cawley, P. (1996) A Study of the Interaction between Ultrasound and a Partially Contacting Solid-Solid Interface. *Proceedings: Mathematical, Physical and Engineering Sciences*, **452**, 2613–2628.

[50] Lavrentyev, A. I. and Beals, J. T. (2000) Ultrasonic Measurement of the Diffusion Bond Strength. *Ultrasonics*, **38**, 513–516.

[51] Lin, L., Shi, Y. W., Chen, J., Li, X. M., and Guo, G. P. (2006) Ultrasonic Testing of the Diffusion Bonding of Titanium Alloys. *Insight*, **48**, 415–417.

[52] Camacho, J. and Fritsch, C. (2011) Phase Coherence Imaging of Grained Materials. *IEEE Transactions on Ultrasonics, Ferroelectrics and Frequency Control*, **58**, 1006–1015.

[53] Thomas, G. H. and Chinn, D. (1999) Signal Analysis Approach to Ultrasonic Evaluation of Diffusion Bond Quality. *Nondestructive Characterization of Materials IX*, **497**, 536–542.

[54] Margetan, F. J., Thompson, R. B., Rose, J. H., and Gray, T. A. (1992) The Interaction of Ultrasound with Imperfect Interfaces: Experimental Studies of Model Structures. *Journal of Nondestructive Evaluation*, **11**, 109–126.

[55] Holmes, C. and Drinkwater, B. W. (2003) The Use of Ultrasound to Measure Contact Stiffness and Pressure in Large Contacting Interfaces. *Review of Progress in Quantitative Nondestructive Evaluation*, **22**, 1072–1079.

[56] Thompson, R. B., Yu, L., and Margetan, F. J. (2005) A Formal Theory for the Spatial Correlation of Backscattered Ultrasonic Grain Noise. *Review of Progress in Quantitative Nondestructive Evaluation*, **24**, 1292–1299.

[57] Cepel, R., Ho, K. C., Rinker, B. A., Palmer, D. D., Lerch, T. P., and Neal, S. P. (2007) Spatial Correlation Coefficient Images for Ultrasonic Detection. *IEEE Transactions on Ultrasonics, Ferroelectrics and Frequency Control*, **54**, 1841–1850.

[58] Yu, L., Thompson, R. B., and Margetan, F. J. (2010) The Spatial Correlation of Backscattered Ultrasonic Grain Noise: Theory and Experimental Validation. *IEEE Transactions on Ultrasonics, Ferroelectrics and Frequency Control*, **57**, 363–378.

[59] Windels, F. and Leroy, O. (2002) Air-Coupled Ultrasonic Testing of Diffusion Bonds. *Ultrasonics*, **40**, 171–176.

[60] Baik, J. M. and Thompson, R. B. (1984) Ultrasonic Scattering from Imperfect Interfaces: A Quasi-Static Model. *Journal of Nondestructive Evaluation*, **4**, 177–196.

[61] Margetan, F. J., Thompson, R. B., and Gray, T. A. (1988) Interfacial Spring Model for Ultrasonic Interactions with Imperfect Interfaces: Theory of Oblique Incidence and Application to Diffusion-Bonded Butt Joints. *Journal of Nondestructive Evaluation*, **7**, 131–152.

[62] Palmer, D. D., Rehbein, D. K., Smith, J. F., and Buck, O. (1988) Nondestructive Characterization of the Mechanical Strength of Diffusion Bonds. I. Experimental Results. *Journal of Nondestructive Evaluation*, **7**, 153–166.

[63] Lavrentyev, A. I. and Rokhlin, S. I. (1998) Ultrasonic Spectroscopy of Imperfect Contact Interfaces between a Layer and Two Solids. *Journal of the Acoustical Society of America*, **103**, 657–664.

[64] Brotherhood, C. J., Drinkwater, B. W., and Guild, F. J. (2003) The Effect of Compressive Loading on the Ultrasonic Detectability of Kissing Bonds in Adhesive Joints. *Journal of Nondestructive Evaluation*, **21**, 95–104.

[65] Buck, O., Thompson, R. B., Rehbein, D. K., Palmer, D. D., and Brasche, L. J. H. (1989) Contacting Surfaces: A Problem in Fatigue and Diffusion Bonding. *Metallurgical Transactions A*, **20**, 627–636.

[66] Nagy, P. B. and Adler, L. (1988) Ultrasonic NDE of Solid-State Bonds: Inertia and Friction Welds. *Journal of Nondestructive Evaluation*, **7**, 199–215.

[67] Pilant, W. L., Knopoff, L., and Schwab, F. (1964) Transmission and Reflection of Surface Waves at a Corner. 3. Rayleigh Waves (Experimental). *Journal of Geophysical Research*, **69**, 291–297.

[68] Instanes, G., Pedersen, A., Toppe, M., and Nagy, P. B. (2009) Constant Group Velocity Ultrasonic Guided Wave Inspection for Corrosion and Erosion Monitoring in Pipes. *Review of Progress in Quantitative Nondestructive Evaluation*, **28**, 1386–1393.

[69] Zheng, Y., Maev, R. G., and Solodov, I. Y. (1999) Nonlinear Acoustic Applications for Material Characterization: A Review. *Canadian Journal of Physics*, **77**, 927–967.

[70] Hughes, D. S. and Kelly, J. L. (1953) Second-Order Elastic Deformation of Solids. *Physical Review*, **92**, 1145–1149.

[71] Landau, L. D. and Lifshitz, E. M. (1975) *Theory of Elasticity*, 3rd edn. Pergamon Press.

[72] Murnaghan, F. D. (1937) Finite Deformations of an Elastic Solid. *American Journal of Mathematics*, **59**, 235–260.

[73] Hikata, A., Chick, B. B., and Elbaum, C. (1963) Effect of Dislocations on Finite Amplitude Ultrasonic Waves in Aluminium. *Applied Physics Letters*, **3**, 195–197.

[74] Toupin, R. A. and Bernstein, B. (1961) Sound Waves in Deformed Perfectly Elastic Materials – Acoustoelastic Effect. *Journal of the Acoustical Society of America*, **33**, 216.

[75] Johnson, G. C. (1981) Acoustoelastic Theory for Elastic–Plastic Materials. *Journal of the Acoustical Society of America*, **70**, 591–595.

[76] Nagy, P. B. (1998) Fatigue Damage Assessment by Non-Linear Ultrasonic Materials Characterization. *Ultrasonics*, **36**, 375–381.

[77] Collison, I. J., Stratoudaki, T., Clark, M., and Somekh, M. G. (2008) Measurement of Elastic Nonlinearity Using Remote Laser Ultrasonics and CHeap Optical Transducers and Dual Frequency Surface Acoustic Waves. *Ultrasonics*, **28**, 471–477.

[78] Buck, O., Morris, W. L., and Richardson, J. M. (1978) Acoustic Harmonic Generation at Unbonded Interfaces and Fatigue Cracks. *Applied Physics Letters*, **33**, 371–372.

[79] Breazeale, M. A. and Philip, J. (1984) Determination of Third-Order Elastic Constants from Ultrasonic Generation Measurements. *Physical Acoustics: Principles and Methods*, **17**, 1–60.

[80] Yost, W. T., Cantrell, J. H., and Na, J. K. (2000) Nonlinear Ultrasonic Pulsed Measurements and Applications to Metal Processing and Fatigue. *Review of Progress in Quantitative Nondestructive Evaluation*, **20**, 1268–1275.

[81] Richardson, J. M. (1979) Harmonic Generation at an Unbonded Interface—I. Planar Interface Between Semi-Infinite Elastic Media. *International Journal of Engineering Science*, **17**, 73–85.

[82] Barnard, D. J., Dace, G. E., Rehbein, D. K., and Buck, O. (1997) Acoustic Harmonic Generation at Diffusion Bonds. *Journal of Nondestructive Evaluation*, **16**, 77–89.

[83] Breazeale, M. A. and Thompson, D. O. (1963) Finite-Amplitude Ultrasonic Waves in Aluminum. *Applied Physics Letters*, **3**, 77–78.

[84] Barnard, D. J., Dace, G. E., and Buck, O. (1997) Acoustic Harmonic Generation Due to Thermal Embrittlement of Inconel 718. *Journal of Nondestructive Evaluation*, **16**, 67–75.

[85] Buck, O., Morris, W. L., and James, M. R. (1980) Remaining Fatigue Life Prediction in the Initiation Regime Using SAW NDE. *Journal of Nondestructive Evaluation*, **1**, 3–9.

[86] Achenbach, J. D. and Norris, A. N. (1982) Loss of Specular Reflection Due to Nonlinear Crack-Face Interaction. *Journal of Nondestructive Evaluation*, **3**, 229–239.

[87] Barnard, D. J., Brasche, L. J. H., Raulerson, D., and Degtyar, A. D. (2003) Monitoring Fatigue Damage Accumulation With Rayleigh Wave Harmonic Generation Measurements. *Review of Progress in Quantitative Nondestructive Evaluation*, **22**, 1393–1400.

[88] Yost, W. T. and Cantrell, J. H. (1990) Materials Characterization Using Acoustic Nonlinearity Parameters and Harmonic Generation: Engineering Materials. *Review of Progress in Quantitative Nondestructive Evaluation*, **9**, 1669–1676.

[89] Rollins, F. R., Taylor, L. H., and Todd, P. H. (1964) Ultrasonic Study of Three-Phonon Interactions. II. Experimental Results. *Physical Review*, **136**, 597–601.

[90] Taylor, L. H. and Rollins, F. R. (1964) Ultrasonic Study of Three-Phonon Interactions. I. Theory. *Physical Review*, **136**, 591–596.

[91] Croxford, A. J., Wilcox, P. D., Drinkwater, B. W., and Nagy, P. B. (2009) The Use of Non-Collinear Mixing for Nonlinear Ultrasonic Detection of Plasticity and Fatigue. *Journal of the Acoustical Society of America*, **126**, 117–122.

[92] Childress, J. D. and Hambrick, C. G. (1964) Interactions Between Elastic Waves in an Isotropic Solid. *Physical Review*, **136**, 411–418.

[93] Yamada, R., Kawashima, K., and Murase, M. (2006) Application of Nonlinear Ultrasonic Measurement for Quality Assurance of Diffusion Bonds of Gamma Titanium Aluminium Alloy and Steel. *Research in Nondestructive Evaluation*, **17**, 223–239.

[94] Hirsekorn, S., Koka, A., Wegner, A., and Arnold, W. (2000) Quality Assessment of Bond Interfaces by Nonlinear Ultrasonic Transmission. *Review of Progress in Quantitative Nondestructive Evaluation*, **19**, 1367–1374.

[95] Ulrich, T. J., Sutin, A. M., Claytor, T., Papin, P., Bas, P., and TenCate, J. A. (2008) The Time Reversed Elastic Nonlinearity Diagnostic Applied to Evaluation of Diffusion Bonds. *Applied Physics Letters*, **93**, 1–3.

[96] Jones, G. L. and Kobett, D. R. (1963) Interaction of Elastic Waves in an Isotropic Solid. *The Journal of the Acoustical Society of America*, **35**, 5–10.

[97] Solodov, I. Y., Asainov, A., and Len, K. (1993) Non-Linear SAW Reflection: Experimental Evidence and NDE Applications. *Ultrasonics*, **31**, 91–96.

[98] Solodov, I. Y., Krohn, N., and Busse, G. (2002) CAN: An Example of Nonclassical Acoustic Nonlinearity in Solids. *Ultrasonics*, **40**, 621–625.

[99] Donskoy, D., Sutin, A. M., and Ekimov, A. (2001) Nonlinear Acoustic Interaction on Contact Interfaces and Its Use for Nondestructive Testing. *NDT&E International*, **34**, 231–238.

[100] Nagy, P. B. (2014) Discussion on the Filtering Effects of Imperfect Interfaces, [Personal Communication] Imperial College London.

[101] Desilets, C. S., Fraser, J. D., and Kino, G. S. (1978) The Design of Efficient Broadband Piezoelectric Transducers. *IEEE Transactions on Sonics and Ultrasonics*, **25**, 115–125.

[102] Kossoff, G. (1966) The Effects of Backing and Matching on the Performance of Piezoelectric Ceramic Transducers. *IEEE Transactions on Sonics and Ultrasonics*, **13**, 20–30.

[103] Gachagan, A., Harvey, G., O'Leary, R. L., and Mackersie, J. (2007) Investigating the Influence of the Constituent Materials on the Performance of Periodic Piezoelectric Composite Arrays. *Review of Progress in Quantitative Nondestructive Evaluation*, **26**, 759–766.

[104] Oppenheim, A. and Schafer, R. (1975) *Digital Signal Processing*, 1st edn. Prentice Hall.

[105] Harris, F. J. (1978) On the Use of Windows for Harmonic Analysis with the Discrete Fourier Transform. *Proceedings of the IEEE*, **66**, 51–83.

[106] Shiavi, R. (2007) Spectral Analysis of Random Signals. In: *Introduction to Applied Statistical Signal Analysis*, 3rd edn. Burlington, Academic Press.

[107] Paliwal, K., Wójcicki, K., and Shannon, B. (2011) The Importance of Phase in Speech Enhancement. *Speech Communications*, **53**, 465–494.

[108] Reddy, N. S. and Swamy, M. N. S. (1985) Derivative of the Phase Spectrum of Truncated Autoregressive Signals. *IEEE Transactions on Circuits and Systems*, **32**, 616–618.

[109] Instanes, G., Toppe, M., Lakshminarayan, B., and Nagy, P. B. (2007) *Corrosion and Erosion Monitoring of Pipes by an Ultrasonic Guided Wave Method*, In: Advanced Ultrasonic Methods for Materials and Structure Inspection, p. 115–157. London, ISTE Ltd.

[110] Wenbo, H., Kaifeng, Z., and Guofeng, W. (2007) Superplastic Forming and Diffusion Bonding for Honeycomb Structure of Ti-6Al-4V Alloy. *Journal of Materials Processing Technology*, **183**, 450–454.

[111] Vázquez, M., Ramos, A., Leija, L., and Vera, A. (2006) Noninvasive Temperature Estimation in Oncology Hyperthermia Using Phase Changes in Pulse-Echo Ultrasonic Signals. *Japanese Journal of Applied Physics*, **45**, 7991–7998.

[112] British Standards Institution (1999) BS EN ISO 14644-1:1999. *Cleanrooms and Associated Controlled Environments—Classification of Air Cleanliness*. London, BSI.

[113] Friend, G. W. (2014) *The Effect of Defects on the Mechanical Properties of Fibre-Reinforced Titanium Metal-Matrix Composites under Fatigue Loading*. Doctoral Thesis, University of Birmingham.

[114] Nikgolov, M. B. and Karakozov, E. S. (1990) Diffusion Bonding Dissimilar Titanium Alloys. *Welding International*, **4**, 883–886.

[115] Ridley, N., Wang, Z. C., and Lorimer, G. W. (1997) Diffusion Bonding of Dissimilar Superplastic Titanium Alloys. *Materials Science Forum*, **243–245**, 669–674.

[116] Welsch, G., Boyer, R., and Collins, E. W. (1994) *Materials Properties Handbook: Titanium Alloys*. ASM International.

[117] Balasubramanian, V., Fernandus, M. J., and Senthilkumar, T. (2013) Development of Processing Windows for Diffusion Bonding of Aluminium/Magnesium Dissimilar Materials. *Welding in the World*, **57**, 523–539.

[118] Hu, W., Ponge, D., and Gottstein, G. (1995) Origin of Grain Boundary Motion during Diffusion Bonding by Hot Pressing. *Materials Science and Engineering: A*, **190**, 223–229.

[119] Huang, Y., Ridley, N., Humphreys, F. J., and Cui, J. (1999) Diffusion Bonding of Superplastic 7075 Aluminium Alloy. *Materials Science and Engineering: A*, **266**, 295–302.

[120] Huang, Y., Cui, J., and Ma, L. (1990) Kinetics of Grain Growth across Bond Interface during Diffusion Bonding. *MRS Proceedings*, **196**, 137–142.

[121] Gudmundson, P. (1983) The Dynamic Behaviour of Slender Structures with Cross-Sectional Cracks. *Journal of the Mechanics and Physics of Solids*, **31**, 329–345.

[122] Solodov, I. Y. (1998) Ultrasonics of Non-Linear Contacts: Propagation, Reflection and NDE Applications. *Ultrasonics*, **36**, 383–390.

[123] Demčenko, A., Akkerman, R., Nagy, P. B., and Loendersloot, R. (2012) Non-Collinear Wave Mixing for Non-Linear Ultrasonic Detection of Physical Ageing in PVC. *NDT&E International*, **49**, 34–39.

[124] Ohara, Y., Kawashima, K., Yamada, R., and Horio, H. (2004) Evaluation of Amorphous Diffusion Bonding by Nonlinear Ultrasonic Method. *Review of Progress in Quantitative Nondestructive Evaluation*, **23**, 944–951.

[125] Turnbull, D. H. and Foster, F. S. (1991) Beam Steering with Pulsed Two-Dimensional Transducer Arrays. *IEEE Transactions on Ultrasonics, Ferroelectrics and Frequency Control*, **38**, 320–333.

[126] Mankins, J. C. (1995) *Technology Readiness Levels*. [White Paper] Office of Space Access and Technology, NASA.

Appendices

Appendix A: Filtering Effects of an Imperfect Interface

The analysis presented below is the result of discussions with Prof. Peter B. Nagy [100].

An imperfect interface behaves like a first-order High-Pass Filter (HPF) when reflecting incoming acoustic waves. Such an HPF has a transfer function, $K(\omega)$, of the form:

$$K(\omega) = \frac{\frac{i\omega}{\Omega}}{1+\frac{i\omega}{\Omega}},$$

where ω denotes the angular frequency and Ω is the -3 dB cut-off frequency of the filter. The group delay, τ_g, of such a filter can be related to its phase spectrum, $\varphi(\omega) = \frac{\pi}{2} - \tan^{-1}\frac{\omega}{\Omega}$, as follows (using $e^{+i\omega t}$ rather than $e^{-i\omega t}$ in the definition of phase):

$$\tau_g = -\frac{\partial\varphi}{\partial\omega}.$$

The group delay is then:

$$\tau_g = \frac{\Omega}{\omega^2+\Omega^2}.$$

In situations where only relatively weak reflections are obtained from the imperfect interface because $\omega \ll \Omega$, as is the case here, the group delay can be approximated as:

$$\tau_g \approx \frac{1}{\Omega}.$$

Although the group delay of the detected signal is indeed larger than the physical propagation time by an amount equal to the group delay of the filter formed by the reflector, the equivalent extra propagation distance is much less than one wavelength since $\omega \ll \Omega$. The true phase will clearly be affected, but not by a significant amount.

Appendix B: Experiment Jig

Draught (overleaf) of the jig manufactured to ensure that the same specimen volume was insonified during each of the two inspections required for the single-sided [linear] ultrasonic technique. This technique, described and assessed in Chapters 3 and 4, was used to estimate the interfacial stiffness of diffusion-bonded Ti-6Al-4V samples.

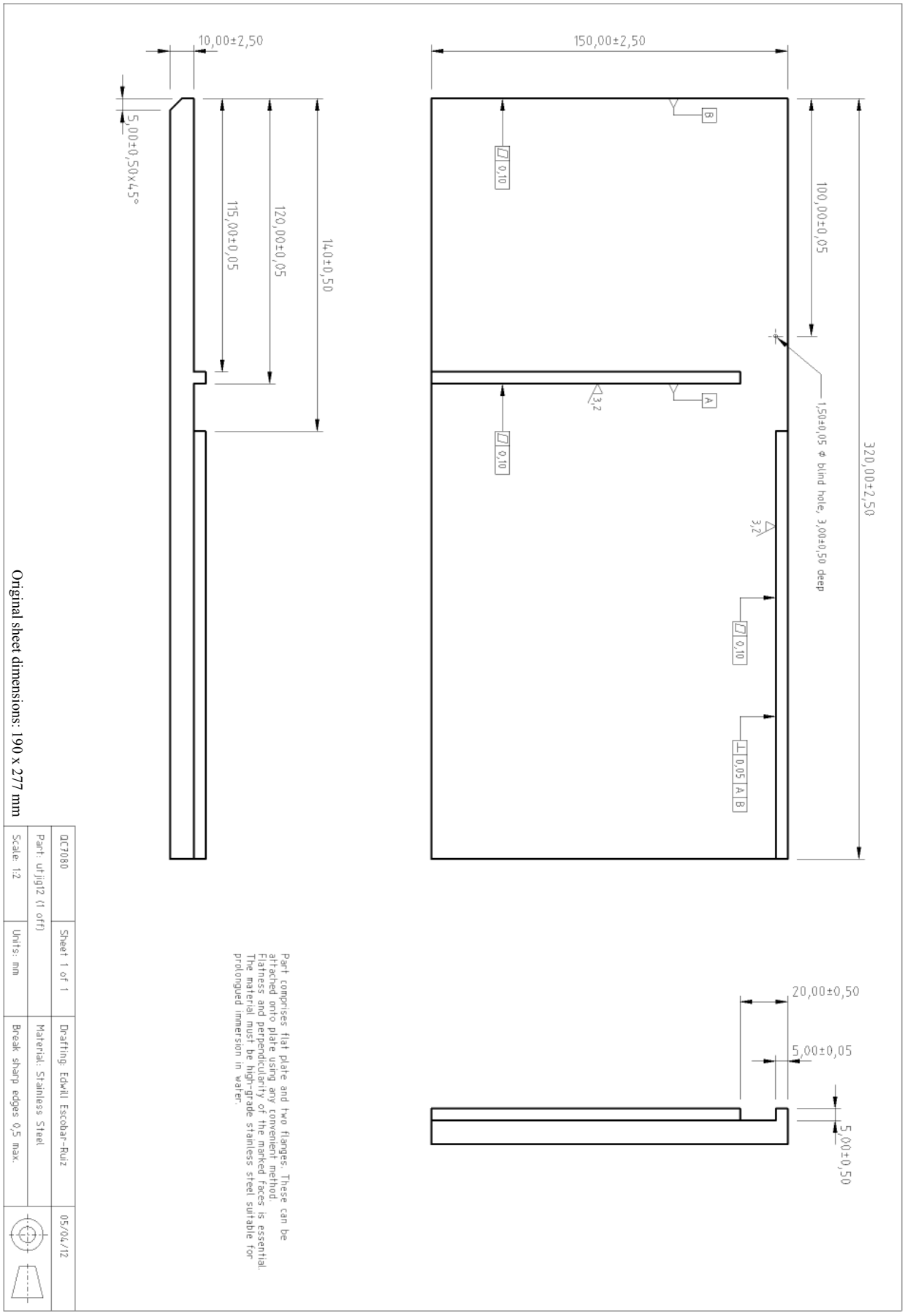
10,00±2,50
5,00±0,50x45°
115,00±0,05
120,00±0,05
140±0,50
150,00±2,50
100,00±0,05
320,00±2,50
1,50±0,05 ⌀ blind hole, 3,00±0,50 deep
0,10
3,2
A
B
0,05 A B
20,00±0,50
5,00±0,05
5,00±0,50
Part comprises flat plate and two flanges. These can be attached onto plate using any convenient method. Flatness and perpendicularity of the marked faces is essential. The material must be high-grade stainless steel suitable for prolonged immersion in water.
Original sheet dimensions: 190 x 277 mm
QC7080
Sheet 1 of 1
Drafting: Edwill Escobar-Ruiz
05/04/12
Part: ut jig12 (1 off)
Material: Stainless Steel
Scale: 1:2
Units: mm
Break sharp edges 0,5 max.

Appendix C: Computational Code

Computational (Matlab®) code used to perform the main processing steps required for the single-sided [linear] ultrasonic technique as presented in Figure 4.6. The algorithm is described by a pseudo-code and comments designated by the '%' symbol.

Begin function: trPh

```
function [trPhMap extractStart slope] =trPh(data,centreFreq_MHz,samplingFreq_MHz,...
        signalStart_pt,threshold)
% Speed-optimised phase analysis of single data set using half-energy centering and true
%       phase iteration
%
% SYNTAX
%
% [trPhMap extractStart slope] =trPh(data,centreFreq_MHz,samplingFreq_MHz,signalStart_pt,
%       threshold)
%
% INPUTS
%
% data: name of the three-dimensional array of ultrasonic data to be processed
% centreFreq_MHz: signal centre frequency [MHz]
% samplingFreq_MHz: signal sampling frequency [MHz]
% signalStart_pt: minimium position in time at which the plateau section can start (related
%       to earliest possible signal arrival time) [pt]
% threshold: amplitude threshold below which phase measurements are not made [bit-space
%       value]
%
% OUPUTS
%
% trPhMap: complete true-phase map [rad]
% extractStart: extraction start time for each of the x-y points in the provided data set
%       [pt]
% slope: slope of the extrapolation line used to obtain the true phase at each x-y point
%       [pts]
%
% NOTE
%
% This algorithm does not check the validity of any of the inputs.
xLength =size(data,1);
yLength =size(data,2);
trPhMap =zeros(xLength,yLength);
slope =zeros(xLength,yLength);
extractStart =zeros(xLength,yLength);
windowLength =round(samplingFreq_MHz /centreFreq_MHz); % Total length of rectangular
%       extraction window [pts]
cScan =squeeze(max(abs(data(:,:,signalStart_pt :(signalStart_pt +windowLength -1))),[],3));
% switch centreFreq_MHz
%     case 9.37
%         probeFactor =0;
%     case 4.73
%         probeFactor =0;
%     case 9.25
%         probeFactor =0;
%     case 18.25
%         probeFactor =-0.0171;
% end
%% Phase measurement: first pass
waitbarID =waitbar(0,'Extracting and analysing signals...');
```

```
for yPosition =1 :1 :yLength
    waitbarFraction =yPosition/yLength;
    waitbar(waitbarFraction,waitbarID);
    for xPosition =1 :1 :xLength
        if cScan(xPosition,yPosition) >=threshold
            extracted =squeeze(data(xPosition,yPosition,signalStart_pt :(signalStart_pt...
                +windowLength -1)));
            [~, ~, ~, straightLine ~,] =trPhAlg(extracted,centreFreq_MHz,samplingFreq_MHz);

            %% Phase measurement: second pass

            modifier =-round(((straightLine(1) *samplingFreq_MHz -pi) /pi) /2);
            if abs(straightLine(1)) >0.5; modifier =0; end % Prevent addressing dimensions
            %   larger than data array size due to noisy signals
            extractStart(xPosition,yPosition) =signalStart_pt +modifier; % Second pass at
            %   extracting the signal from correct point

            extracted =squeeze(data(xPosition,yPosition,extractStart(xPosition,yPosition)...
                :(extractStart(xPosition,yPosition) +windowLength -1)));
            [~, ~, ~, straightLine ~,] =trPhAlg(extracted,centreFreq_MHz,samplingFreq_MHz);

            trPhMap(xPosition,yPosition) =straightLine(2);
            slope(xPosition,yPosition) =((straightLine(1) *samplingFreq_MHz -pi) /pi) /2;
                % Verification of adequate slope minimisation
        end
    end
end
close(waitbarID);
end
```

End function: trPh

The above function calls and depends on the following subroutine (also described by a pseudo-code and comments designated by the '%' symbol):

Begin function: trPhAlg

```
function [freqSpect phaseSpect freqAxis straightLine centreFreqIndex] =trPhAlg(signal,...
        centreFreq_MHz,samplingFreq_MHz)
% Speed-optimised calculation of frequency and phase spectra for a given signal
%
% SYNTAX
%
% [freqSpect phaseSpect freqAxis straightLine centreFreqIndex] =trPhAlg(signal,...
%       centreFreq_MHz,samplingFreq_MHz)
%
% INPUTS
%
% signal: un-spliced, un-windowed input signal of any bit depth and any numerical format
%       [a. u.]
% centreFreq_MHz: signal centre frequency [MHz]
% samplingFreq_MHz: signal sampling frequency [MHz]
%
% OUPUTS
%
% freqSpect: complete complex frequency spectrum of input signal [a. u.]
% phaseSpect: complete phase spectrum of input signal [rad]
% freqAxis: complete frequency axis used for both 'freqSpect' and 'phaseSpect' [MHz]
% straightLine: coefficients for least-squares linear fit over the phase region of interest
% centreFreqIndex: index for centre frequency position (both 'freqSpect' and 'phaseSpect'
%       spectra)
%
% NOTE
%
% This algorithm does not check whether the signal is a column vector or whether the Nyquist
% criterion is met. The DC and Nyquist Frequency components of the computed amplitude
% spectra are not correctly scaled. The 'double()' function is applied to the input signal
```

```
% here. The winspect correction factor (wcf) applied in this function corrects the DC offset
% inherent to winspect files.

roiHalfLength =5; % Half of the number of points over which to apply linear regression in
%       order to find the true phase [pts]
minResolution =10000; % [pts]

%% Padded Signal
% New array must encapsulate minResolution as well as the signal, and must be a power of two

originalPts =size(signal,1);
zeroLength =2 ^nextpow2(originalPts +minResolution) -originalPts;
signal =double([signal(round(originalPts /2) +1 :end); zeros(zeroLength,1); signal(1 :...
        round(originalPts /2))]);

%% Frequency and phase spectra

numOfPts =size(signal,1);

freqSpect =fft(signal,numOfPts); % Frequency spectrum of input signal [% FSH]
phaseSpect =unwrap(angle(freqSpect)); % Phase spectrum of input signal [Rad]

freqStep =samplingFreq_MHz /numOfPts; % [MHz]
freqAxis =(0 :freqStep :freqStep *(numOfPts -1)).'; % [MHz]

%% Phase spectra linear fit
% Matlab indexing starts at 1 whereas freqAxis starts at zero.

centreFreqIndex =round(centreFreq_MHz /samplingFreq_MHz *numOfPts +1);
hiFreqIndex =centreFreqIndex +roiHalfLength; % End of region of interest
lowFreqIndex =centreFreqIndex -roiHalfLength; % Start of region of interest
straightLine =polyfit(freqAxis(lowFreqIndex:hiFreqIndex),phaseSpect(lowFreqIndex:...
        hiFreqIndex),1);

end
```

End function: trPhAlg

Appendix D: True-Phase Maps

Interface true phase, Φ_{bond}, maps for the specimens whose interfacial stiffness maps are given in Figure 4.8. A similar global determination of interface integrity is possible from true-phase measurements alone as with interfacial stiffness estimates. However, reflection magnitude is not a factor in true-phase measurements, which means that valuable amplitude information is under-utilised if Equation (3.5) is not employed.

The values in brackets in the figure below are the standard deviation of true-phase measurement for each map shown. These large variations within each sample are partially the result of variations in interface quality, as is expected from samples that have had their interfaces only partially contaminated. The variations, along with inevitable measurement error, are amplified in the results shown in Figure 4.8.

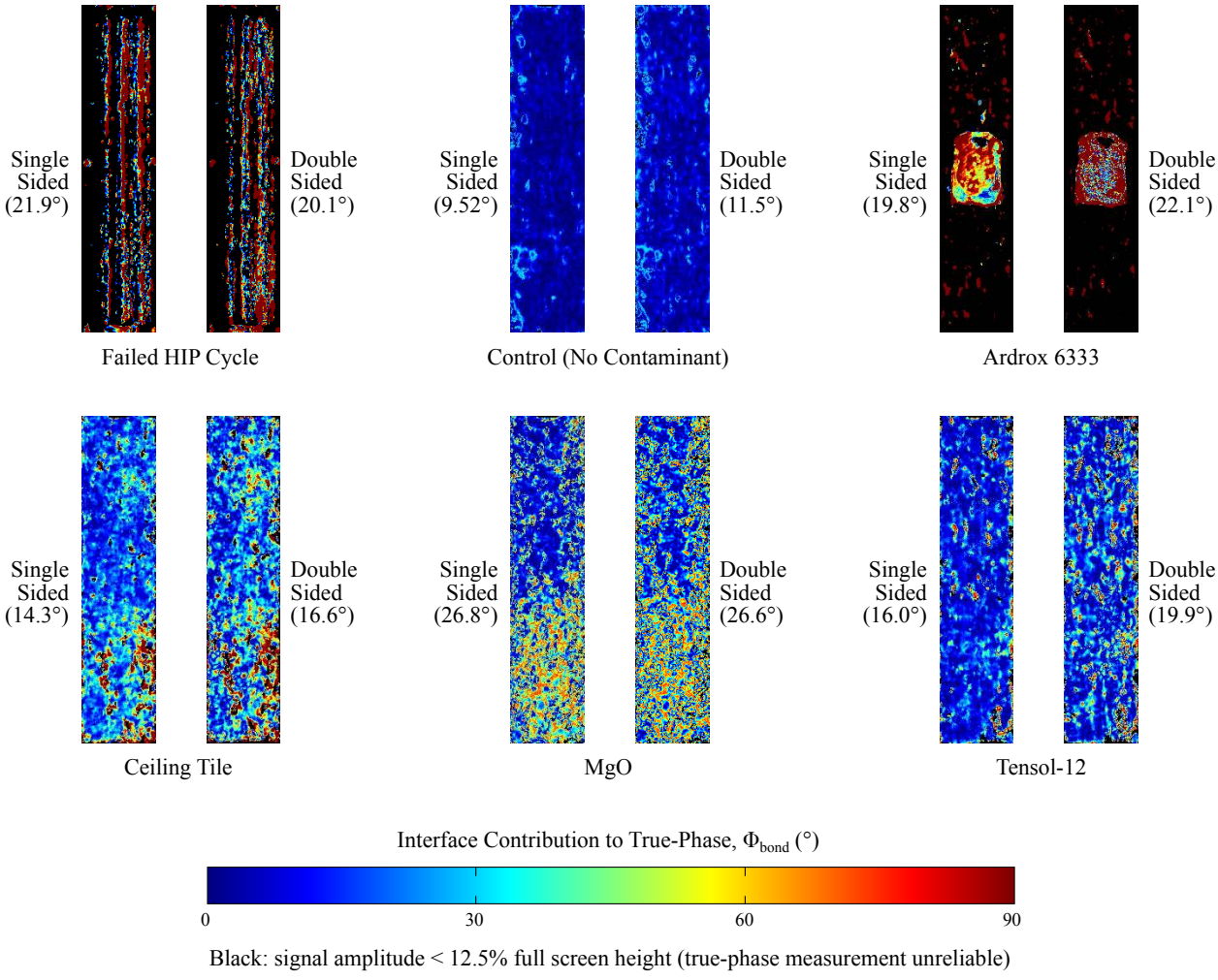

Appendix E: Non-Linear Specimen Micrographs

Micrographs of the specimens used in the non-linear experiments laid out in Chapter 5.

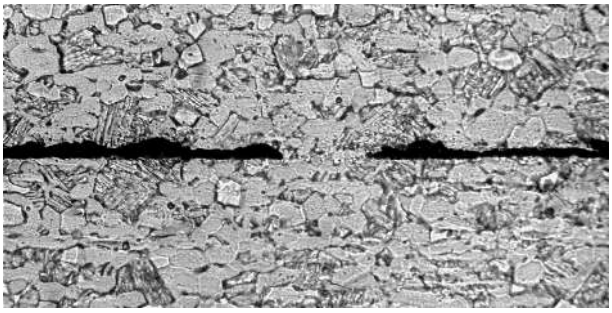

Sample 1: 6.59% CBGG

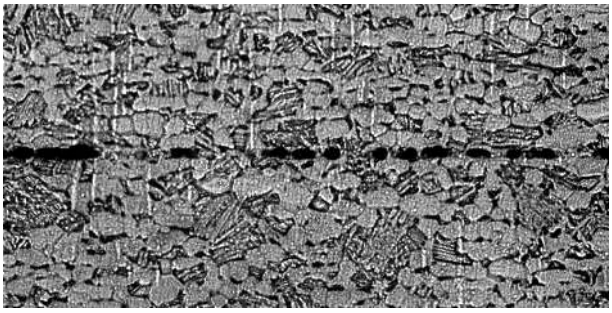

Sample 2: 32.7% CBGG

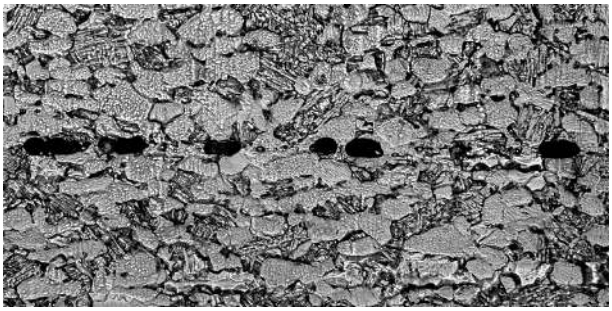

Sample 3: 48.0% CBGG

Sample 4: 68.8% CBGG

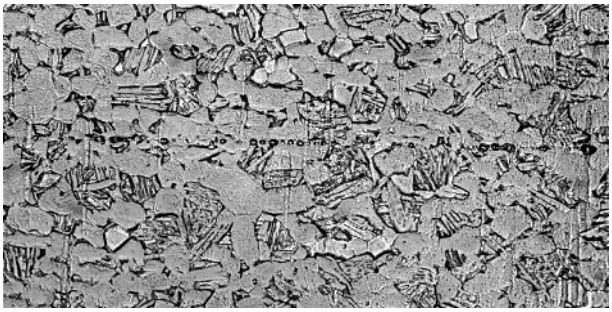

Sample 5: 73.2% CBGG

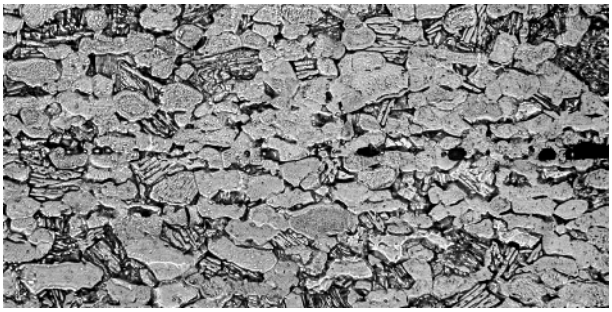

Sample 6: 79.3% CBGG

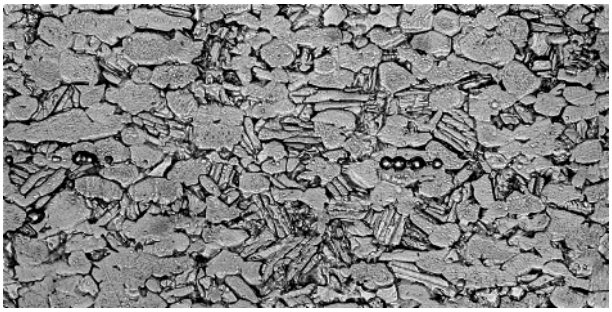

Sample 7: 85.1% CBGG

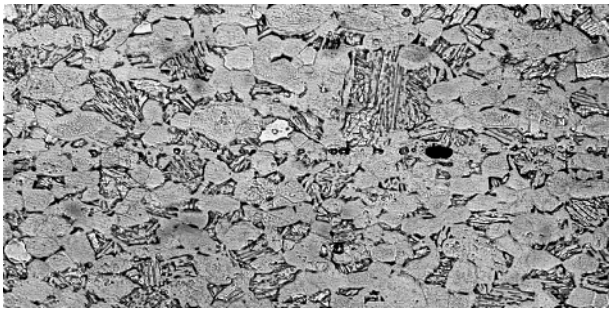

Sample 8: 86.0% CBGG

25 µm